

INFORMATION TO USERS

This manuscript has been reproduced from the microfilm master. UMI films the text directly from the original or copy submitted. Thus, some thesis and dissertation copies are in typewriter face, while others may be from any type of computer printer.

The quality of this reproduction is dependent upon the quality of the copy submitted. Broken or indistinct print, colored or poor quality illustrations and photographs, print bleedthrough, substandard margins, and improper alignment can adversely affect reproduction.

In the unlikely event that the author did not send UMI a complete manuscript and there are missing pages, these will be noted. Also, if unauthorized copyright material had to be removed, a note will indicate the deletion.

Oversize materials (e.g., maps, drawings, charts) are reproduced by sectioning the original, beginning at the upper left-hand corner and continuing from left to right in equal sections with small overlaps. Each original is also photographed in one exposure and is included in reduced form at the back of the book.

Photographs included in the original manuscript have been reproduced xerographically in this copy. Higher quality 6" x 9" black and white photographic prints are available for any photographs or illustrations appearing in this copy for an additional charge. Contact UMI directly to order.

U·M·I

University Microfilms International
A Bell & Howell Information Company
300 North Zeeb Road, Ann Arbor, MI 48106-1346 USA
313/761-4700 800/521-0600

Order Number 1358520

The effect of particle size on the reduction of ilmenite

Marathay, Prashant Arvind, M.S.

The University of Arizona, 1994

Copyright ©1994 by Marathay, Prashant Arvind. All rights reserved.

U·M·I
300 N. Zeeb Rd.
Ann Arbor, MI 48106

THE EFFECT OF PARTICLE SIZE ON THE REDUCTION OF ILMENITE

by

Prashant Arvind Marathay

Copyright © Prashant Arvind Marathay 1994

A Thesis Submitted to the Faculty of the
DEPARTMENT OF CHEMICAL ENGINEERING
In Partial Fulfillment of the Requirements
For the Degree of
MASTER OF SCIENCE
In the Graduate College
THE UNIVERSITY OF ARIZONA

1994

THE EFFECT OF PARTICLE SIZE ON THE REDUCTION OF ILMENITE

by

Prashant Arvind Marathay

Copyright © Prashant Arvind Marathay 1994

A Thesis Submitted to the Faculty of the
DEPARTMENT OF CHEMICAL ENGINEERING
In Partial Fulfillment of the Requirements
For the Degree of
MASTER OF SCIENCE
In the Graduate College
THE UNIVERSITY OF ARIZONA

1994

STATEMENT BY AUTHOR

This thesis has been submitted in partial fulfillment of the requirements for an advanced degree at The University of Arizona and is deposited in the University Library to be made available to borrowers under rules of the Library.

Brief quotations from this thesis are allowable without special permission, provided that accurate acknowledgment of source is made. Requests for permission for extended quotation from or reproduction of this manuscript in whole or in part may be granted by the copyright holder.

SIGNED : Robert A. Mitty

APPROVAL BY THESIS DIRECTOR

This thesis has been approved on the date shown below:

Farhang Shadman
Farhang Shadman

6-6-94
Date

Professor of Chemical Engineering

ACKNOWLEDGMENTS

It is with immeasurable gratitude that I thank Dr. Farhang Shadman. His kindness, wisdom and guidance have been a tremendous resource during my studies at the University of Arizona. He is one of the finest managers I have had the pleasure to work for and I have enjoyed his company.

Mr. Xiaoyang Du also deserves special mention. He has served as a technical advisor, mentor and supportive friend. His knowledge and patience allowed for my success.

Special thanks go to Dr. Andrew Cutler for his time and knowledge regarding the Lunar Sample and additional thanks go to Gary Chandler and Kris Law for their expertise using the Scanning Electron Microscope.

Financial support was provided by NASA and the Department of Chemical Engineering, to whom I am grateful. Jo Robb, Wendy Haley and Richard Fife were especially helpful with administrative work and Sal Gonzales, Charles Amling and Lorenzo Lujan were invaluable in helping design and repair laboratory equipment.

Finally, I would like to thank my friends and colleagues in the Department of Chemical Engineering, especially Fabio Baldessari, for helping me remember whenever I had forgotten. I hope to repay all of their kindness with friendship.

DEDICATION

This work is dedicated to my parents, Arvind and Sunita Marathay, my wife, Leena, and my sister, Gitika. Their love, encouragement and confidence in my abilities have always been appreciated. Without their support, none of this would have been possible.

TABLE OF CONTENTS

LIST OF ILLUSTRATIONS	7
LIST OF TABLES	10
INTRODUCTION	13
Introductory Remarks	13
Purpose	17
Method of Approach	19
EXPERIMENTAL PROCEDURE AND APPARATUS	22
Experimental Setup	22
Specific Equipment	24
<i>CAHN Electronic Balance</i>	24
<i>Varian Gas Chromatograph</i>	25
<i>Infrared CO/CO₂ Analyzer</i>	26
<i>Horiba CO₂ Analyzer</i>	26
<i>Lindberg Furnace</i>	27
Sample and Sample Preparation	27
<i>Experimental Sample Preparation</i>	27
<i>Sample Preparation for Analysis</i>	28
Experimental Procedure	31
Experimental Procedure for Hydrogen Reduction	33
Experimental Procedure for Carbon Monoxide Reduction	36
Observations	36
REDUCTION OF ILMENITE WITH HYDROGEN	50
Experimental Apparatus	50
Modeling	50
Results	52
Discussion	56
REDUCTION OF ILMENITE WITH CARBON MONOXIDE	63
Experimental Apparatus	63
Modeling	63
Results	68
Discussion	72
REDUCTION OF LUNAR SOIL WITH HYDROGEN	87
Lunar Soil	87
Specific Lunar Sample	88

TABLE OF CONTENTS - *Continued*

Experimental Apparatus	94
Results	95
Discussion	95
CONCLUSIONS AND RECOMMENDATIONS	109
Conclusions	109
Recommendations	110
NOTATION	111
APPENDIX A: REDUCTION DATA	113
Hydrogen Reduction Data	113
Carbon Monoxide Reduction Data	116
Lunar Soil Reduction Data	122
APPENDIX B: PARTICLE SIZE DATA	123
REFERENCES	129

LIST OF ILLUSTRATIONS

2.1	Experimental Setup	23
2.2	SEM Micrograph of Ilmenite Particles greater than 100 μm	29
2.3	SEM Micrograph of Sieved and Washed Ilmenite Particles	30
2.4	SEM Micrograph of Sieved and Superwashed Ilmenite Particles	30
2.5	Hydrogen Reaction Matrix for Ilmenite Reduction	34
2.6	Carbon Monoxide Reaction Matrix for Ilmenite Reduction	34
2.7	Reaction Rates using a Quartz Pan vs. a Die Pellet	39
2.8	Reaction Rates using a Die Pellet	40
2.9	Effect of Die Pelletizing on Ilmenite Particles	41
2.10	Effect of Die Pelletizing on Ilmenite Particles	42
2.11	Overall Cross Section of a Partially Reduced Ilmenite Pellet	43
2.12	Edge Particle of a Partially Reduced Ilmenite Pellet	44
2.13	Center Particle of a Partially Reduced Ilmenite Pellet	45
2.14	Reaction Rates using a Mesh Basket vs. a Calcined Pellet	46
2.15	Effect of Flow Rate and Sample Mass using a Mesh Basket	48
2.16	Effect of Fines on Reaction Rates	49
3.1	Effect of Particle Size on Ilmenite Reduction using Hydrogen	53
3.2	Effect of Temperature on 325-400 mesh Ilmenite Particles	54
3.3	Arrhenius Plot for 325-400 mesh Ilmenite Particles using Hydrogen	55
3.4	Partially Reduced Ilmenite	57

LIST OF ILLUSTRATIONS - *Continued*

3.5	Reaction Rate Predicted by Model vs. Experimental Data for 325-400 mesh Ilmenite Particles	58
3.6	Model Prediction for Larger Ilmenite Particles	59
3.7	Reaction Rate Predicted by Model vs. Experimental Data for 140-170 mesh Ilmenite Particles	61
3.8	Reaction Rate Predicted by Model vs. Experimental Data for 60-70 mesh Ilmenite Particles	62
4.1	Effect of Particle Size on Ilmenite Reduction using Carbon Monoxide	69
4.2	Effect of Temperature on 325-400 mesh Ilmenite Particles	70
4.3	Arrhenius Plot for 325-400 mesh Ilmenite Particles using Carbon Monoxide	71
4.4	Reaction Rate Predicted by Model vs. Experimental Data for 325-400 mesh Ilmenite Particles	73
4.5	Reaction Rate Predicted by Nucleation Model vs. Experimental Data for 325-400 mesh Ilmenite Particles	75
4.6	Iron Dispersed at Low Conversion	77
4.7	Iron Dispersed at High Conversion	77
4.8	Reaction Data Predicted using a Variable Diffusivity	79
4.9	Reaction Data Predicted using a Variable Diffusivity	80
4.10	Diffusivity vs. Conversion	81
4.11	Diffusivity vs. Conversion - Effect of Temperature	82
4.12	Diffusivity vs. Conversion - Effect of Particle Size	83
4.13	Diffusivity vs. Conversion	85

LIST OF ILLUSTRATIONS - *Continued*

4.14	Reaction Rate Predicted by Variable Diffusivity Model vs. Experimental Data for 325-400 mesh Ilmenite Particles	86
5.1	Compositions of Pyroxenes	89
5.2	Nomenclature of Pyroxenes	89
5.3	View of the Apollo 11 Landing Site	91
5.4	X-Ray Map of Ti, Fe, Si and Ca in Entire Lunar Sample	92
5.5	Relative Location of Lunar Sample on Pyroxene Quadrilateral	93
5.6	Reaction Rate of Lunar Sample compared to Known Simulants	97
5.7	SEM Micrograph of Completely Reduced Fayalite	98
5.8	SEM Micrograph of Completely Reduced Lunar Sample, Particle #3	98
5.9	SEM Micrograph of Partially Reduced Hypersthene	99
5.10	SEM Micrograph of Partially Reduced Lunar Sample, Particle #18	99
5.11	SEM Micrograph of Completely Reduced Lunar Sample, Particle #5	101
5.12	X-Ray Map Detailing Fe, Ti, Si, Ca, Mg and Al for Particle #5	102
5.13	SEM Micrograph of Completely Reduced Lunar Sample, Particle #1	103
5.14	X-Ray Map Detailing Fe, Ti, Mg and Si for Particle #1	103
5.15	Spot X-Ray Analysis for Particle #1	104
5.16	SEM Micrograph of Completely Reduced Lunar Sample, Particle #4	106
5.17	X-Ray Map Detailing Fe, Ti, Si, Mg, Ca and Al for Particle #4	107
5.18	SEM Micrograph of Partially Reduced Lunar Sample, Particle #1	108
5.19	SEM Micrograph of Partially Reduced Lunar Sample, Particle #5	108

LIST OF TABLES

2.1	Reaction Conditions for Hydrogen Reduction of Ilmenite	35
2.2	Reaction Conditions for Hydrogen Reduction of Ilmenite	35
A.1	Hydrogen Reduction of 325-400 mesh Ilmenite at 812 °C	113
A.2	Hydrogen Reduction of 325-400 mesh Ilmenite at 861 °C	113
A.3	Hydrogen Reduction of 325-400 mesh Ilmenite at 910 °C	113
A.4	Hydrogen Reduction of 325-400 mesh Ilmenite at 1012 °C	113
A.5	Hydrogen Reduction of 325-400 mesh Ilmenite at 1080 °C	113
A.6	Hydrogen Reduction of 140-170 mesh Ilmenite at 910 °C Effect of Calcined Pellet	114
A.7	Hydrogen Reduction of 140-170 mesh Ilmenite at 908 °C	114
A.8	Hydrogen Reduction of 100-140 mesh Ilmenite at 812 °C	114
A.9	Hydrogen Reduction of 100-140 mesh Ilmenite at 812 °C Effect of Fines	114
A.10	Hydrogen Reduction of 100-140 mesh Ilmenite at 906 °C	115
A.11	Hydrogen Reduction of 100-140 mesh Ilmenite at 1013 °C	115
A.12	Hydrogen Reduction of 60-70 mesh Ilmenite at 812 °C	115
A.13	Hydrogen Reduction of 60-70 mesh Ilmenite at 1016 °C	115
A.14	Carbon Monoxide Reduction of 325-400 mesh Ilmenite at 917 °C	116
A.15	Carbon Monoxide Reduction of 325-400 mesh Ilmenite at 1016 °C	117
A.16	Carbon Monoxide Reduction of 325-400 mesh Ilmenite at 1115 °C	117
A.17	Carbon Monoxide Reduction of 325-400 mesh Ilmenite at 1167 °C	117

LIST OF TABLES - *Continued*

A.18	Carbon Monoxide Reduction of 100-140 mesh Ilmenite at 919 °C	118
A.19	Carbon Monoxide Reduction of 100-140 mesh Ilmenite at 1016 °C	119
A.20	Carbon Monoxide Reduction of 100-140 mesh Ilmenite at 1114 °C	120
A.21	Carbon Monoxide Reduction of 100-140 mesh Ilmenite at 1173 °C	120
A.22	Carbon Monoxide Reduction of 100-140 mesh Ilmenite at 1121 °C	121
A.23	Carbon Monoxide Reduction of 170-200 mesh Ilmenite at 1120 °C	121
A.24	Hydrogen Reduction of +19 mesh Lunar Soil at 1109 °C	122
A.25	Hydrogen Reduction of 19-20 mesh Lunar Soil at 1109 °C	122
B.1	Particle Size Calculation for 325-400 mesh Particles, #1	123
B.2	Particle Size Calculation for 325-400 mesh Particles, #2	124
B.3	Particle Size Calculation for 170-200 mesh Particles, #1	125
B.4	Particle Size Calculation for 170-200 mesh Particles, #2	126
B.5	Particle Size Calculation for 100-140 mesh Particles	127
B.6	Particle Size Calculation for 60-70 mesh Particles	128

ABSTRACT

The effect of particle size on ilmenite (FeTiO_3) reduction was studied by experimentally determining the intrinsic activation energy and modeling the data using a shrinking core model. The model accounted for both kinetics and ash diffusion control and allowed for a variable diffusivity as a function of conversion.

The intrinsic activation energy was determined by reducing ilmenite particles ranging from 60 to 400 mesh with H_2 and CO partial pressures between .131 and .156 atm over a temperature range of 812 to 1173 °C. The activation energy for hydrogen reduction was found to be 22.3 kcal/mol and the activation energy for carbon monoxide reduction was found to be 16.1 kcal/mol.

INTRODUCTION

Introductory Remarks

As the National Aeronautics and Space Administration (NASA) continues its efforts to build a manned space station on the lunar surface, increased emphasis has been placed on generating the required resources directly from lunar material (McKay and Williams, 1979; Williams and Erstfeld, 1979, Gibson and Knudsen, 1985). This benefits NASA in two ways: first, there are immediate savings which are realized by reducing the overall payload on numerous missions and second, this allows the space station to be self-sufficient (National Commission on Space, 1986).

Oxygen, for use as a propellant or to sustain life, is an immediate requirement of such a space station. Since there is no atmosphere on the moon, oxygen can only be generated by reducing the lunar soil with a relatively strong reducing agent. Thus, by designing a system which is capable of reducing lunar soil while regenerating and recycling the reducing agent, NASA will be able to generate one of the fundamental chemical compounds required by the space station.

Many studies have concentrated on the design of a suitable reactor (Cutler, 1986, Cutler and Waldren, 1992). Although these designs may be feasible, reactors cannot be designed without fully understanding the reaction kinetics. Thus lunar soil or its components must be studied directly to determine the reaction rates.

Lunar soil itself is very different from earth soil. As noted in the Lunar Sourcebook (Heiken et al., 1991), there are two distinct terrains on the Moon with

widely different chemical compositions. The *highlands* or rough lunar surfaces contain lighter elements like calcium and aluminum while the *maria* or smoother surfaces contain more iron and titanium. Mineralogically, the highlands consist predominantly of *feldspar* while the maria is composed primarily of *pyroxenes*.

Pyroxene, feldspar and other lunar minerals, seem to have solidified from a melted state and give rise to compounds that are generally not found on earth. The lunar soil tends to be richer in heavier metals like titanium and zirconium, which have relatively high melting points and contains much less sodium and potassium, which have lower melting points. However, like terrestrial soil, lunar soil contains oxygen complexed with iron and silicon.

Interestingly, oxygen is the most abundant element present on the lunar surface; approximately 45% by weight. Silicon is the second most abundant (21% by weight) followed by calcium, magnesium and iron whose weight percentages change as one moves from the highlands to the maria. Total iron concentration, for instance, ranges from 6% in the highlands to 15% in the maria (Heiken et al., 1991).

The majority of the oxygen is tightly bound to silicate compounds. Silicates, however, tend to react only at extremely high temperatures. Reactions at any significant rate do not occur at temperature below 1000 °C (Massieon, 1992). Similarly, alumina and titanium oxides, while abundant on the lunar surface, are extremely difficult compounds from which to remove oxygen.

Lunar soil is also difficult to study. Although some lunar soil is available for

experimentation, the amount needed to conduct a comprehensive study is unattainable. Thus, previous works have used either terrestrial ores (Wouterlood, 1979; Massieon, 1992) or synthesized lunar simulants (Zhao, 1991; Massieon, 1992).

Terrestrial ores tend to come from two sources. The ore was either discovered to occur naturally on earth or the ore was part of celestial body which fell to earth as a meteorite, for example. Generally, naturally occurring ores are less common and exist in different oxidation states than their lunar equivalents. Furthermore, these ores tend to vary in composition or contain significant impurities, making it difficult to draw conclusions.

Synthesized lunar simulants offer relative purity and abundance compared to terrestrial ores. However, these simulants have not been exposed to the same conditions as lunar soil. Thus, simulants also tend to be in different oxidation states unless special buffers have been used during preparation. Simulants also do not to have the harsh effects of solar winds (Heiken et al., 1991). Nonetheless, when generating fundamental reaction data, lunar simulants are preferred because of their consistent composition and availability.

Of the numerous lunar simulants, most studies have focused on ilmenite (Zhao, 1991; Briggs and Sacco, 1988; Bardi, 1987) although olivine, pyroxene and fayalite have all received attention (Massieon, 1992). Ilmenite tends to be the mineral of choice since it is the most abundant oxide mineral in lunar soil and can produce up to 10.5% oxygen by weight. Ilmenite is also easier to characterize than pyroxenes since

the ilmenite solid solution contains only iron or magnesium.

Reduction experiments on lunar simulants have been relatively limited. These experiments have shown that oxygen bearing minerals that contain iron tend to have lower energy requirements than other oxygen containing compounds (Massieon 1992). In fact, Zhao and Shadman (1991) showed that the diffusion of iron away from the reaction front during ilmenite reduction was a significant feature affecting the process kinetics.

These experiments have also used different reducing agents. Zhao and Shadman (1991) studied the effects of reducing ilmenite with hydrogen, carbon monoxide and carbothermal reduction. Other experiments using methane have also shown that oxygen production is possible (Rosenberg and Wu, personal communication, 1993).

Since it is yet unclear how the reactor will be designed, each reducing agent must be thoroughly investigated so that adequate data is available in the event it is used. Nonetheless, hydrogen and carbon monoxide have received the greatest attention due to their relative ease of use and possible production on the moon (Blanford, 1982; Kiko et al., 1979).

Thus, the basic reactions that have been studied most are ilmenite reduction by hydrogen or carbon monoxide. These reactions are as follows:



The reducing agent and oxygen can then be separated. The reducing agent can be returned to the reactor and the oxygen can be extracted for consumption.

Although these reactions have been previously studied, the kinetics which drive the reaction cannot be understood unless the effect of particle size is known. Previous work (Zhao 1991; Zhao and Shadman, 1990 and 1991) has shown that reduction of ilmenite with hydrogen, carbon monoxide and combinations of these results in first order reactions. Zhao also found that the activation energy using Hydrogen was 22.3 kcal/mol and the activation energy using carbon monoxide ranged from 10.0 to 20.0 kcal/mole.

Zhao's results however were obtained for particles which were 45 microns or less. These particles contained numerous fines which tend to react quickly. Since lunar soil consists primarily of particles which are less than 1 cm in size (Heiken et al., 1991), this analysis is accurate but incomplete. Furthermore, Zhao showed that lunar simulants and lunar soil react by a shrinking core mechanism and produce an ash layer. Thus as the reaction progresses, the ash layer becomes more sizable and diffusion can limit the reaction rate. This could severely limit the rate of reaction for larger particle sizes.

Purpose

The effect of particle size is fundamental to reactor design. An effective reactor cannot be designed without fully understanding the reaction mechanism and the rate at

which the raw materials will react. Oxygen production from lunar simulants has been studied previously, but the rate dependence on particle size has not. Since larger particles tend to take longer to react, it becomes important to understand how much longer a reaction may take and why.

The matter is further compounded by the fact that in any lunar operation, it is unlikely that any reactor feed will be pre-sieved or separated in any way. Efforts by Ramadorai (1992) have essentially shown that beneficiation of iron or ilmenite in lunar samples is currently unfeasible. Thus there is little advantage to pre-treating or pre-sieving lunar soil. As a result, a distribution of particles will likely be used directly in the reactors. The amount of oxygen generated will then depend on the average soil composition, the temperature of reaction and the average particle size. A suitable reactor will have to take these variables into account.

It is also unlikely that there will be any significant mining or crushing operations on the moon initially. Since the upper layer of lunar soil is made up primarily of fines which range in size from sub-microns to centimeters, these particles will probably be used first due to their relative accessibility. However, if mining is required, it is likely that the crushing of large particles will also become necessary. Since crushing will be an energy expenditure and is associated with a cost, there will inevitably be a point of diminishing returns. Accurate determination of this point depends on how particle size affects the rate of oxygen production.

The purpose of this study is to characterize the specific effect of particle size

and to understand how the natural production of an ash layer affects the overall reduction of ilmenite. The verification of the activation energies and the precise effect of particle radius can then be used by future scientists as they endeavor to produce oxygen on the moon.

Method of Approach

The basics associated with particle size are well understood (Levenspiel, 1972; Smith, 1981; Szekely, 1976). However, the application of these models to lunar soil and lunar simulants is not. Depending on the behavior of the reaction, the properties of the reaction components, and the controlling mechanism, the type of model used can be significantly different.

Zhao showed that the reduction of lunar simulants with hydrogen or carbon monoxide follows a shrinking core mechanism. Thus, as a gas molecule approaches an individual particle, it must overcome up to three different diffusional resistances before reacting. The path a gas molecule takes can be broken down as follows:

- Step 1. Mass transfer of gaseous reactant to the vicinity of an individual particle.
- Step 2. Diffusion of gaseous reactant through the film layer surrounding a particle.
- Step 3. Diffusion of gaseous reactant through any ash layer so far accumulated around the particle.
- Step 4. Reaction of gaseous reactant with the unreacted core.

The overall reaction is only as fast as the slowest step. Thus the overall rate is determined by the rate limiting step. As the controlling mechanism changes the

reaction rate can also change. However, unless the previous controlling mechanism disappears, the new rate can only be slower than before. Therefore, most kinetic data tends to be concave down in nature as different mechanisms control the reaction.

In the particular case of ilmenite reduction, mass transport is affected by the orientation of particles and inter-particle diffusion. Film diffusion occurs as the gas approaches individual particles and moves through the surrounding gas film. Ash diffusion occurs as the gas moves through the porous, titanium dioxide, product layer surrounding the unreacted core. Since iron tends to be nonporous, it prohibits any oxygen diffusion

Ideally, the parameters associated with the chemical reaction itself (Step 4) could be studied directly. Experimental data would then directly yield the activation energy and provide the basis for a kinetically controlled, mathematical model. Since the final reactor will be designed differently than the laboratory experiments, the diffusional effects unique to the reactor can always be considered in addition to the kinetic model.

In an effort to study the chemical kinetics directly, the experiments were designed to minimize the effects of the various diffusion steps. However, not all of the diffusional effects can be designed out of the laboratory experiment since some of the effects are inherent to the specific particle which is reacting. In this case, the orientation of the particles, the inter-particle diffusion and the film diffusion are experimentally introduced and can be adjusted, while the ash diffusion and the rate of

chemical reaction are inherent to the system.

A variety of configurations were attempted in order to minimize or eliminate the effect of laboratory induced diffusion. A kinetic model was then developed based the reaction data and the model was modified to account for ash diffusion. The resulting model predicts the time to achieve a certain level of conversion based on the relative effect between ash diffusion and chemical kinetics.

EXPERIMENTAL PROCEDURE AND APPARATUS

Experimental Setup

The experimental apparatus has been schematically shown in Figure 2.1. The reactor system was centered around a CAHN 1000 electronic microbalance. A wire basket made of Nichrome was suspended from one arm of the balance and an equivalent counter weight was suspended from the other arm. The basket was enclosed within a quartz reactor and a counter weight was enclosed within a Pyrex glass attachment.

The quartz reactor was designed to allow nitrogen to enter from above, through the balance. The reducing gas was introduced from a side arm. The gases mixed in the region above the basket and the mixture flowed downward, past the basket. The gaseous reaction products and remaining gas mixture exited through the bottom of the reactor. The gas stream then passed through various analyzers designed to determine the concentration of the reducing gas and the overall flow rate.

A Lindberg furnace with a Proportional/Integral/Differential (PID) controller was positioned below the reactor and could be raised or lowered using a crank assembly. A thermocouple, made of Alumel and Chromel, was used to measure the actual reaction temperature. The thermocouple was attached to the side of the reactor, but was at the same level as the wire basket.

The reactor was assembled by placing an empty basket on the balance hang-down assembly and zeroing the balance. Then, 50 to 200 mg of sieved sample

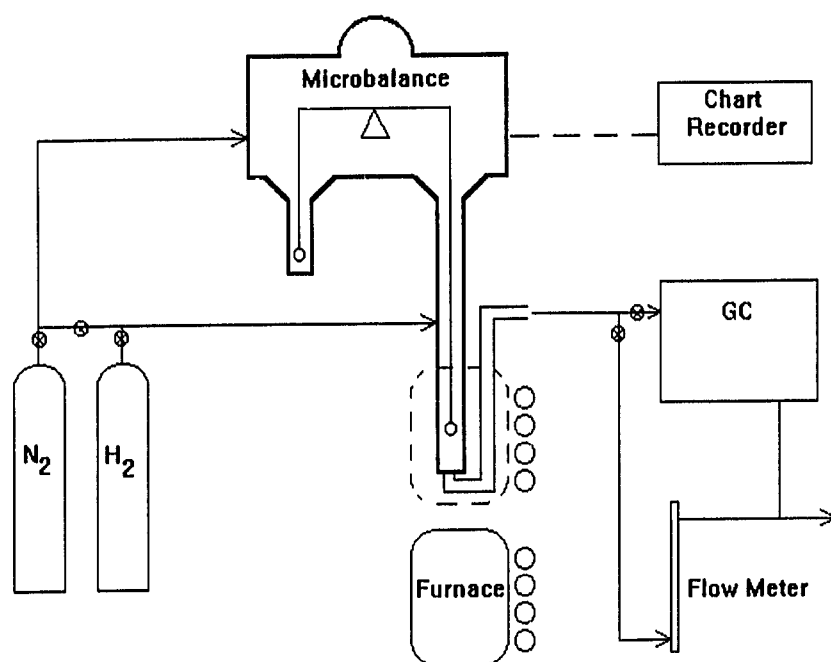


Figure 2.1 Experimental Setup

was placed in the basket and its initial weight was measured. The system was sealed by attaching tubes to the reactor side arms and a nitrogen gas purge was applied for two hours to reduce the level of oxygen within the system. The reducing gas was then introduced through the reactor side arm and the overall gas concentration was measured. Finally, the furnace was raised around the reactor to initiate the reaction.

Specific Equipment

CAHN Electronic Balance

The CAHN 1000 electronic balance has a sensitivity from 1 μg to 100 gm, although all reactions were performed at a sensitivity of 10 mg. The balance operates essentially as an equal arm balance which pivots about the center of a taut ribbon. As weight is applied, a force is generated around the axis of rotation. Using a torque motor, the balance applies a torque which is equal but opposite in direction. As the weight increases, the motor requires more current to counter the weight. Thus current becomes a direct measure of the sample weight.

In the 10 mg operating range used, the balance was tremendously robust and provided excellent stability. However, a stable baseline could not be established for the 1 mg or 1 μg settings. As a result, these settings were never used. It is possible that by elimination of all background influences, a stable baseline might have been established.

The main problems with the balance were its sensitivity to static electricity and

its delicate hang-down wires. Once the basket was placed into the reactor and suspended from the hang-down assembly, static charge could affect the measured weight. Static electricity also affected the centering of the basket within the reactor. A small attraction force close to the top of the reactor caused a large fluctuation in the region around the basket. The balance would no longer record an accurate weight if the basket touched the reactor sides.

Numerous methods were employed to reduce the static charge including briefly raising the furnace, touching the basket to metal prior to placing it in the reactor and spraying the outside of the reactor with ammonia. In the end, ammonia applied with a tissue provided the best results.

The delicate hang-down assemblies were made of Nichrome and could withstand temperatures of 1100 °C. The assemblies were extremely fragile and would break if too much tensile strength was applied. It was found however that super glue adequately repaired the hang-down assemblies until a new part could be ordered.

Varian Gas Chromatograph

The Varian Series 3700 Gas Chromatograph was used to determine the hydrogen concentration within the reaction system. The concentration was determined prior to starting the reaction and could only be monitored before or after the reaction.

The gas chromatograph contained a thermal conductivity detector and two adsorption columns: a mole sieve column and a poropak column. The mole sieve column was used to detect non-polar gases such as hydrogen. Nitrogen was used as the

carrier gas.

The main problem with the gas chromatograph was the relative error between readings. The concentration peaks for the combined nitrogen/hydrogen gas stream varied from 1 to 5% while the calibration gases were relatively consistent. As a result, the concentration of the combined gas stream was not calculated until four consecutive readings within 1% were obtained. This however is no guarantee that the true concentration was measured since this is a precision indication rather than an accuracy measurement. To insure accuracy however, the gas chromatograph was calibrated each day using two primary gas standards.

Infrared CO/CO₂ Analyzer

The CO/CO₂ analyzer, capable of detecting gas concentrations between 1 and 30%, was an IR 702 Gas Analyzer from Infrared Industries Inc. The gas analyzer provided continuous on-line concentration monitoring using a dual beam nondispersive infrared source and photon detectors. The detectors had been calibrated to monitor carbon monoxide and carbon dioxide.

The analyzer was relatively consistent from day to day, requiring only occasional calibration. Nonetheless, the calibration was checked each day using two primary gas standards.

Horiba CO₂ Analyzer

The Horiba CO₂ analyzer was used primarily for its flow meter and as a visual indication as to how much oxygen, in the form of carbon dioxide, was being generated.

The sensitivity of the instrument ranged from the parts per billion level to one percent.

Lindberg Furnace

The Lindberg furnace was capable of providing a steady temperature up to 1200 °C. Since all the reactions were performed at temperatures less than 1180 °C, this furnace was adequate. The heating filaments were made of silicon carbide which were encased in a ceramic to dampen any temperature fluctuations.

The furnace was controlled using a PID controller. The furnace temperature was sensed using a Platinel II thermocouple which provided greater stability than standard Alumel-Chromel thermocouples. Set points were generally achieved within a few minutes after raising the furnace.

Sample and Sample Preparation

Experimental Sample Preparation

The ilmenite sample was obtained from CERAC (stock number I-1056, Lot # 36323 -L -1 +2, -100 mesh). The sample was prepared by subjecting magnetite (Fe_2O_3), iron and titanium dioxide to intense heat for prolonged time periods.

Although the sample was 99.9% pure, larger particles tended to be more porous than smaller particles. CERAC was unable to provide an explanation for this observation. However, it is possible that larger particles were formed both by the fusion of smaller particles and directly from magnetite, iron and titanium dioxide. This may account for the presence of porous particles (formed from smaller particles) and

nonporous particles (formed directly from Fe_2O_3 , Fe and TiO_2). A Scanning Electron Microscope (SEM) picture, included as Figure 2.2, shows the relative non-uniformity of large particles.

The sample was sieved using a mechanical separator and then washed using deionized water. However, due to the tremendous number of fine particles, the sample was re-washed and re-sieved by hand. SEM pictures, shown in Figure 2.3 and 2.4, confirm the reduced number of fine particles due to additional washing. Again, it can be seen that the sample was not uniformly non-porous, but the overall particle size was within the specified sieve range.

Sample Preparation for Analysis

The primary tool for analysis was the SEM by JEOL, which provided exceptional detail at high magnification. However, in order to use the equipment, the sample had to be carefully prepared. Two different mounting techniques were used. The first method was to use a sample mount with a thin film of adhesive. Whole particles could then be attached to the sample stage and coated with carbon or gold prior to observation. This technique was used to study particles which had been subjected to extreme pressure and to determine the relative amount of fines contained within the sample after sieving.

The second more complicated method was to mount the sample in epoxy resin and then polish the surface to expose a sample cross section. Loose samples or individual particles were poured into a plastic clip to concentrate the particles in one

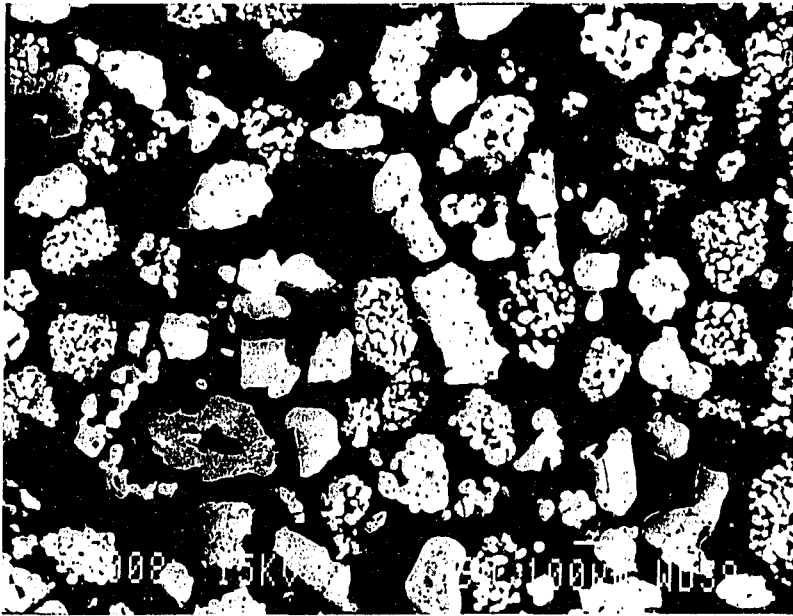


Figure 2.2 SEM Micrograph of Ilmenite Particles greater than 100 μm
(Courtesy of Mr. Xiaoyang Du)

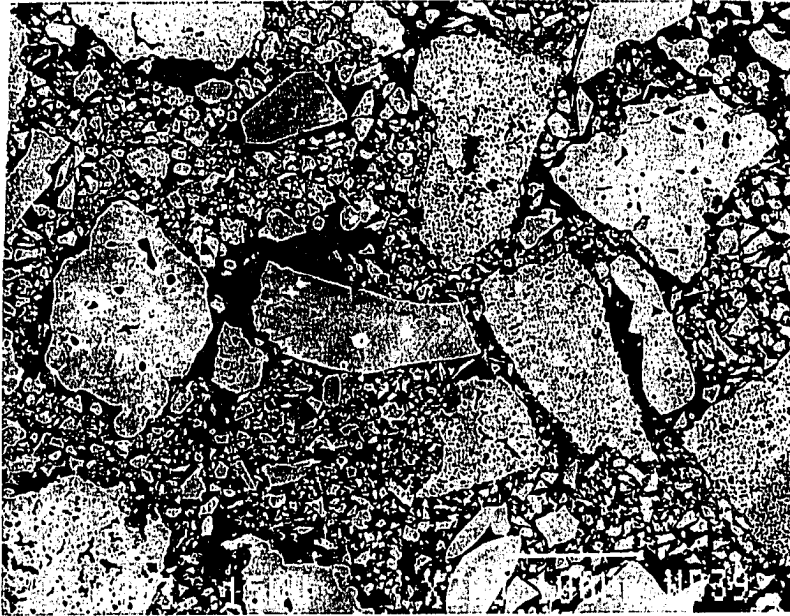


Figure 2.3 SEM Micrograph of Sieved and Washed Ilmenite Particles

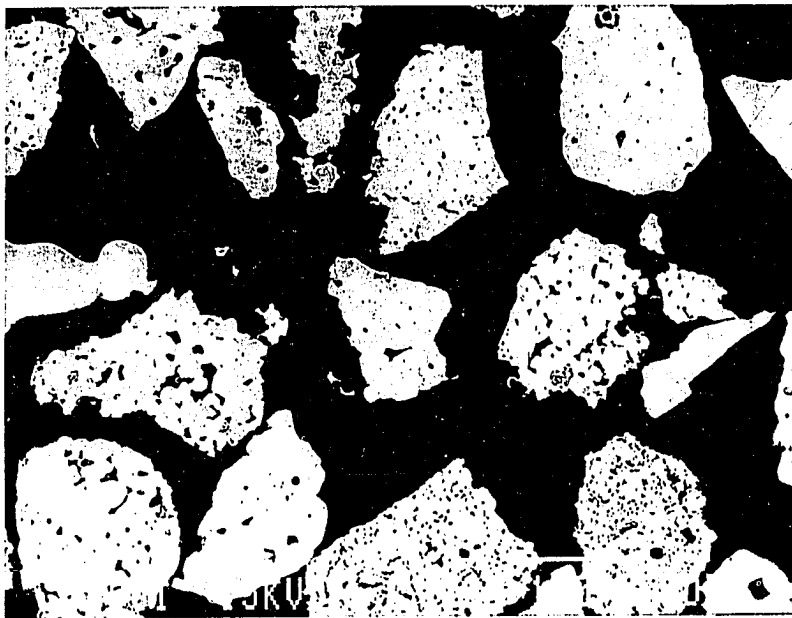


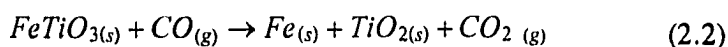
Figure 2.4 SEM Micrograph of Sieved and Superwashed Ilmenite Particles

area and to prevent all the particles from being polished away. Pellets were first cut to expose a cross section and then placed within clips so that the cross section would be at the epoxy surface. The samples were then mounted in epoxy while under vacuum to prevent entrapment of air bubbles. The samples were allowed to cure overnight and the epoxy mount was then polished using an Ecomet 4 automatic polisher or by hand polishing until a relatively scratch free, clear surface was obtained. This polishing technique was required in order to use X-ray analyses.

The SEM was also used to determine the average surface area per unit volume. Using Noran software which accompanied the SEM, two dimensional data showing the particle perimeter and particle area was acquired. This data was then used to solve for the effective surface area per unit volume. The additional surface area due to porous particles was, therefore, taken into account. When these pores were graphically filled the effective radius was further reduced. The particle size data has been included in Appendix B.

Experimental Procedure

Ilmenite can be reduced a variety of ways depending on the reducing gases which are chosen. In the case of hydrogen or carbon monoxide reduction, the respective equations are as follows:



Since the reaction products weigh less than the reactants, the weight loss can be measured and the progress of the reaction can be monitored.

Four different experimental geometries were tested to determine which setup yielded reliable and informative data. The variations occurred in the type of basket used to hold the sample and the form of the unreduced ilmenite. The four different geometries were as follows:

1. using a quartz pan instead of the wire basket and placing a thin layer of loose ilmenite particles within the pan;
2. compressing approximately 100 mg of ilmenite particles into a pellet using a pelletizer. The particles were placed into a stainless steel die and compressed at 10,000 kPa for 1 to 15 minutes. The pellet was removed and cut into a rectangular slab before it was placed in the wire basket for reduction.
3. forming the ilmenite particles into a pellet by adding water and then shaping the thick slurry into a rectangular pellet. The formed pellet was then placed in the wire basket and kept under a nitrogen purge for two hours before it was calcined at 1100 °C. The calcined pellet was then reduced in the wire basket;
4. placing loose ilmenite particles into an open, stainless steel, wire mesh box and then placing the mesh box into the wire basket. Since the openings in the wire mesh used to make the baskets were sometimes greater than the

particle size, two flat pieces of mesh cut at different angles were placed in the bottom of the box. This reduced the average hole size and prevented particles from falling to the bottom of the reactor. Before each box and its accompanying flat pieces were used, they were held under a nitrogen purge for two hours and then subjected to a reducing agent at approximately 1000 °C. A slight weight increase was noted.

Experimental Procedure for Hydrogen Reduction

A series of reactions were performed to determine the effect of particle size on the hydrogen reduction of ilmenite. The reaction matrix has been included as Figure 2.5 and the specific reaction conditions for each have been listed in Table 2.1. The reaction data has been included in Appendix A.

The particle sizes used ranged from 60 to 400 mesh (38-255 μm), the reduction temperatures were varied from 812 °C to 1080 °C, and the hydrogen concentration was varied from 13.34% to 15.55%. The total flow rate was always greater than 597 cc/min which had been shown by Zhao (1991) to eliminate film diffusion effects. The amount of ilmenite reduced ranged from 101.88 mg to 203.44 mg. All particles had been sieved using standard size sieves to insure a uniform particle size and washed with water to remove any fines.

The gas concentration was determined using a Varian Gas Chromatograph and the total flow rate was determined using a bubble meter. The hydrogen gas used was

Hydrogen Reaction Matrix

Temp:	800 °C	850 °C	900 °C	1000 °C	1050 °C
Particle Size					
325-400 (38-45 μm)	T_Run 5	T_Run 11	T_Run 6	T_Run 7	T_Run 12
140-170 (90-106 μm)			Run 3 T_Run 8		
100-140 (106-149 μm)	T_Run 4 T_Run 10		T_Run 2	T_Run 1	
60-70 (210-250 μm)	T_Run 9			T_Run 3	

Figure 2.5 Hydrogen Reaction Matrix for Ilmenite Reduction

Carbon Monoxide Reaction Matrix

Temp:	900 °C	1000 °C	1050 °C	1100 °C	1150 °C
Particle Size					
325-400 (38-45 μm)	CO_Run 6	CO_Run 1		CO_Run 2	CO_Run 5
170-200 (75-90 μm)				CO_Run 11	
100-140 (106-149 μm)	CO_Run 7	CO_Run 4		CO_Run 3 CO_Run 10	CO_Run 9
60-70 (210-250 μm)					

Figure 2.6 Carbon Monoxide Reaction Matrix for Ilmenite Reduction

Run Name	Particle Size (Mesh)	Temperatue (C)	% Hydrogen (%)	Flow Rate (cc/min)	Initial Ilmenite (mg)	% Conversion (%)	Geometry
Run 3	140-170	908	13.15	600	87.19	93.15	Pellet
T_Run 1	100-140	1013	14.77	625	158.87	52.08	Mesh Box
T_Run 2	100-140	906	13.36	721	195.04	27.19	Mesh Box
T_Run 3	60-70	1016	13.34	762	203.59	52.15	Mesh Box
T_Run 4	100-140	812	14.09	769	207.83	45.74	Mesh Box
T_Run 5	325-400	812	15.08		101.88	38.93	Mesh Box
T_Run 6	325-400	910	15.08		115.96	70.69	Mesh Box
T_Run 7	325-400	1012	15.42	619	134.11	63.47	Mesh Box
T_Run 8	140-170	910	13.98	623	198.85	43.37	Mesh Box
T_Run 9	60-70	812	14.34	608	136.58	44.88	Mesh Box
T_Run 10	100-140	812	14.22	597	185.96	44.44	Mesh Box/Fines
T_Run 11	325-400	861	15.55	600	136.62	66.57	Mesh Box
T_Run 12	325-400	1080	14.26	623	100.45	76.32	Mesh Box

Table 2.1 Reaction Conditions for Hydrogen Reduction of Ilmenite

Run Name	Particle Size (Mesh)	Temperatue (C)	% Carbon Monoxide (%)	Flow Rate (cc/min)	Initial Ilmenite (mg)	% Conversion (%)	Geometry
T_CORun 1	325-400	1016	15.0	500	113.45	76.29	Mesh Box
T_CORun 2	325-400	1115	14.8	500	126.50	71.56	Mesh Box
T_CORun 3	100-140	1114	15.0	500	177.26	50.96	Mesh Box
T_CORun 4	100-140	1016	15.0	500	179.46	49.78	Mesh Box
T_CORun 5	325-400	1167	15.0	500	101.40	81.14	Mesh Box
T_CORun 6	325-400	917	15.0	600	98.85	99.13	Mesh Box
T_CORun 7	100-140	919	15.0	600	99.12	64.21	Mesh Box
T_CORun 9	100-140	1173	15.1	350	150.96	11.00	Mesh Box
T_CORun 10	100-140	1121	15.0	300	430.85	13.72	Mesh Box
T_CORun 11	170-200	1120	15.3	320	116.56	93.75	Mesh Box

Table 2.2 Reaction Conditions for Carbon Monoxide Reduction of Ilmenite

99.999% pure.

Experimental Procedure for Carbon Monoxide Reduction

Another series of reactions were performed to determine the effect of particle size on carbon monoxide reduction of ilmenite. The reaction matrix has been included as Figure 2.6 and the specific reaction conditions for each run have been listed in Table 2.2. The reaction data has been included in Appendix A.

The particle sizes used ranged from 100-400 mesh (38 - 149 μm), the reduction temperatures were varied from 920 $^{\circ}\text{C}$ to 1172 $^{\circ}\text{C}$, and the carbon monoxide concentration was varied from 14.8% to 15.3%. The total flow rate was always greater than 300 cc/min which had been shown by Zhao (1991) to eliminate film diffusion effects. The amount of ilmenite reduced ranged from 71.88 mg to 203.44 mg. All particles had been sieved using standard size sieves to insure a uniform particle size and washed with water to remove any fines.

The gas concentration was determined using an Infrared CO/CO₂ Gas Analyzer and the total flow rate was determined using a flow meter incorporated in the Horiba CO₂ analyzer.

Observations

As mentioned in the *Introduction* under *Method of Approach*, the desire was to directly measure the kinetics of ilmenite reduction. To this end, it was important to eliminate any experimentally introduced diffusional effects. Different geometries were

used to identify the advantages each method had over another in eliminating diffusional resistances. A method was deemed to be better if, under similar conditions, it yielded a higher rate of reaction and was easier to use.

The pan and mesh box had the advantage of ease. Loose particles were simply placed into the holder, suspended in the reactor, and then reacted immediately after the two hour nitrogen purge. The mesh box however required a certain amount of preparation and design. Furthermore, each box could only be used between one and five times before it became too brittle and broke. The quartz pan was designed and supplied by the glass shop.

Pelletizing required time and was not easy. The pelletizer required up to 15 minutes per pellet and frequently the pellets would break as they were removed from the die. The most successful pellets actually came at reduced pressures for shorter periods of time. Even then, extreme care had to be taken with the fragile pellets.

Similarly, calcining was also time consuming. Forming the pellets was only moderately difficult. The pellets were then purged for two hours before calcining. These formed pellets were approximately 6 mm by 5 mm by 1 mm compared to die pellets which were 8 mm by 6 mm by .2 mm.

Experimentally, the quartz pan yielded the lowest rate of reaction. When compared to a similar reaction using a die pellet, the reaction rate was notably slower. This lower rate is due to the fact that gas can only approach the ilmenite particles from the top of the pan. This restricted mass transfer and created a concentration gradient.

The relative rates between the pan and pellet have been shown in Figure 2.7.

The die pellet offered uniform conversion since gas was able to flow around the entire pellet facilitating mass transfer. However, as Figure 2.8 shows, no particle size effect was observed when different size particles were used. Using the SEM, it was determined that pelletizing caused severe crushing. Figures 2.9 and 2.10 show the result of subjecting the particles to severe pressure. Thus, different particle sizes were being crushed to one uniform size and hence the reaction rates were identical.

The calcined pellet had the distinct advantage of showing a particle size effect. The pellet thickness was a concern, since a concentration gradient could develop. However, the data show that the pellet was porous enough so that no significant diffusional resistance was introduced from the edge of the pellet to the center. This conclusion is supported by Figures 2.11, 2.12, and 2.13 which show an overall pellet cross section, an edge particle and a center particle of partially reduced ilmenite, respectively. These figures show that there is no reaction front and that both edge and center particles have been well converted despite the short reaction time.

The mesh basket yielded slightly higher rates than the calcined pellet and still allowed for a particle size effect. When the reaction rates using a mesh basket were compared to those using a calcined pellet, the reaction rates were initially identical but differed at higher conversions. These results have been shown in Figure 2.14. The observed difference is within the experimental margin of error.

As with the calcined pellet, the mesh box did not introduce any diffusional

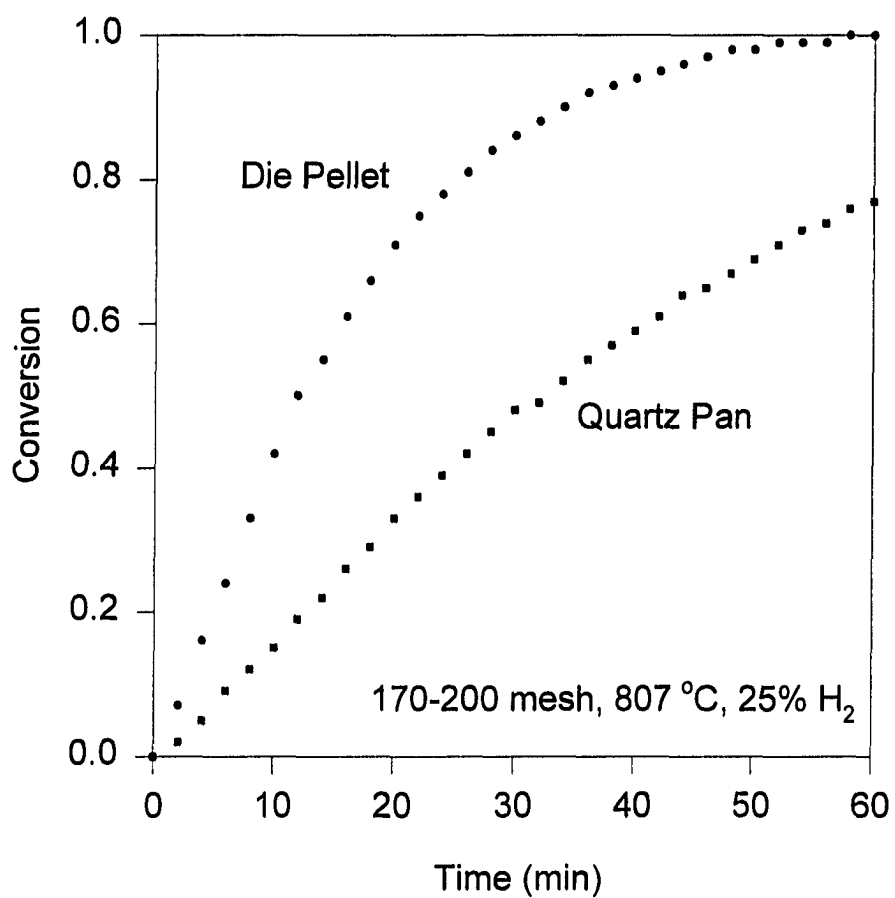


Figure 2.7 Reaction Rates using a Quartz Pan vs. a Die Pellet

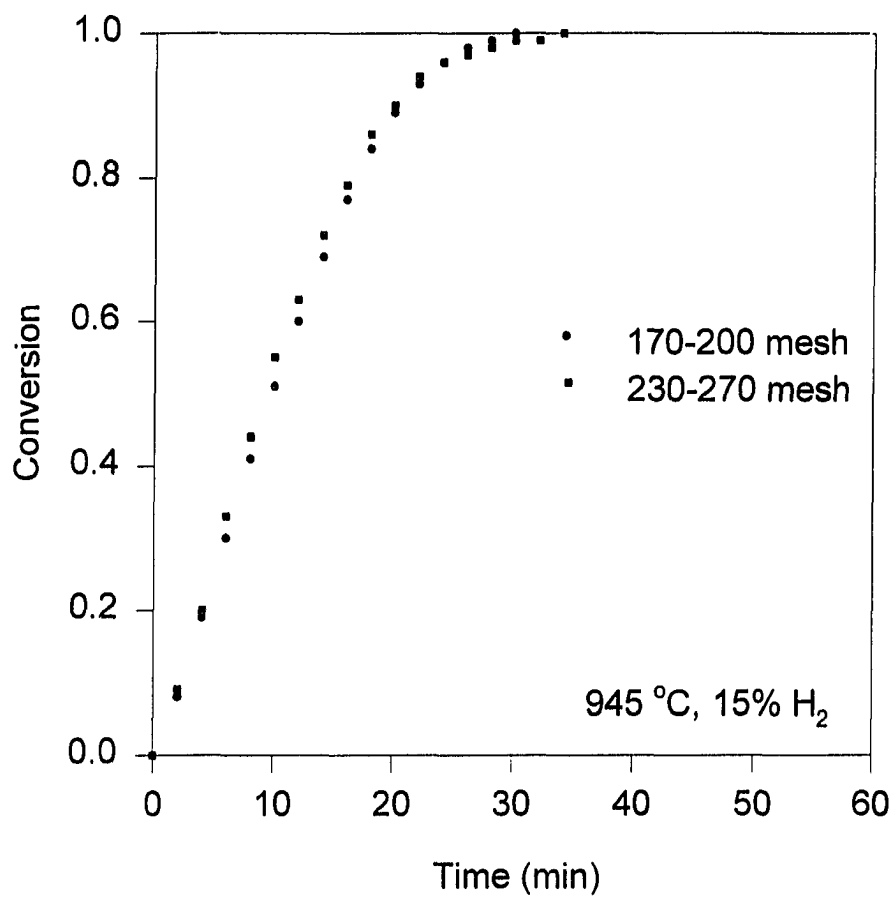


Figure 2.8 Reaction Rates using a Die Pellet



Figure 2.9 Effect of Die Pelletizing on Ilmenite Particles

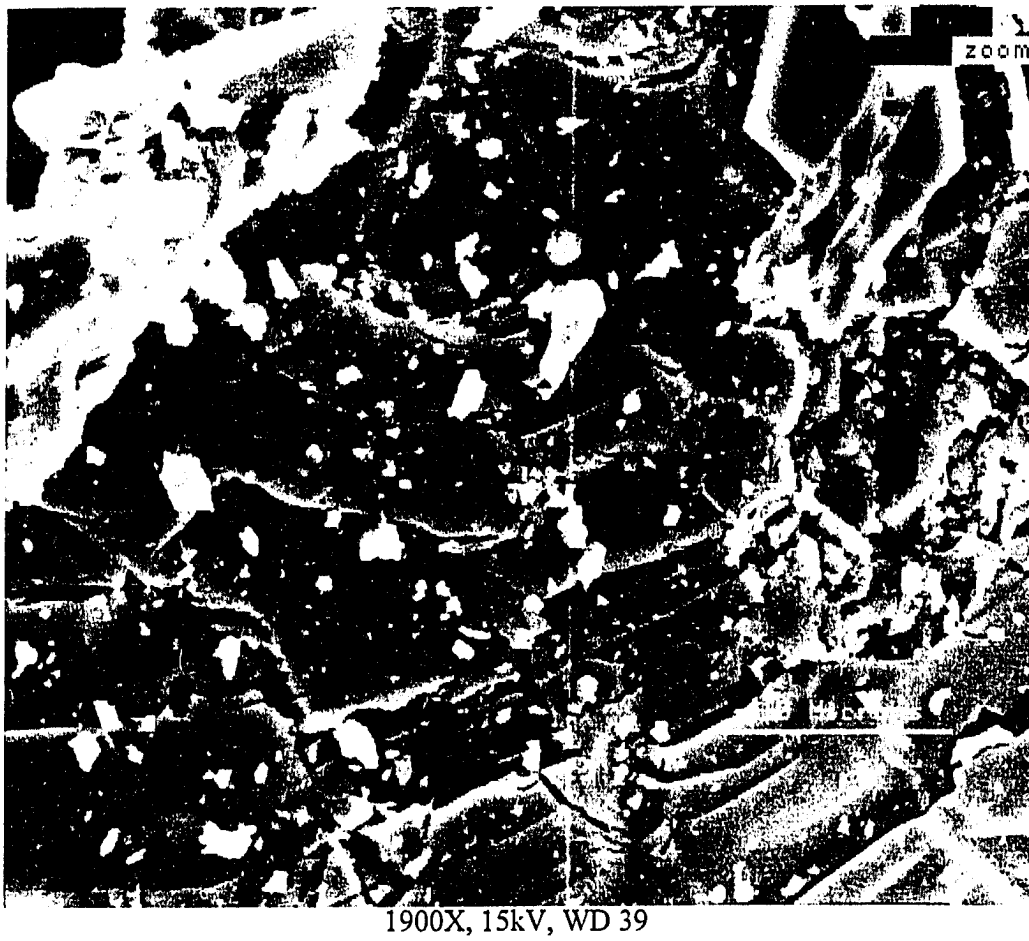


Figure 2.10 Effect of Die Pelletizing on Ilmenite Particles

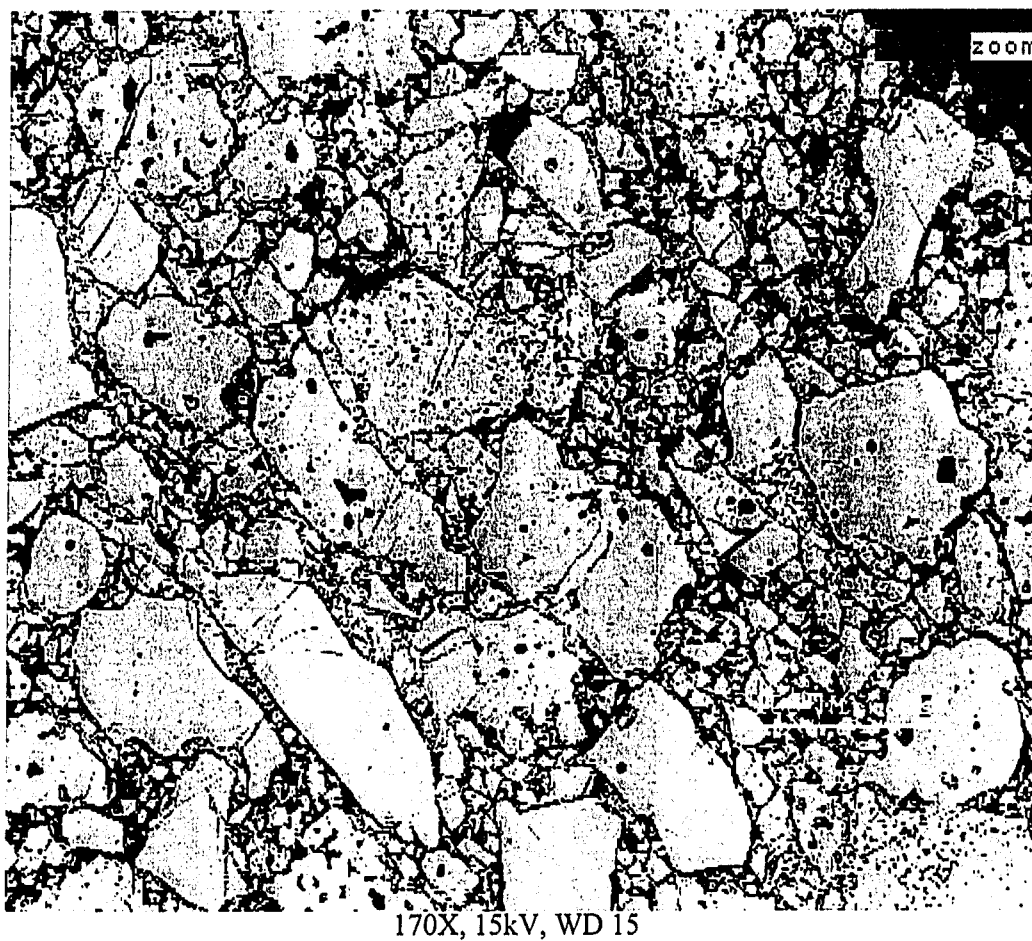


Figure 2.11 Overall Cross Section of a Partially Reduced Ilmenite Pellet

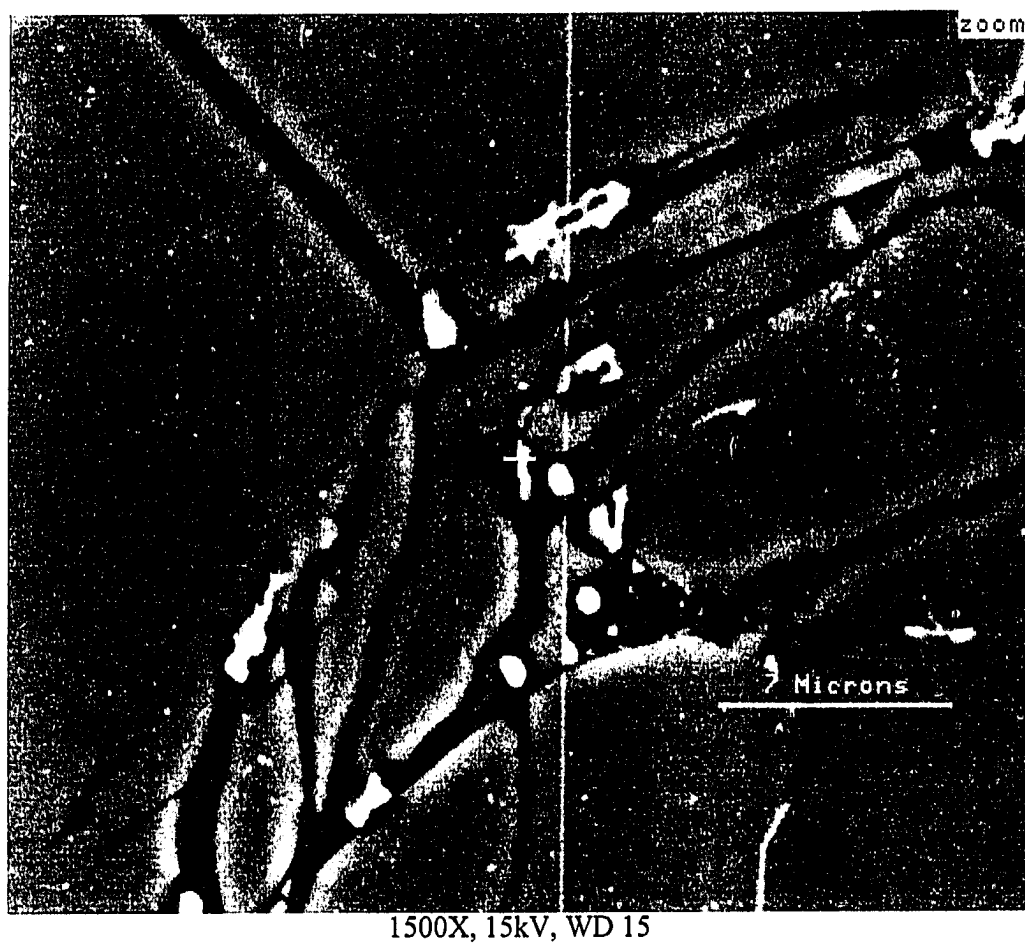


Figure 2.12 Edge Particle of a Partially Reduced Ilmenite Pellet

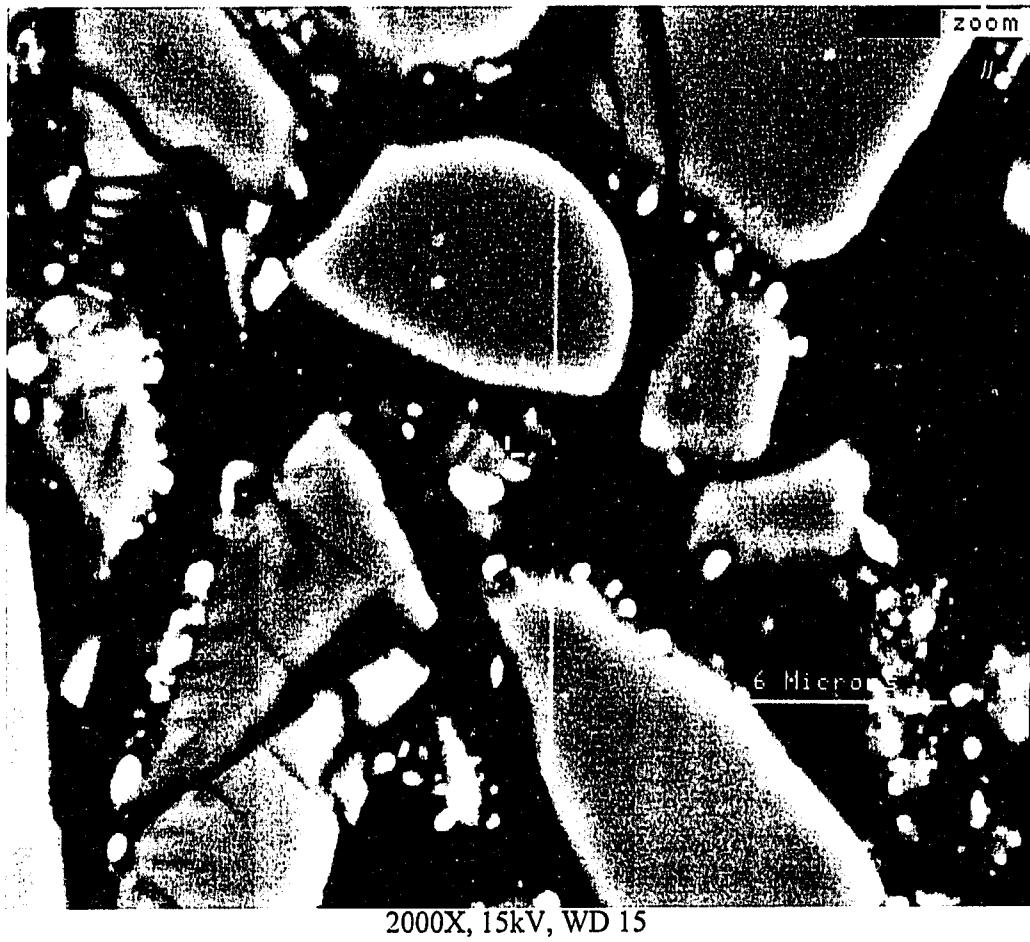


Figure 2.13 Center Particle of a Partially Reduced Ilmenite Pellet

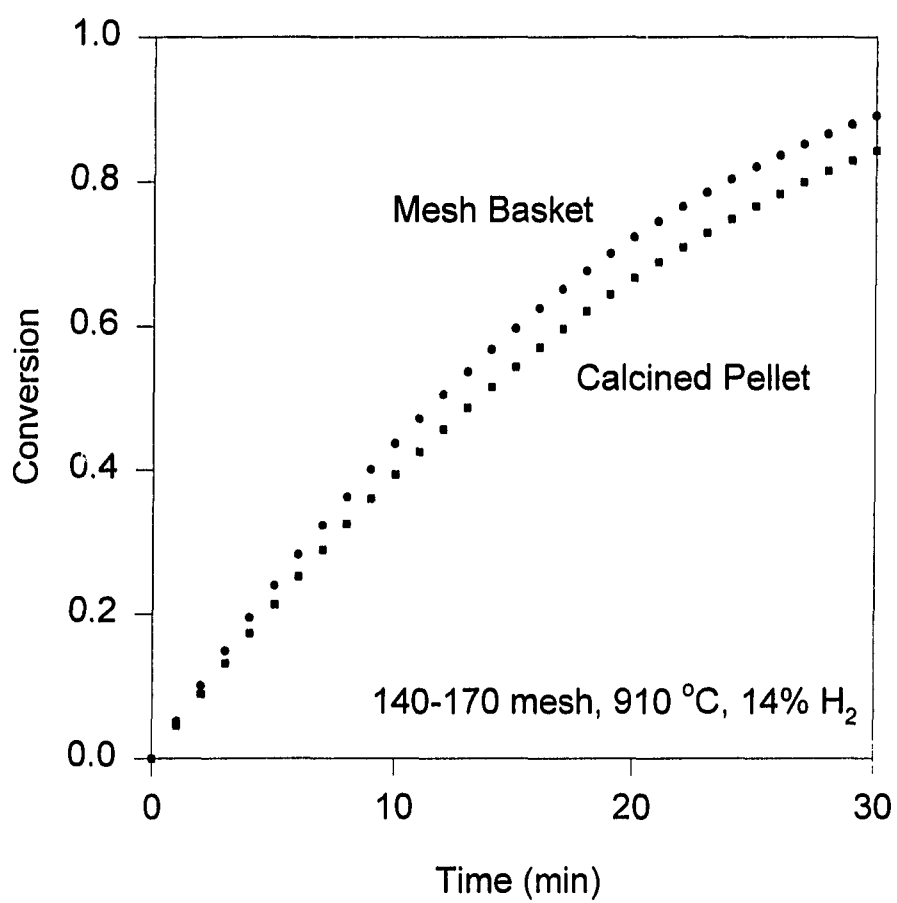


Figure 2.14 Reaction Rates using a Mesh Basket vs. a Calcined Pellet

resistance. Two runs using carbon monoxide, with different flow rates and substantially different amounts of ilmenite, were made. As Figure 2.15 shows, the runs were nearly identical. Thus geometric differences had little effect on the reaction. This data also shows the reproducibility of the data.

The mesh box was also used to examine the effect of fines on the reaction rate. Figure 2.16 shows that samples that contain fines reacted at substantially higher rates than washed samples. Thus re-washing the ilmenite samples with water was necessary in order to collect accurate data.

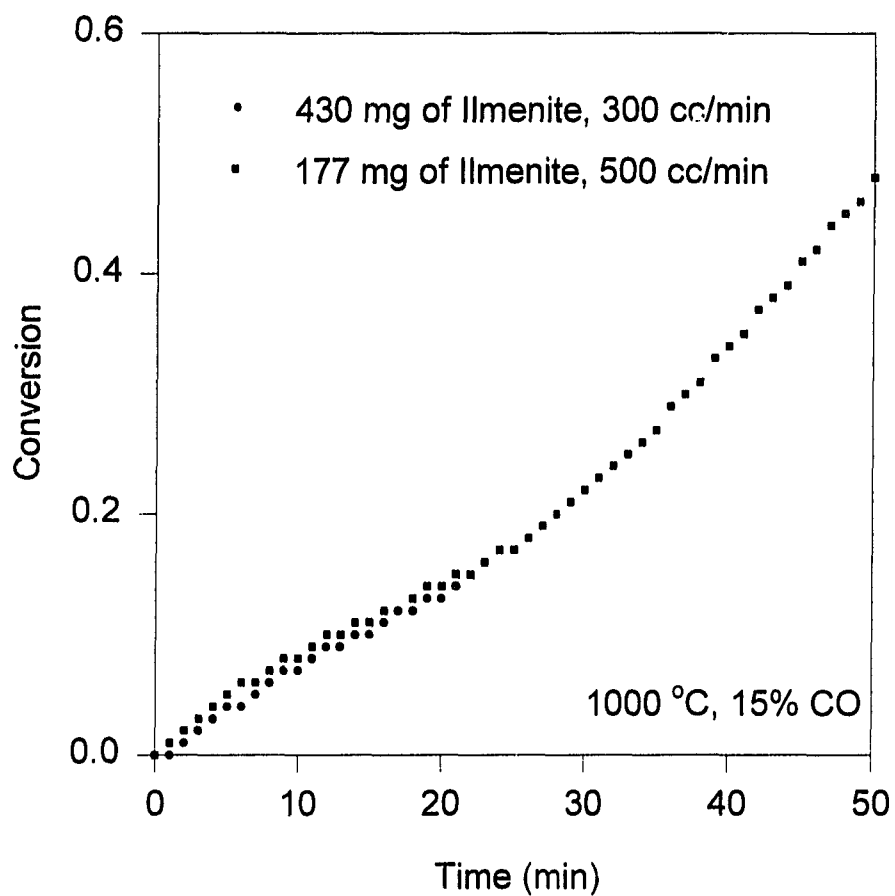


Figure 2.15 Effect of Flow Rate and Sample Mass using a Mesh Basket

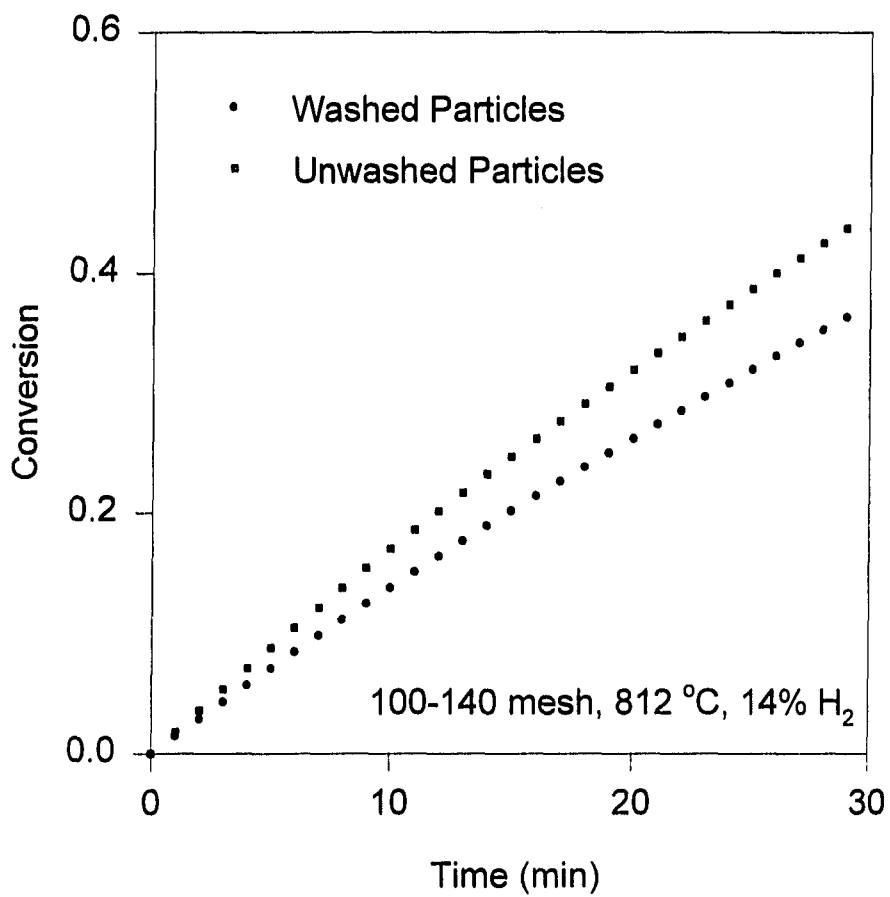


Figure 2.16 Effect of Fines on Reaction Rates

REDUCTION OF ILMENITE WITH HYDROGEN

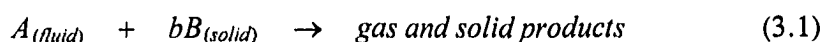
Experimental Apparatus

The experimental apparatus has been shown schematically in Figure 2.1 and the reaction matrix followed has been shown in Figure 2.5 and Table 2.1. The reactions were primarily conducted by placing loose ilmenite particles in a wire mesh box and suspending the box in the wire basket. The reaction data has been included in Appendix A.

Modeling

The reaction could be controlled by mass transfer, film diffusion, ash diffusion or chemical kinetics. In the case of hydrogen, the modeling simplifies since both mass transfer and film diffusion can be eliminated based on observations earlier. Furthermore, ash diffusion is less significant since the hydrogen molecule is small in size. Thus the model is based on the hypothesis that chemical kinetics is the controlling mechanism.

Hydrogen reduction of ilmenite is described by the chemical reaction given earlier in Equation 1.1. This reaction is equivalently written as:



where b is the stoichiometric coefficient and in this particular case is equal to one.

As shown in Levenspiel, if the reaction is unaffected by ash diffusion, the quantity of material reacting is proportional to the unreacted solid surface area. Since hydrogen and ilmenite react on an equimolar basis, the rate of hydrogen disappearance

is equal to the rate of ilmenite reduction. Thus, the rate at which moles of B react can be written as:

$$-\frac{1}{4\pi r_c^2} \frac{dN_A}{dt} = -\frac{b}{4\pi r_c^2} \frac{dN_B}{dt} = bk_s C_A \quad (3.2)$$

where N_A , N_B and C_A are the moles of A , B and concentration of A respectively. The rate coefficient is given by k_s and r_c is the radius of the unreacted core. By maintaining a constant hydrogen concentration and monitoring the sample weight as a function of time, the rate coefficient (k_s) can be determined.

The above differential equation can be solved by relating the moles of B to the particle radius. Since $N_B = \rho_B V$, and $dN_B = \rho_B dV$, by relating volume to radius, the above equation becomes

$$-\rho_B \frac{dr_c}{dt} = k_s C_A \quad (3.3)$$

Integrating the left hand side from the original particle radius, R , to the radius of the unreacted core, r_c , and integrating the right hand side from 0 to t yields,

$$t = \tau_k (R - r_c) \quad (3.4)$$

where

$$\tau_k = \frac{\rho_B R}{k_s C_A} \quad (3.5)$$

in terms of conversion, X_B ,

$$t = \tau_k \left[1 - (1 - X_B)^{\frac{1}{3}} \right] \quad (3.6)$$

The intrinsic activation energy (E) can be found plotting the conversion function versus time and using a linear regression program to solve for the slope. Since the slope is equal to τ_k , the rate constant, k_s , can be determined for a specific temperature.

By solving for k_s at a series of different temperatures, the activation energy, E , can be determined by using the Arrhenius law,

$$k_s = k_0 \exp\left(\frac{-E}{RT}\right) \quad (3.7)$$

where k_0 is the frequency factor and T is temperature. A plot of $-\ln(k_s)$ versus T^{-1} yields a straight line with slope $-E/R$.

Once the intrinsic activation energy is known, the rate coefficient can be determined for any temperature and the reaction rate can be predicted. The particle size effect can be obtained by modifying τ_k to include the new particle radius.

Results

A particle size effect, as shown in Figure 3.1, was observed. As expected, the reaction rate was slower for larger particles. The activation energy was calculated by varying the temperature between 812 °C and 1080 °C over five runs. Each run was performed using 325-400 mesh particles and approximately 15% hydrogen. The results of these runs are shown in Figure 3.2.

The activation energy was subsequently calculated by preparing an Arrhenius plot (Figure 3.3) for the same five runs. The activation energy for hydrogen reduction of ilmenite was found to be 22.3 kcal/mol and the frequency factor (k_0) was found to be 4,335 cm/min. The fact that all five points essentially fell on a straight line, further reinforced the conclusion that the experiments were entirely kinetically controlled. Had the activation energy line been concave down, that would have been an indication of diffusional control at higher temperatures.

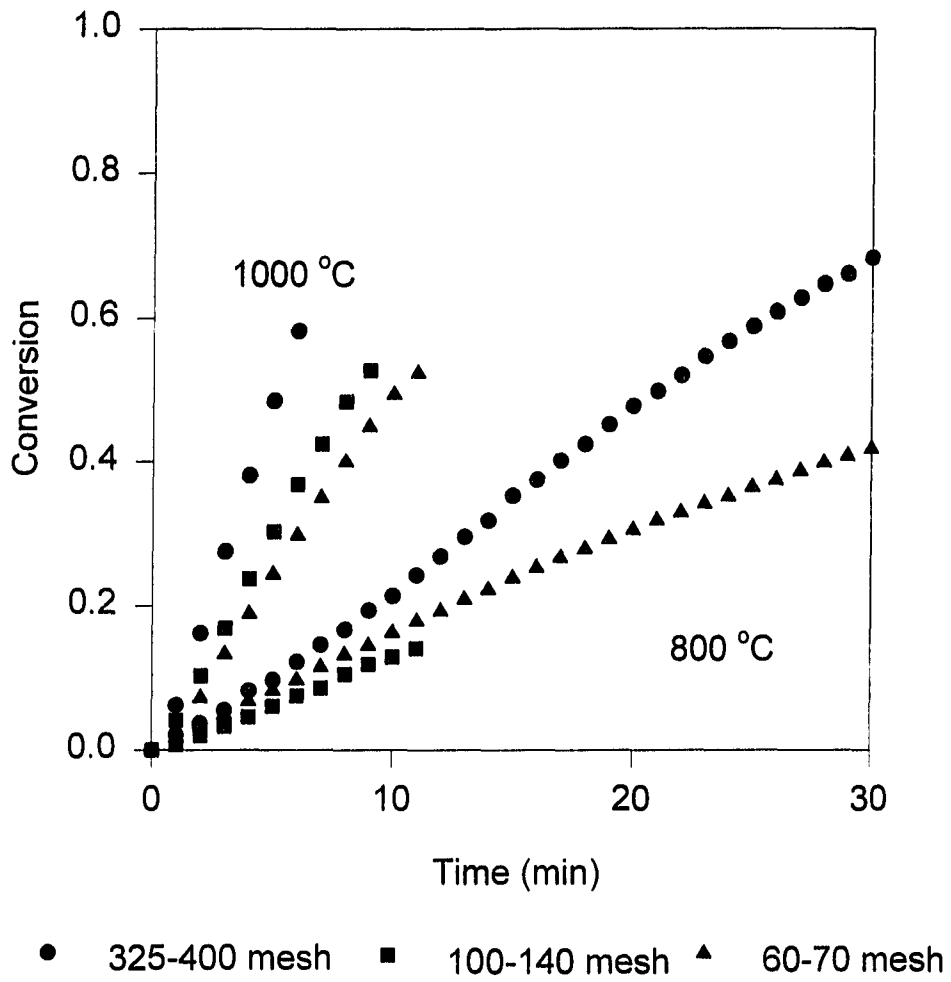


Figure 3.1 Effect of Particle Size on Ilmenite Reduction using Hydrogen

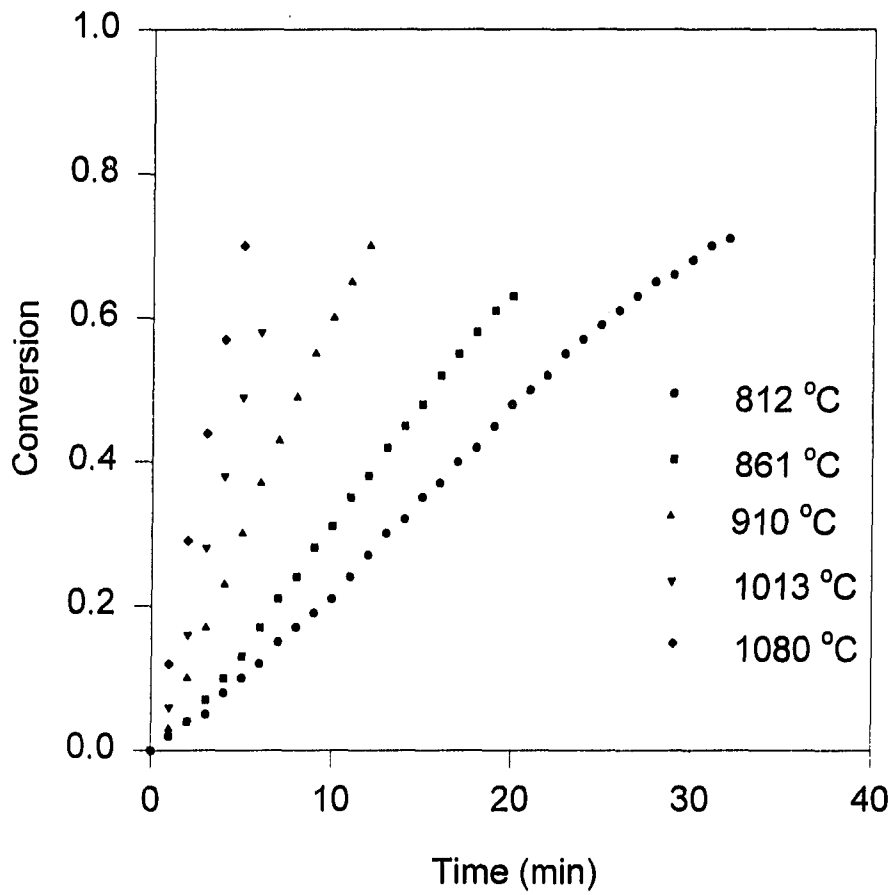


Figure 3.2 Effect of Temperature on 325-400 mesh Ilmenite Particles

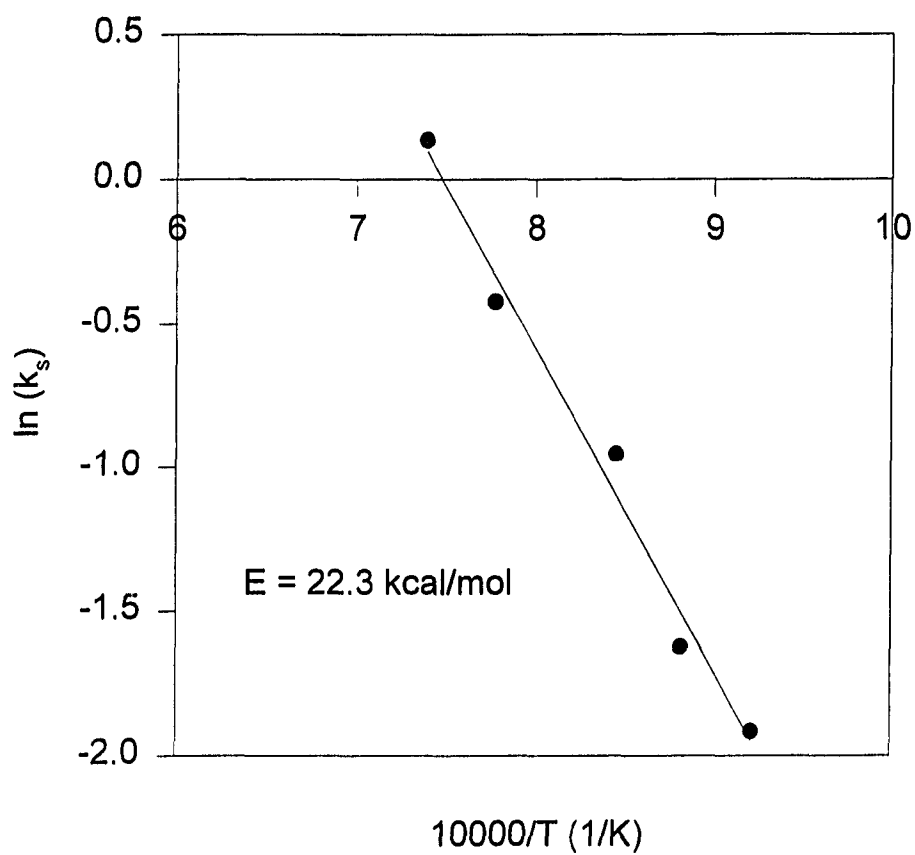


Figure 3.3 Arrhenius Plot for 325-400 mesh Ilmentite Particles using Hydrogen

The reaction was found to be well predicted using a shrinking core model (SCM). Figure 3.4 shows an SEM micrograph of a partially reduced ilmenite sample. The figure shows the characteristic iron accumulation and slight particle fracturing. No significant ash or pellet diffusion was observed using 325 mm particles. Reaction data for larger molecules, using hydrogen, is also surprisingly unaffected by ash diffusion.

Discussion

The reduction process can be considered in three distinct phases. Initially, the reduction is characterized by a relatively slow induction phase. This is followed by a steep reaction phase where the reaction rate reaches a maximum. Finally, the reaction is quenched as the ilmenite becomes fully reduced and the reaction rate levels off to zero.

Unlike reduction of ilmenite with carbon monoxide, the hydrogen induction phase is relatively short, and at high temperatures is essentially nonexistent. Furthermore, as particle size increases, the induction phase does not become prominent as it does with carbon monoxide. As a result, all the reactions were completed in relatively short time periods.

Using the activation energy and frequency factor reported above, the SCM was used to compare predicted values to experimental data (Figure 3.5). Slight deviations from experimental values were expected since the SCM does not consider porous particles and does not take the observed particle breakage into account. Furthermore,



Figure 3.4 Partially Reduced Ilmenite

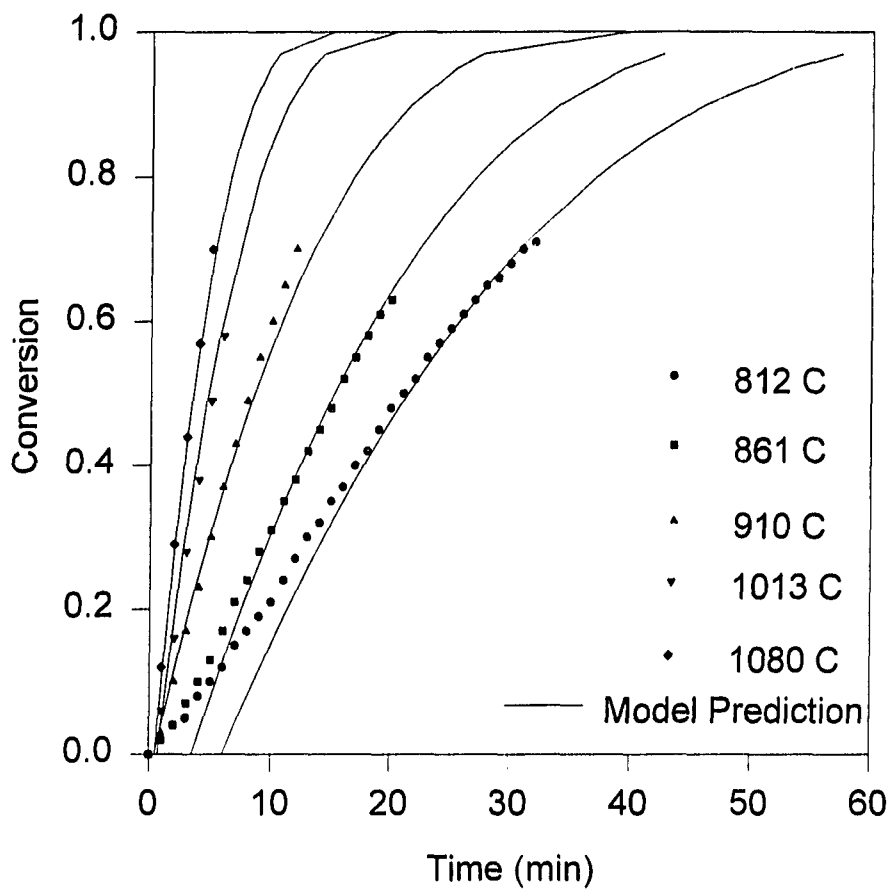


Figure 3.5 Reaction Rate Predicted by Model vs. Experimental Data for 325-400 mesh Ilmenite Particles

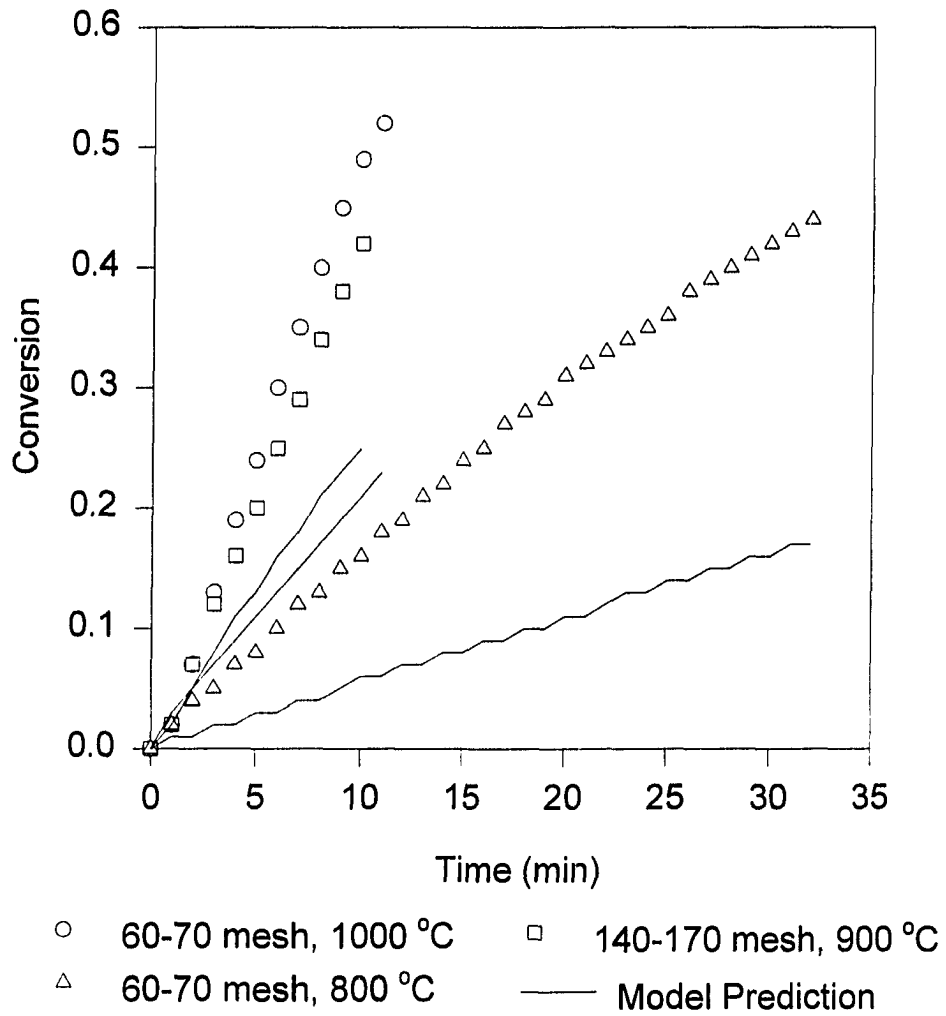


Figure 3.6 Model Prediction for Larger Ilmenite Particles

the induction phase, most prominent in the 812 °C case, was neglected since this region is not kinetically controlled and is not predicted by the model. This matter is considered in further detail in the following chapter. Nonetheless, the SCM provides a reasonably good fit to the experimental data.

However, when the model was used to compare predicted values to experimental data for large particle sizes, the fit was not as good. In fact, Figure 3.6 shows that the model actually under predicts the overall rate. This was an indication that parameters used in the model were not accurate.

The discrepancy was explained by studying SEM photographs and finding that the effective radius was actually less than predicted from the sieve sizes. By performing a particle size analysis on the SEM's Noran Operating System, values for perimeter length and solid area were obtained. The ratio of area to perimeter times two gave an average effective particle radius that was smaller than the original particle radius. This occurs because the volume to surface area ratio decreases as the exposed surface area increases. The particle size data has been included in Appendix B. When the model is adjusted to include the effective radius, the model accurately predicts the experimental results as shown in Figure 3.7 and 3.8.

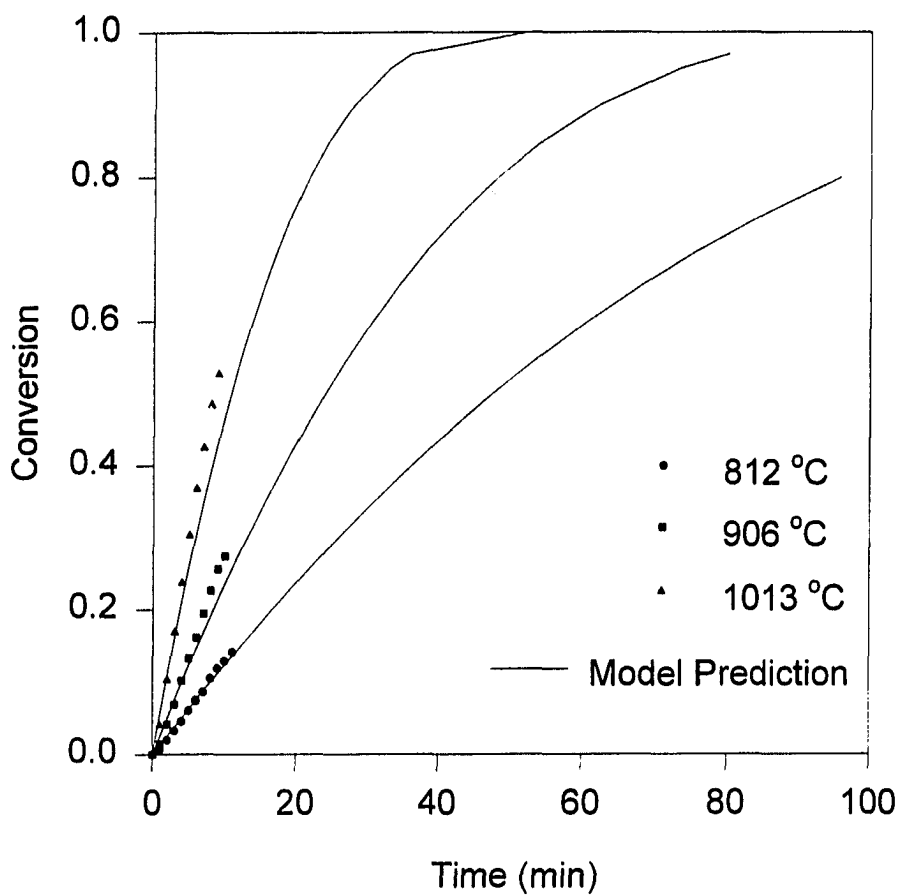


Figure 3.7 Reaction Rate Predicted by Model vs. Experimental Data for 100-140 mesh Ilmenite Particles

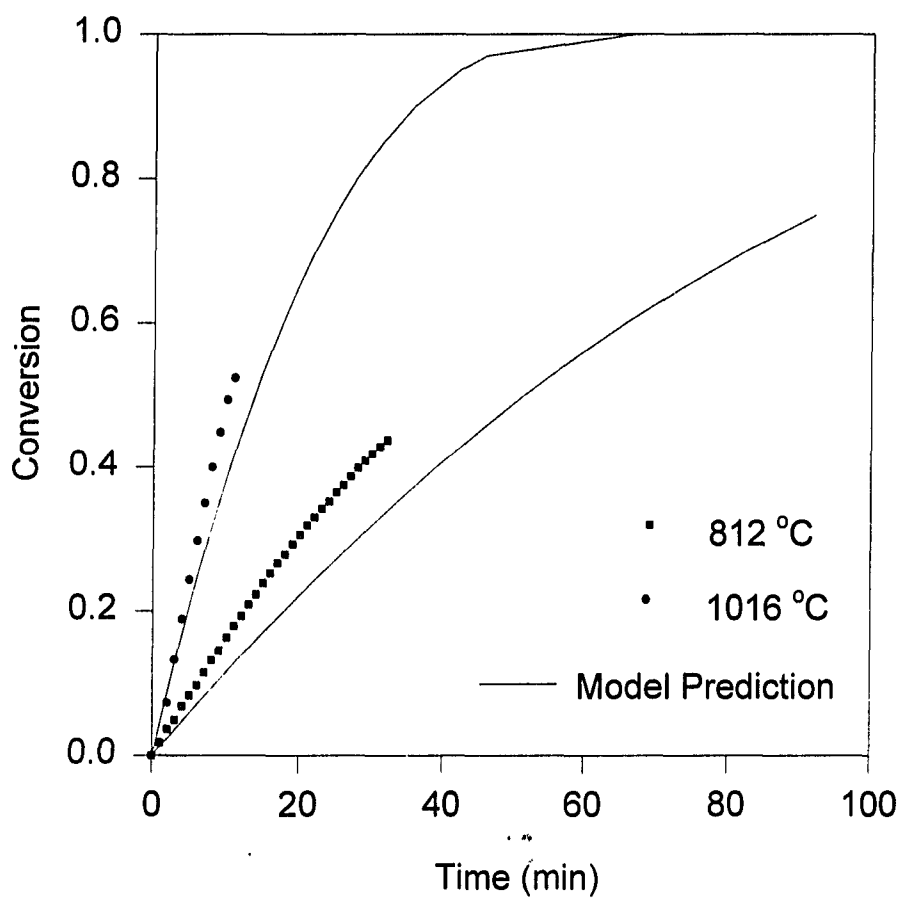


Figure 3.8 Reaction Rate Predicted by Model vs. Experimental Data for 60-70 mesh Ilmenite Particles

REDUCTION OF ILMENITE WITH CARBON MONOXIDE

Experimental Apparatus

The experimental apparatus has been shown schematically in Figure 2.1 and the reaction matrix followed has been shown in Figure 2.6 and Table 2.2. The reactions were primarily conducted by placing loose ilmenite particles in a wire mesh box and suspending the box in the wire basket. The reaction data has been included in Appendix A.

Modeling

As with hydrogen reduction, the reaction could be controlled by mass transfer, film diffusion, ash diffusion or chemical kinetics. In the case of carbon monoxide, the model does not simplify tremendously since only mass transfer and film diffusion can be eliminated based on observations made earlier.

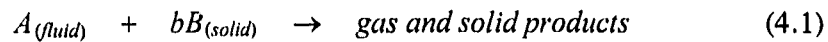
The model is further complicated by the fact that the carbon monoxide induction phase is tremendously long and is concave up. This indicates that the model either contains an exponential or power function or some parameter within the chemical or ash diffusion model is changing as the reaction progresses.

Two models for carbon monoxide reduction of ilmenite can be developed using two different approaches. The models are consistent in the asymptotic case but differ in the assumptions upon which they are based. The first, more simplistic model is formulated quite like the hydrogen model was developed. In this case, since both ash

and kinetics contribute to limit the overall reaction, both models are used additively. The second model, which has not yet been fully developed, is based on first principles and contains a variable diffusivity. The development of both models is shown below.

Model 1:

The reduction of ilmenite by Carbon Monoxide can be described by the chemical reaction given earlier in Equation 1.2. This reaction is equivalently written as:



where b is the stoichiometric coefficient and in this particular case is equal to one. By parallel development to the hydrogen model, a kinetically controlled model can be found to have the form:

$$t = \tau_k \left[1 - (1 - X_B)^{\frac{1}{3}} \right] \quad (4.2)$$

where

$$\tau_k = \frac{\rho_B R}{k C_{A,1}} \quad (4.3)$$

In order to develop the ash diffusion model, the rate at which the core shrinks is equated to flow of gas which diffuses through the ash layer and reaches the core. Thus, as shown in Levenspiel,

$$-\frac{dN_A}{dt} = -\frac{dN_B}{dt} = 4\pi r_c^2 Q \quad (4.4)$$

where N_A and N_B are the moles of A and B respectively and r is the radius. Q is the flux of A through the ash layer and can be represented by Fick's law of equimolar counter diffusion making the equation:

$$-\frac{dN_B}{dt} = 4\pi r_c^2 D_e \frac{dC_A}{dr} \quad (4.5)$$

where D_e is the effective diffusivity of the gaseous reactant through the ash layer and C_A is the concentration of A in the bulk. In order to simplify this expression, it is assumed that the rate at which the core shrinks is slower than the flow rate of A . Thus the LHS of Equation 4.5 is essentially constant. Assuming constant diffusivity, the above differential equation can be solved to yield,

$$-\frac{dN_B}{dt} \left(\frac{1}{r_c} - \frac{1}{R} \right) = 4\pi D_e C_A \quad (4.6)$$

The moles of B can now be eliminated by relating N_B to the particle radius. Since the moles of B are equal to the molar density of the particle times the particle volume and the particle volume is a function of radius, Equation 4.6 can be rewritten as,

$$-\rho_B r_c^2 \left(\frac{1}{r_c} - \frac{1}{R} \right) \frac{dr_c}{dt} = D_e C_A \quad (4.7)$$

Integrating the left hand side between the original particle radius, R , and the radius of the unreacted core, r_c , and integrating the right hand side between 0 and t yields,

$$t = \tau_a \left[1 - 3 \left(\frac{r_c}{R} \right)^2 + 2 \left(\frac{r_c}{R} \right)^3 \right] \quad (4.8)$$

where

$$\tau_a = \frac{\rho_B R^2}{6 D_e C_A} \quad (4.9)$$

Equation 10 can be rewritten in terms of X as,

$$t = \tau_a \left[1 - 3(1 - X_B)^{\frac{2}{3}} + 2(1 - X_B) \right] \quad (4.10)$$

Since both ash diffusion and chemical kinetics are controlling the reaction, the time for the overall reaction can be found by summing the times of the individual controlling steps. Thus the complete model is given by,

$$t = \frac{\rho_B R}{k_s C_A} \left[1 - (1 - X_B)^{\frac{1}{3}} \right] + \frac{\rho_B R^2}{6 D_e C_A} \left[1 - 3(1 - X_B)^{\frac{2}{3}} + 2(1 - X_B) \right] \quad (4.11)$$

Again, by monitoring the sample weight as a function of time, the two coefficients in the above equation can be fit to conversion versus time data. The first coefficient can be used to determine the rate coefficient (k_s) and the second coefficient can be used to solve for the diffusivity (D_e).

As with hydrogen, the rate coefficient can be used to find the intrinsic activation energy (E). Once the intrinsic activation energy is known, the rate coefficient can be determined for any temperature and the reaction rate, assuming a constant diffusivity, can be predicted. The particle size effect can be obtained by modifying τ_k and τ_a to include the new particle radius.

Model 2:

The flux equation of continuity can be simplified by assuming there is no θ or ϕ dependence. Furthermore, by assuming the pseudo-steady state approximation holds, there is no concentration dependence upon time. Thus the equation of continuity becomes.

$$\frac{1}{r^2} \frac{\partial}{\partial r} (r^2 Q_{Ar}) = 0 \quad (4.12)$$

subject to the boundary conditions,

$$\begin{aligned} \text{BC. 1 when } r = R, C_A &= C_{A(\text{bulk})} \\ \text{BC. 2 when } r = r_c, \left(\frac{\partial C_A}{\partial r} \right)_{r=r_c} &= \left(\frac{k C_A}{D_e} \right)_{r=r_c} \end{aligned}$$

where r is the position coordinate, R is the particle size, r_c is the position of the unreacted core, and Q_{Ar} is the flux of component A in the r direction and can be represented by Fick's law of diffusion.

After converting Equation 4.12 into non dimensional form, integrating and determining the coefficients of integration using the boundary conditions, the concentration gradient, Γ , is given by,

$$\Gamma = \frac{1}{\xi} \left(\frac{-k_s R F_p z^2}{D_e + k_s R F_p z - k_s R F_p^2 z^2} \right) + \frac{D_e + k_s R F_p z}{D_e + k_s R F_p z - k_s R F_p^2 z^2} \quad (4.13)$$

where

$$\Gamma = \frac{C_A}{C_{A(bulk)}}$$

$$\xi = \frac{rA}{F_p V} = \frac{r}{F_p R} \quad (4.14)$$

$$z = \frac{r_c A}{F_p V} = \frac{r_c}{F_p R}$$

where A , V and F_p are the surface area, volume and shape factor respectively.

Time is then introduced using Equation 4.13 and

$$-\rho_B \frac{dr}{dt} = k C_A \quad (4.15)$$

evaluated at $r = r_c$. In non dimensional form this equation becomes,

$$\frac{dz}{dt} = \frac{-k_s D_e C_{Ab}}{F_p R \rho_B} \left(\frac{1}{D_e + k_s R F_p z - k_s R F_p^2 z^2} \right) \quad (4.16)$$

Since conversion is given by,

$$X_B = 1 - \left(\frac{r_c}{R} \right)^3 \quad (4.17)$$

Equation 4.16 becomes

$$\frac{dX_B}{dt} = \frac{k_s C_{Ab} F_p}{R \rho_B} \left(\frac{D_e (1 - X_B)^{2/3}}{D_e + k_s R (1 - X_B)^{1/3} - k_s R (1 - X_B)^{2/3}} \right) \quad (4.18)$$

Equation 4.16 is subject to the initial conditional that at time equals zero, the core size is equal to the particle size. In terms of conversion (Equation 4.18), the initial condition becomes when $t=0$, $X_B=0$.

Equation 4.18 is consistent with equation 4.11 if D_e is assumed constant. Furthermore, if D_e is constant and is much greater than $k_s R(1-X_B)^{1/3} - k_s R(1-X_B)^{2/3}$, Equation 4.18 reduces to Equation 4.2 and becomes kinetically controlled. However if D_e is much smaller than $k_s R(1-X_B)^{1/3} - k_s R(1-X_B)^{2/3}$, Equation 4.18 reduces to Equation 4.10 and becomes ash controlled.

A more comprehensive model is possible if D_e is a known function of conversion. This function can be used in Equation 4.18 and the differential equation can be solved numerically. A variable diffusivity cannot be used in Equation 4.11 since its derivation was based on the assumption that diffusivity was constant.

Results

A particle size effect as shown in Figure 4.1 was observed. As expected, the reaction rate was slower for larger particles. The activation energy was calculated by varying the temperature between 917 °C and 1167 °C over four runs. Each run was performed using 325-400 mesh particles and approximately 15% carbon monoxide. The result of these runs is shown in Figure 4.2.

The activation energy was subsequently calculated by preparing an Arrhenius plot (Figure 4.3) for the same four runs, using data after the induction period. The activation energy for carbon monoxide reduction of ilmenite was found to be 16.1 kcal/mol and the frequency factor, k_o , was found to be 201 cm/min.

The reaction after the induction period was found to be well predicted using a

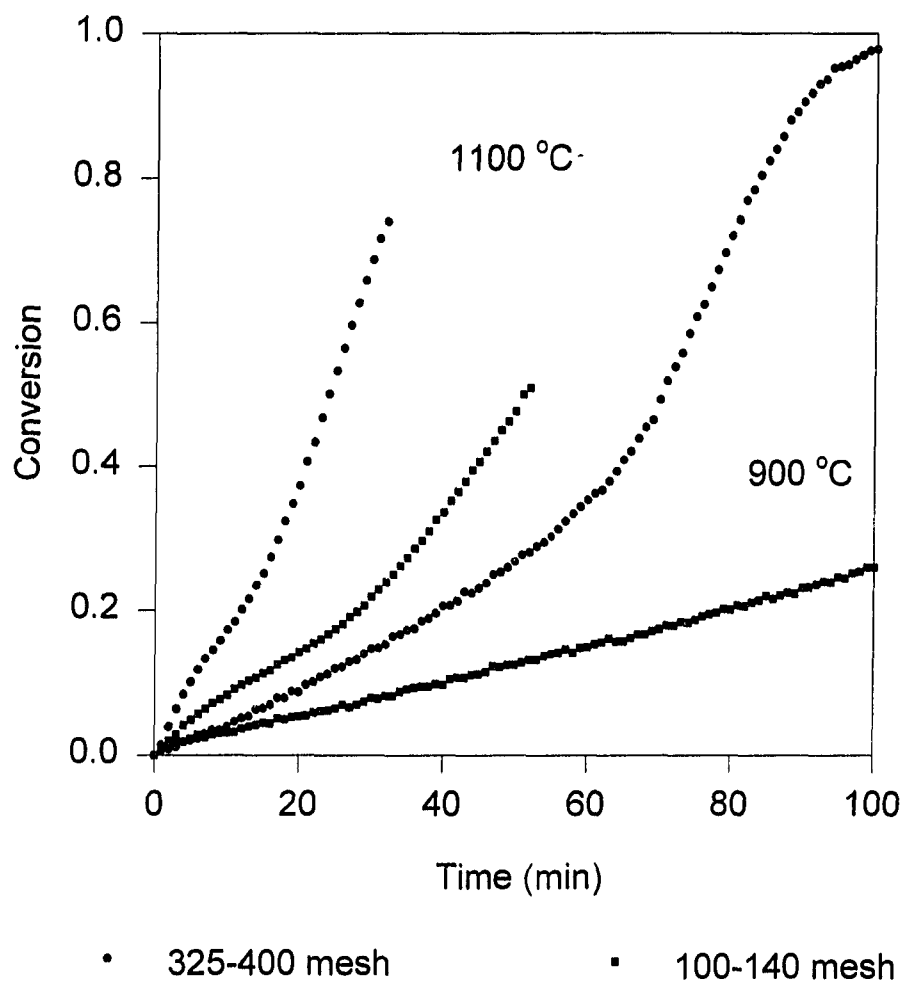


Figure 4.1 Effect of Particle Size on Ilmenite Reduction using Carbon Monoxide

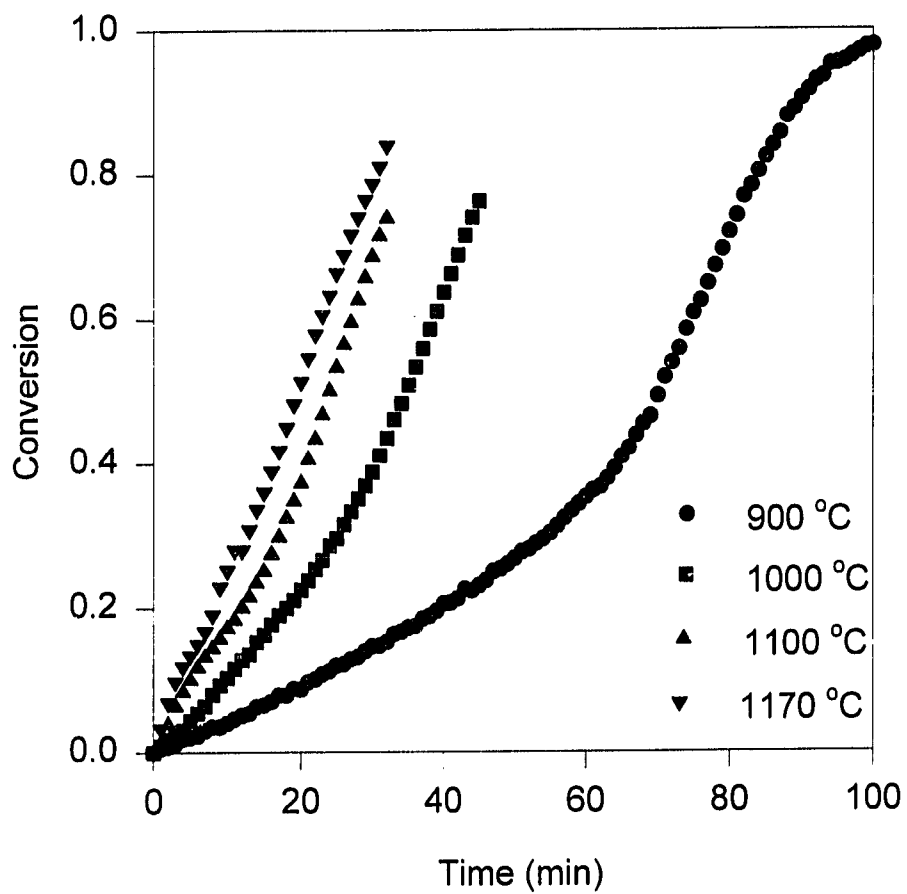


Figure 4.2 Effect of Temperature on 325-400 mesh Ilmenite Particles

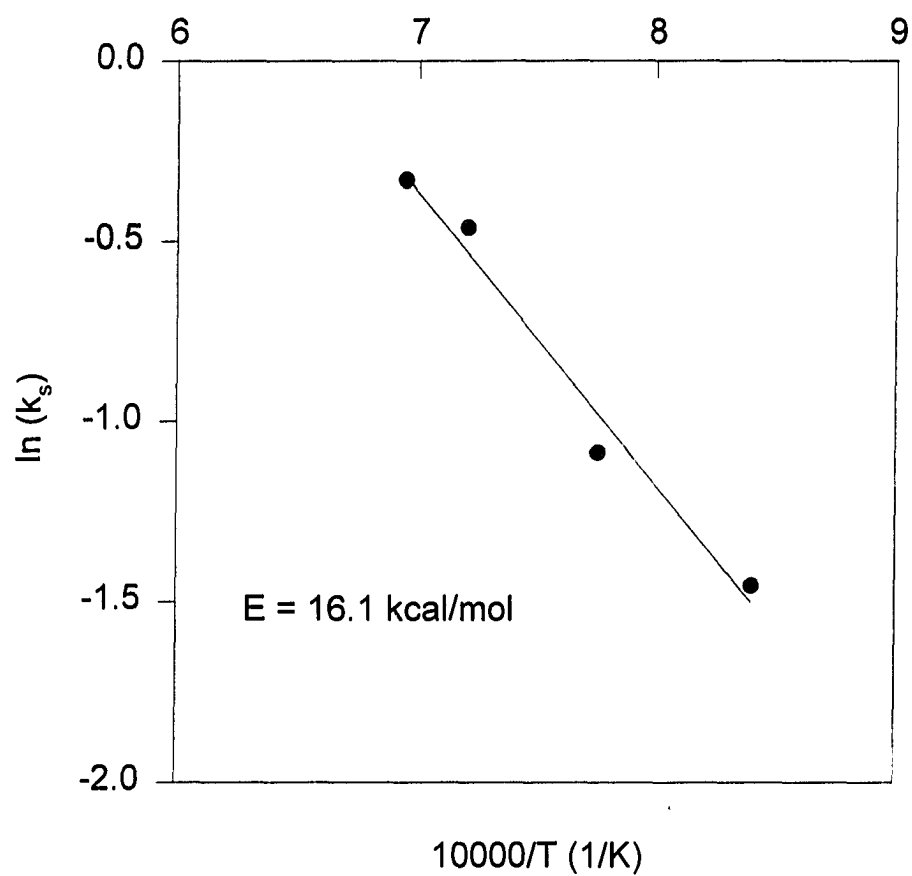


Figure 4.3 Arrhenius Plot for 325-400 mesh Ilmenite Particles using Carbon Monoxide

shrinking core mechanism. The overall reaction was modeled using the combined diffusion and kinetic model allowing for a variable diffusivity. As of yet, a general function relating diffusivity to conversion, for all particle sizes and temperatures, has not been developed.

Discussion

The reduction process can be considered in three distinct phases. Initially, the reduction is characterized by a rather slow induction phase. This is followed by a steep reaction phase where the reaction rate reaches a maximum. Finally, the reaction is quenched and the reaction rate levels off to zero as the ilmenite becomes fully reduced. Characteristic to carbon monoxide reduction is the long induction phase. This phase is longer than any temperature effect and is a distinct attribute of the reaction.

The pure shrinking core model does not adequately explain the induction phase although the reaction and quenching phases are well characterized by the kinetic model. When the model is adjusted to include the reduced effective radius, the model still only accurately predicts the reaction and quenching stages of the experimental results as shown in Figures 4.4. This is due to the fact that the shrinking core model does not contain any terms which can account for an accelerating reaction rate.

The addition of a nucleation model is also not satisfactory. It has been hypothesized by Szekely (1976) and Zhao (1991) that the induction phase is limited due to the growth of iron nuclei. Once enough iron sites have been developed, the iron can

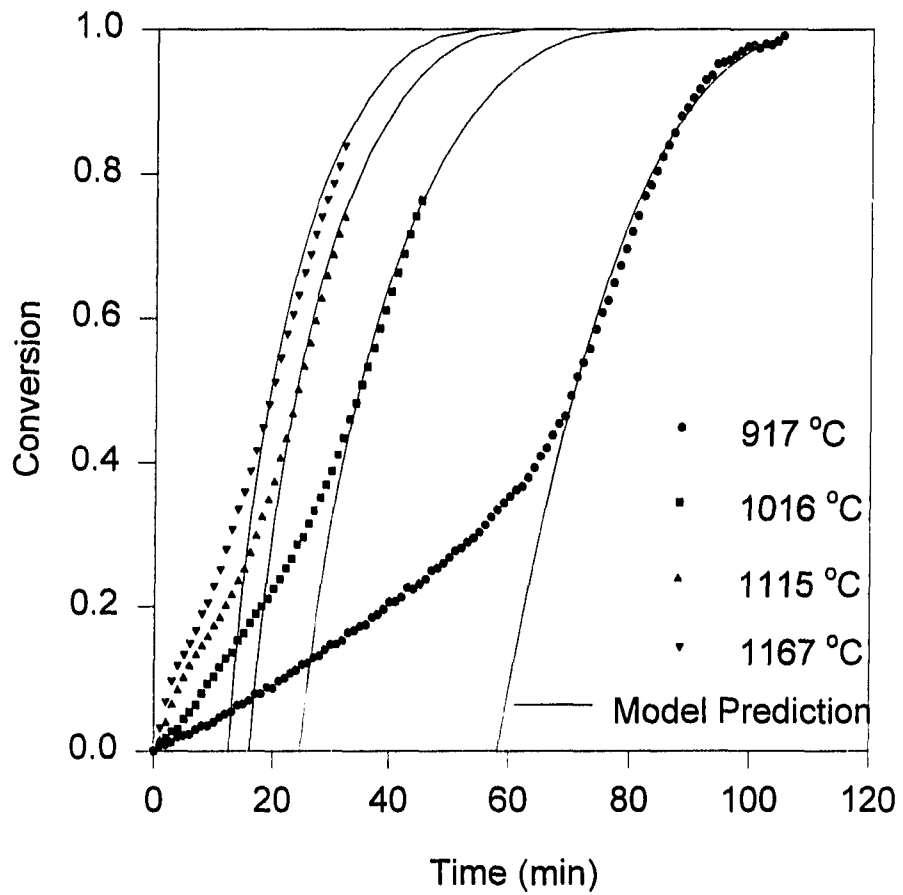


Figure 4.4 Reaction Rate Predicted by Model vs. Experimental Data for 325-400 mesh Ilmenite Particles

diffuse to a relatively close nuclei and the pores can be opened allowing carbon monoxide to access the particle surface.

In order to model this effect, a standard nucleation model for three dimensional growth, assuming all nuclei are present at the reaction start, was used. This model took the form of

$$t = mX^3 \quad (4.19)$$

However, as shown in Figure 4.5, the nucleation model adds the right curvature but grossly under predicts the reaction rate during the induction phase. This means that although nucleation may be present, it is not the rate controlling step during this period.

Additionally, the Avrami model for three dimensional product growth and the Phase Change Model were used since they possess "S" shaped conversion versus time curves. Although both models resembled the data better than models put forth by Szekely (1976), the models are not close enough to provide a reliable fit. Furthermore, the effect of particle size cannot easily be gleaned from the resulting coefficients.

Although it is yet unclear what happens during the induction phase, experiments have shown the following:

1. as particle size increases, the induction phase becomes more prominent
2. as temperature increases the induction phase is reduced
3. as Fe is added, the induction phase is reduced (Zhao, 1991)
4. as the molecular size of the reducing gas is increased, the induction phase

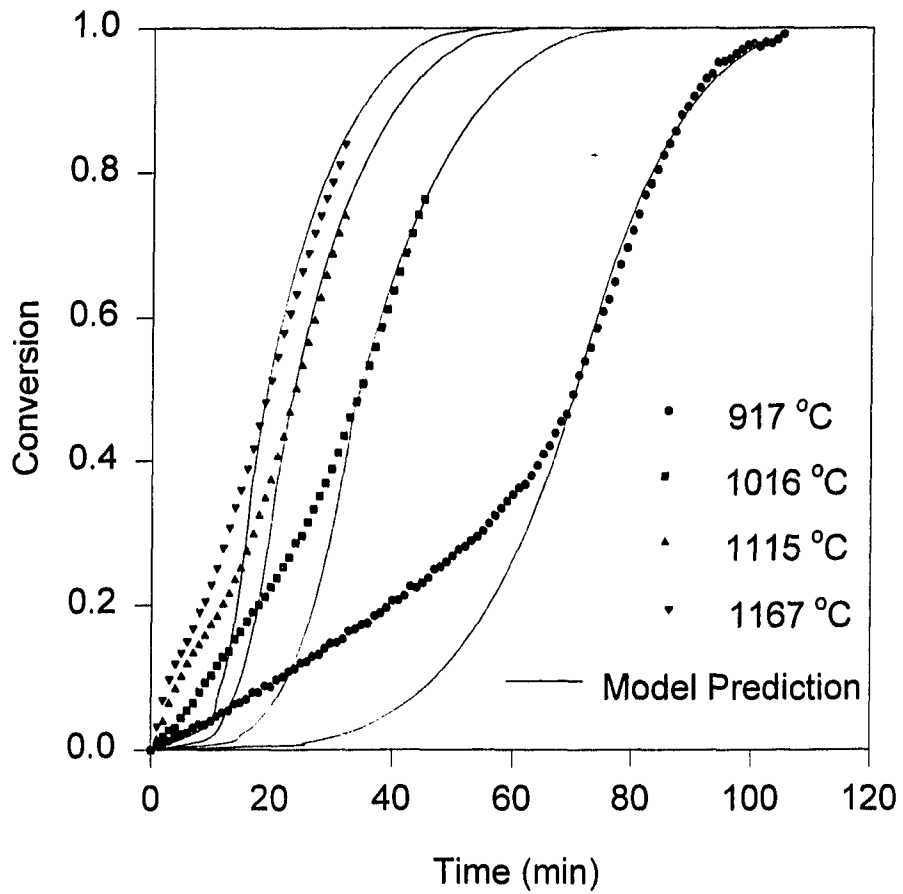


Figure 4.5 Reaction Rate Predicted by Nucleation Model vs. Experimental Data for 325-400 mesh Ilmenite Particles

become longer. Thus the induction phase is more distinct with carbon monoxide reduction than with hydrogen reduction.

These observations tend to indicate that the induction phase is related to the movement of iron but this does not account for the observations between carbon monoxide and hydrogen.

A possible explanation is that diffusivity might somehow be a function of conversion; increasing as conversion increases. The physical meaning of this is that as the reaction progresses, more iron is produced. This iron occupies the micropores in the ilmenite and partially blocks the carbon monoxide from coming in contact with the unreacted core. Thus the local gas concentration is reduced due to a low diffusivity. This dispersed iron can be seen as the bright phases in Figure 4.6.

As more iron is produced, it begins to migrate toward large growth centers since the activity of the highly dispersed iron phase is greater than that of the bulk iron present at the growth locations. These growth centers are scattered throughout the particle as shown in Figure 4.7. This causes the micropores to open and the diffusivity to increase. The process of iron movement continues to affect the reaction until the pore size is no longer the controlling mechanism. At this point, the reaction shifts to being chemically controlled and an increase in the reaction rate is observed.

This theory essentially uses a variable diffusivity to account for the degree of pore blockage and for the fact that the induction stage of carbon monoxide reduction is longer than that of hydrogen. The theory combines the concepts of the nucleation

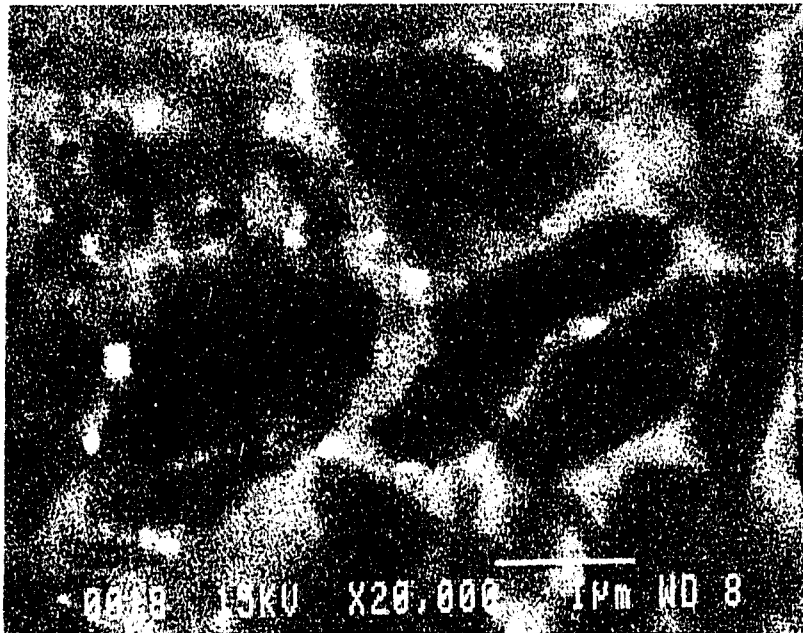


Figure 4.6 Iron Dispersed at Low Conversion

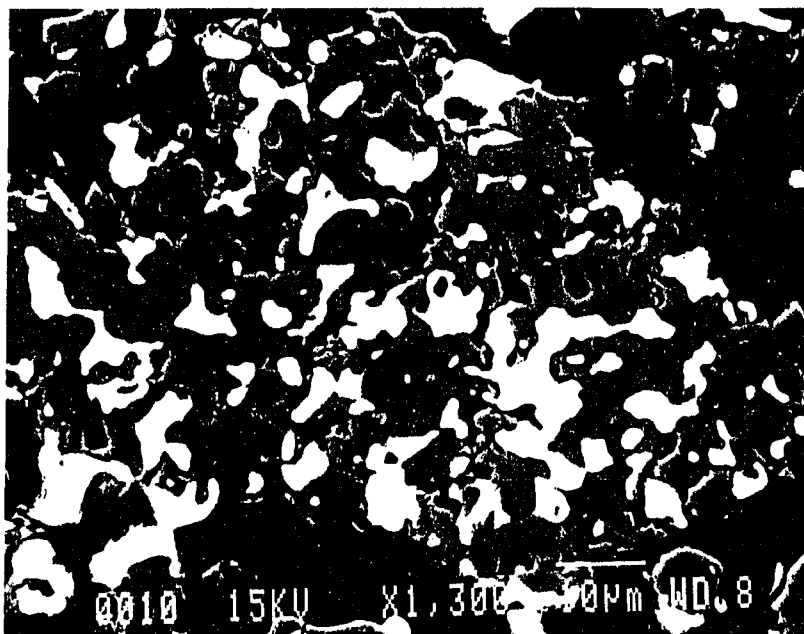


Figure 4.7 Iron Dispersed at High Conversion

hypothesis and the transport reaction mechanism.

Since diffusivity is an unknown function of conversion, the combined model (Equation 4.18) was used to determine the diffusivity needed to accurately predict the experimental results. Since the experimental results were used to predict the variable diffusivity, the model and experimental values fit exactly, as shown in Figures 4.8 and 4.9. The equation used to solve for diffusivity is as follows,

$$D_e = \frac{\frac{\rho_B R^2}{3k_s C_A} \frac{dX_B}{dt} [(1-X_B)^{-1/3} - 1]}{1 - \frac{\rho_B R}{3k_s C_A} (1-X_B)^{-2/3} \frac{dX_B}{dt}} \quad (4.20)$$

The model relies on a conversion versus time slope. This slope was provided directly from smoothed reaction data. The diffusivity coefficient was then plotted versus conversion and Figure 4.10 was obtained.

Using Figure 4.10, more can be said regarding the functionality of diffusivity. Diffusivity is a complex function of iron movement, structural changes, and other factors. Furthermore, it seems to vary with respect to temperature (Figure 4.11) and particle size (Figure 4.12). As temperature increases, the iron phase is more mobile so the pores open more quickly. As particle size increases and the ash layer becomes more prominent, the pores seem to take longer to open.

Additionally, small particles show the relative effect between temperature and structural effects. Initially, different temperature runs show significantly different diffusivities. However, as conversion increases, the diffusivity curves tend to converge indicating that structural changes, which are less temperature sensitive, become more

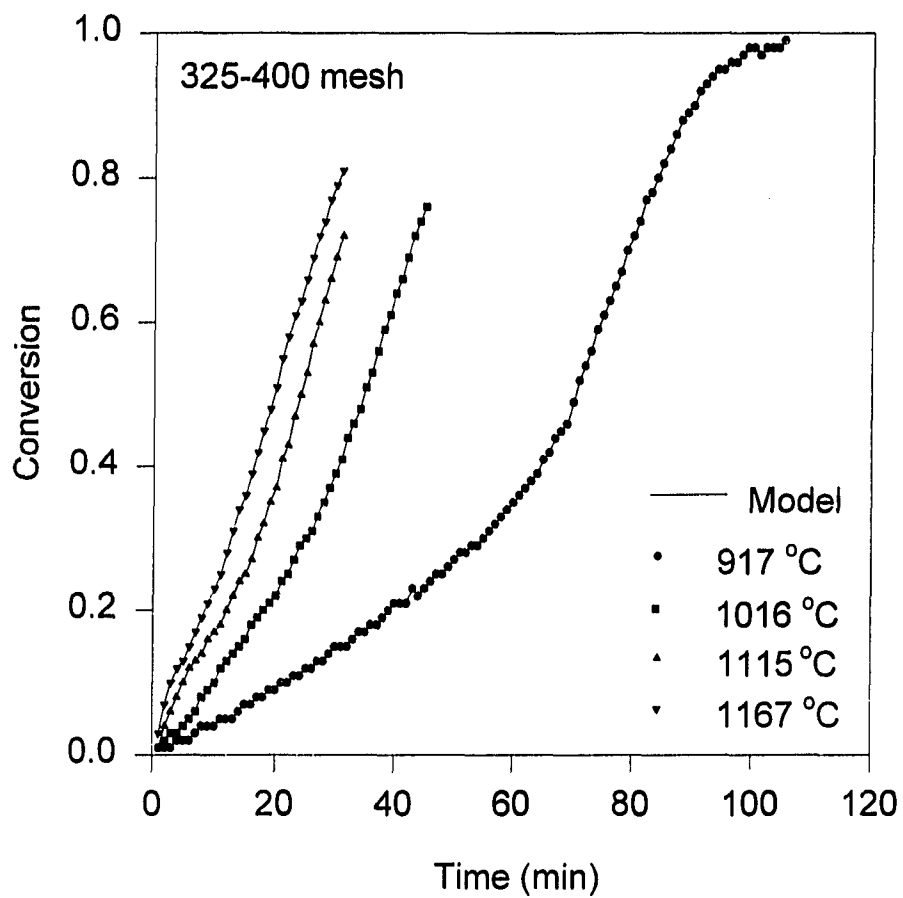


Figure 4.8 Reaction Data Predicted using a Variable Diffusivity

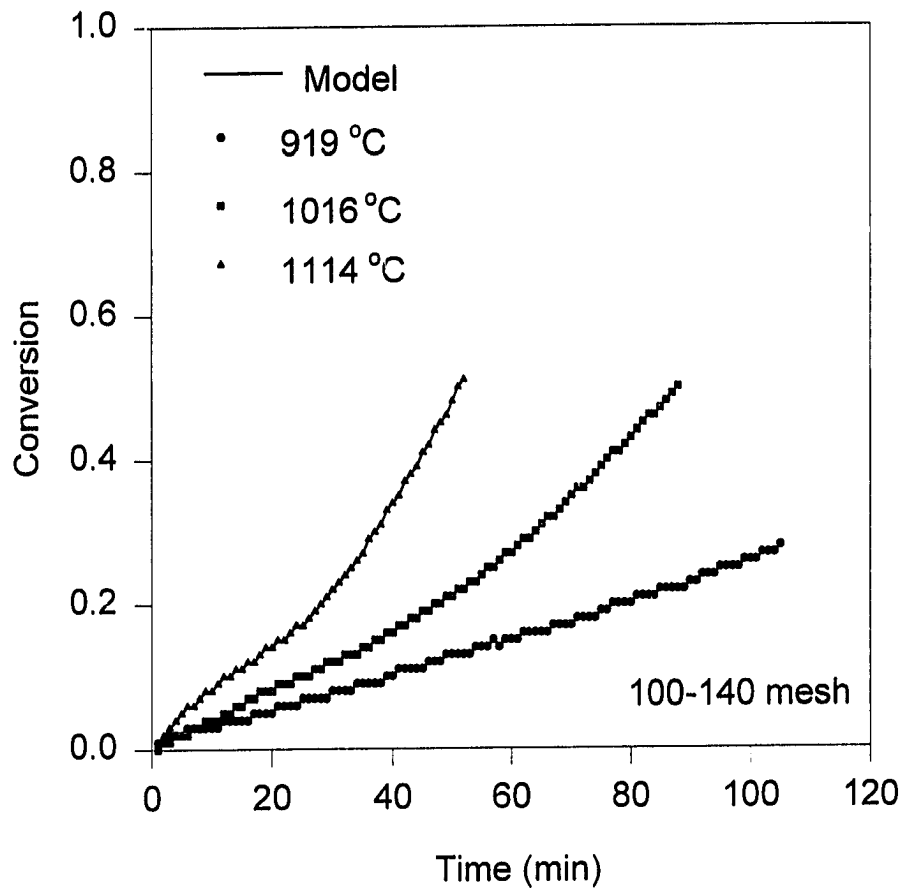


Figure 4.9 Reaction Data Predicted using a Variable Diffusivity

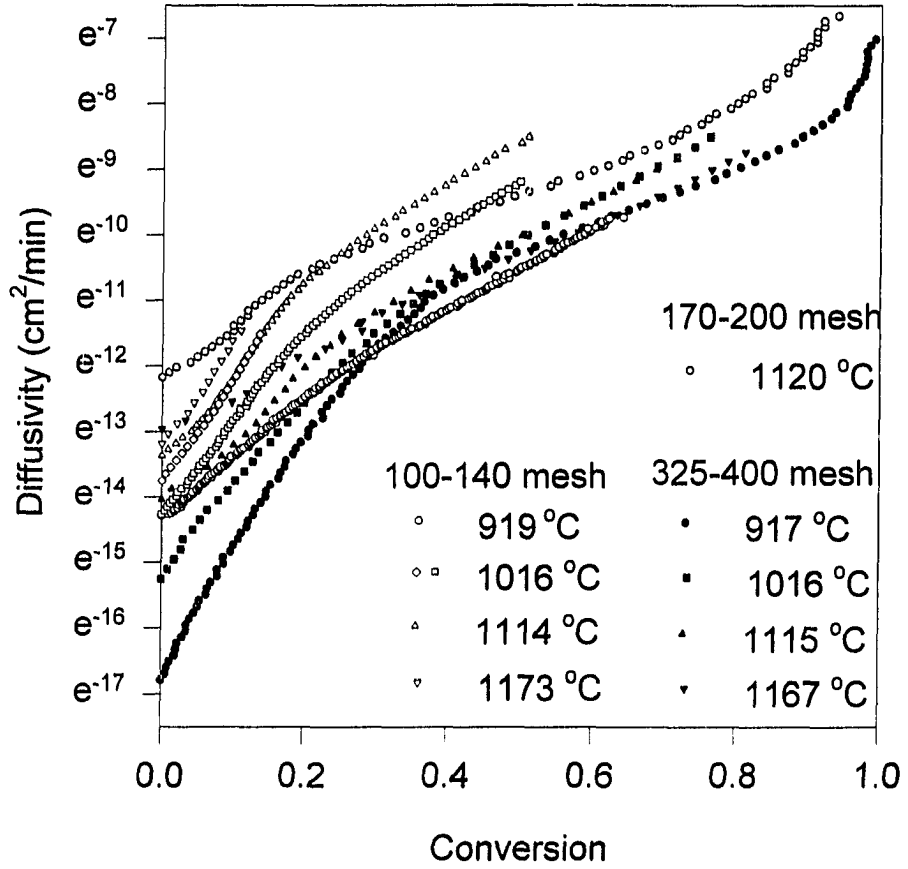


Figure 4.10 Diffusivity vs. Conversion

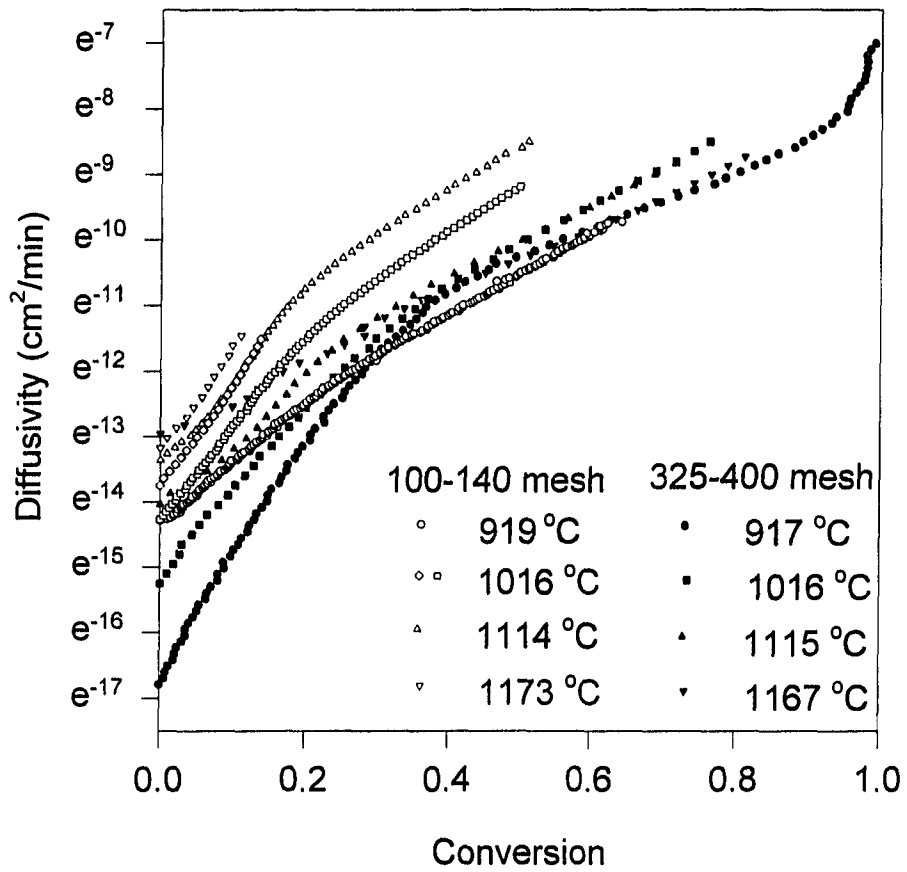


Figure 4.11 Diffusivity vs. Conversion
Effect of Temperature

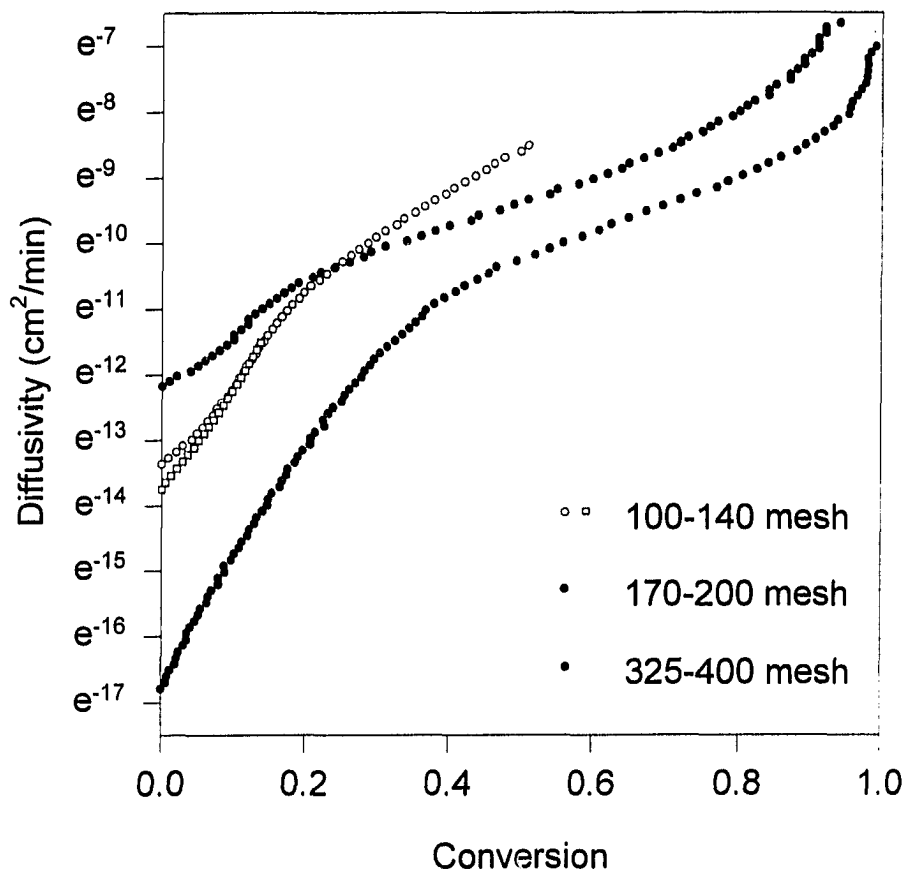


Figure 4.12 Diffusivity vs. Conversion
Effect of Particle Size

prominent. Larger particles, which are dependent entirely on the mobility of iron, are not severely influenced by structural changes and do not converge.

Thus, the model will provide quantitative data when an accurate function, describing diffusivity as a function of conversion, is determined. As a preliminary evaluation of trends, the variation in diffusivity with conversion was approximated by an exponential function (Figure 4.13). The model predictions using this exponential dependence are shown in Figure 4.14. Since this exponential function is only an approximation, the model fit to the data is only to confirm the trends and does not have adequate quantitative accuracy.

The current model is also only conversion dependent and assumes an average diffusivity. It is very likely that diffusivity is a function of radius as well; decreasing near the unreacted core and increasing away from the core. Thus, further work is needed to determine the dependence of diffusivity on conversion more accurately using fundamental structural models. Nonetheless, until a better function of diffusivity is found, the model qualitatively fits the reaction data well.

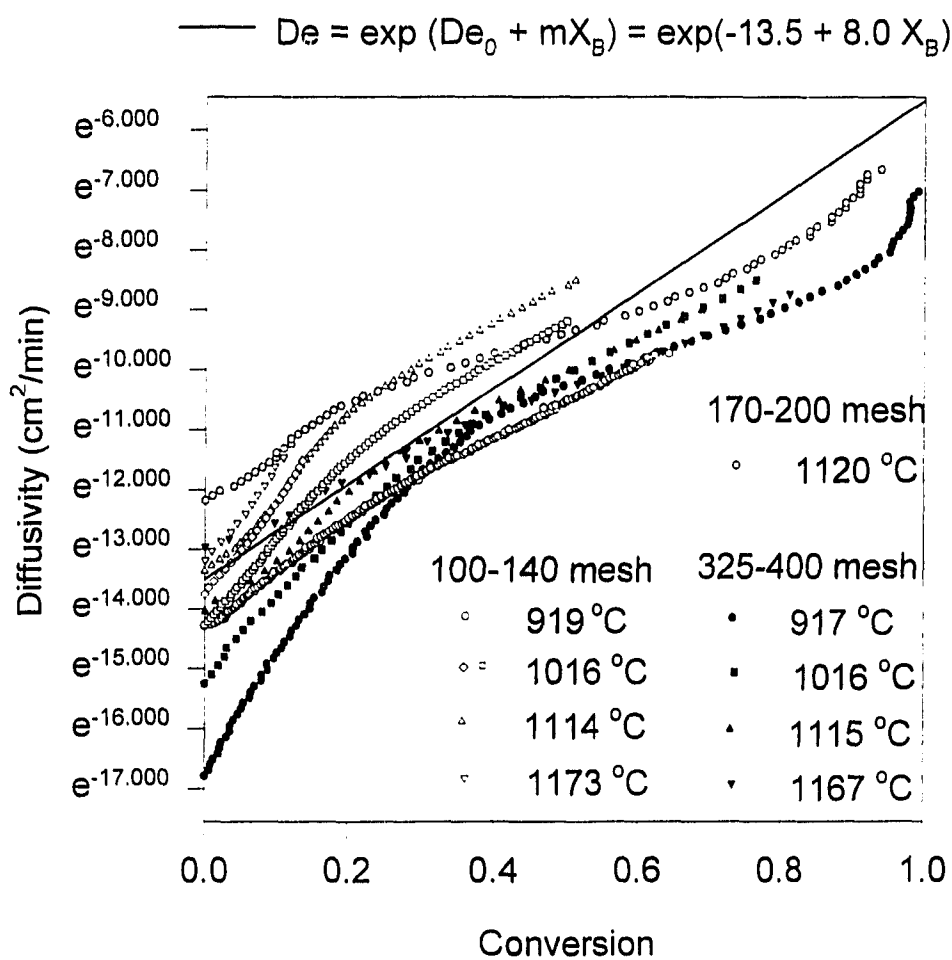


Figure 4.13 Diffusivity vs. Conversion

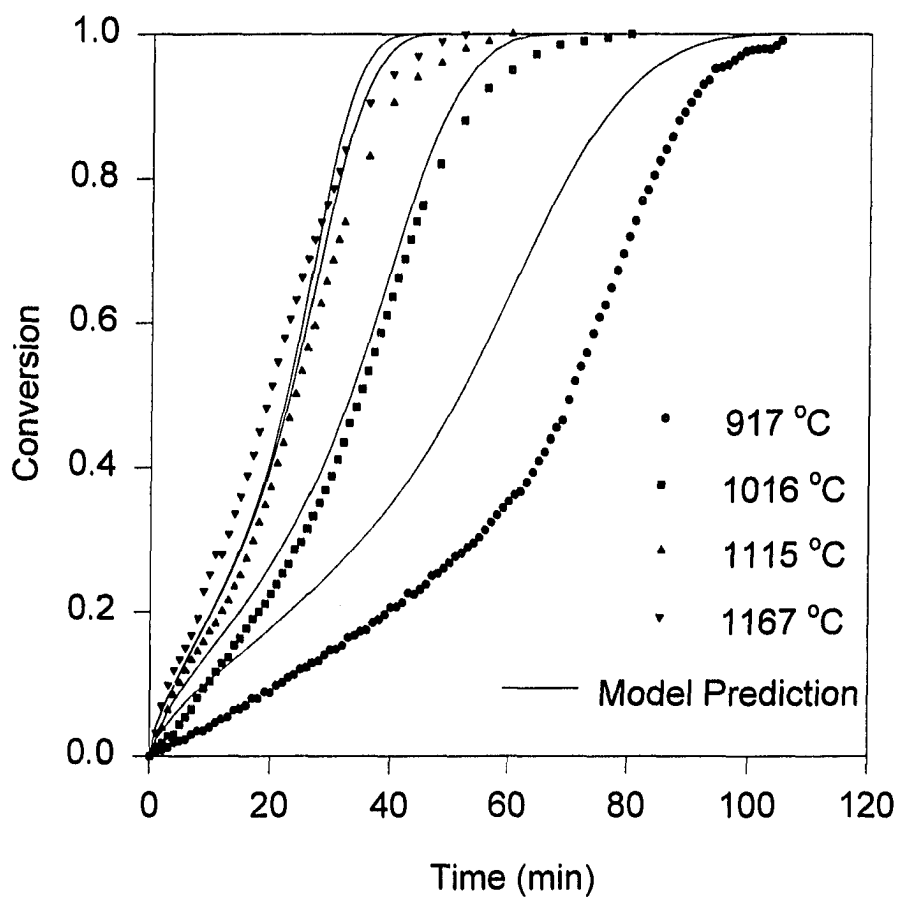


Figure 4.14 Reaction Rate Predicted by Variable Diffusivity Model vs. Experimental Data for 325-400 mesh Ilmenite Particles

REDUCTION OF LUNAR SOIL WITH HYDROGEN

Lunar Soil

Over time, the lunar bedrock has been bombarded by meteoroids and solar winds. As a result, the surface bedrock has fragmented and now the lunar surface is almost completely covered with a layer of *lunar regolith* or lunar soil. This layer, which is generally 4 to 5 meters thick, consists of a variety of particles, generally less than 1 cm in size (Heiken et al., 1991).

The particles that make up the regolith are a combination of fractured bedrock and remelted debris of older rocks referred to as *impact melt rocks*. Depending on the extent and types of local activity, the mineral composition of lunar regolith can vary substantially.

Differences in lunar composition are also found between the lunar highlands and maria. The highlands tend to be rich in minerals containing lighter or lower melting point elements like calcium and alumina. The maria however tends to contain heavier elements such as iron and titanium.

In general however, lunar rocks can be said to be made up of minerals and glasses. As noted in the Lunar Sourcebook (Heiken et al., 1991), silicate minerals, which are composed primarily of silicon and oxygen, make up over 90% of the volume of most lunar rocks. Silicates are followed by metal oxides in terms of abundance. Depending on the location, metal oxides, especially ilmenite, can make up as much as 20% by volume of lunar rocks. This type of metal oxide concentration is primarily

found in lunar maria.

Lunar silicates consist primarily of *pyroxene*, $(\text{Ca,Fe,Mg})_2\text{Si}_2\text{O}_6$; *plagioclase feldspar*, $(\text{Ca,Na})(\text{Al,Si})_4\text{O}_8$; and *olivine*, $(\text{Mg,Fe})_2\text{SiO}_4$. The parenthetical notation denotes that the compounds are solid solutions and that the metals contained within parenthesis can substitute for one another. Based on this variability, compositions of lunar silicates are commonly viewed pictorially. Figure 5.1 shows the composition of pyroxenes and Figure 5.2 shows the more common nomenclature associated with pyroxenes. As Massieon showed, the different elements present can greatly affect the reduction rates of these minerals.

Compared to terrestrial minerals, lunar silicates are unique in that they contain no oxidized iron. This is due to the fact that there is less oxygen on the moon than there is on earth. Iron in lunar pyroxenes and ilmenite, for instance, occurs only as Fe^{2+} . Furthermore, terrestrial pyroxenes tend to contain lighter elements like magnesium and calcium while lunar pyroxenes tend to contain iron. Similarly, terrestrial olivine tends to be richer in magnesium than its lunar counterpart.

Specific Lunar Sample

NASA provided the University of Arizona with 4.9 grams of lunar soil collected from the Apollo 11 mission (Sample # 10084.100). The sample is unique for many reasons. First, the sample was a contingency sample. On the first four Apollo missions, the first astronaut to reach the lunar surface sampled the lunar regolith with a

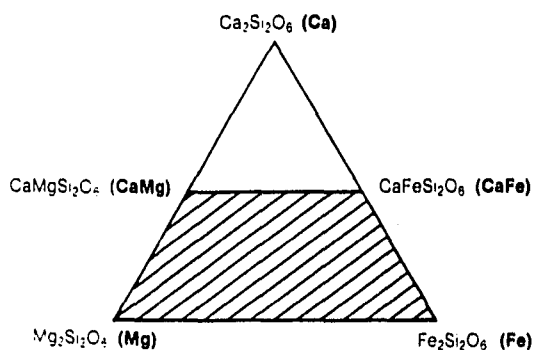


Figure 5.1 Compositions of Pyroxenes (after Heiken et al., 1991)

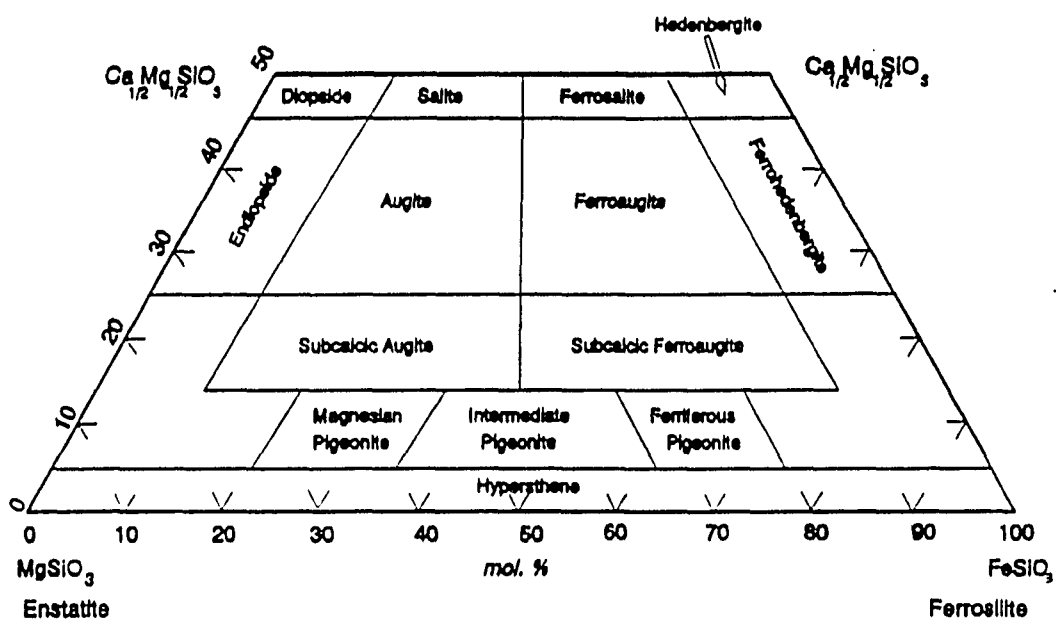


Figure 5.1b Nomenclature of Pyroxenes (after Deer et al., 1982)

contingency sampler. This way, in the event the mission was unexpectedly aborted, at least some lunar material would have been collected. Second, Apollo 11 was the first manned mission to land on the moon. Thus, the sample received was one of the first collected by man from the moon.

The Apollo 11 landing site was on the flat surface of Mare Tranquillitatis. A picture of the landing site has been included as Figure 5.3. Since, the lunar sample was a contingency sample, the picture essentially shows the precise area from which the sample was collected.

According to the Lunar Sourcebook and other published data, the Apollo 11 samples contained 44.9% pyroxenes, 21.4% plagioclase, 16% mare glass, 8.3% highland glass, 6.5% ilmenite and 2.1% olivine. The specific lunar sample received contained approximately 11% iron by weight. An SEM x-ray map (Figure 5.4) shows the relative abundance of iron, silica, aluminum, and calcium. Figure 5.5 shows the relative location of the lunar sample on the pyroxene quadrilateral. After beneficiation, the ilmenite content was increased to approximately 30% by weight (Cutler, personal communication, 1993).

The lunar sample was provided for various characterization experiments, however, a portion of the sample was devoted to reduction studies. These samples were reduced using hydrogen in an attempt to understand the basic reaction mechanisms and to test the results versus data collected from previous experiments using lunar simulants.



Figure 5.3 View of the Apollo 11 Landing Site
(NASA Photo AS11-37-5468)

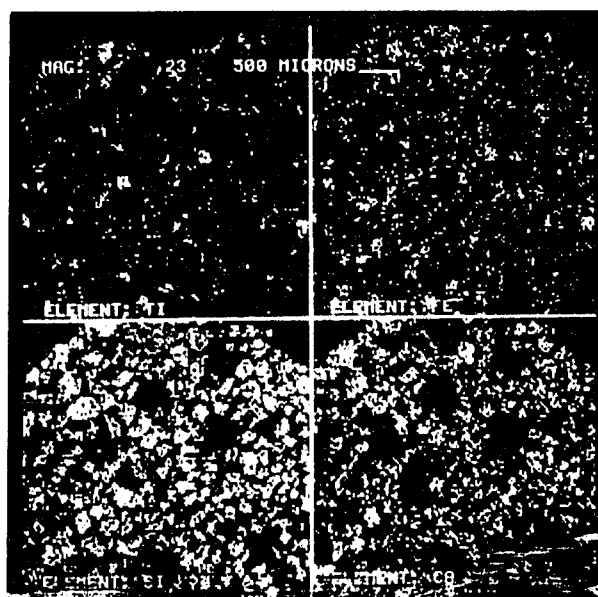


Figure 5.4 X-Ray Map of Ti, Fe, Si and Ca in Entire Lunar Sample
(Courtesy of Dr. Andrew Cutler)

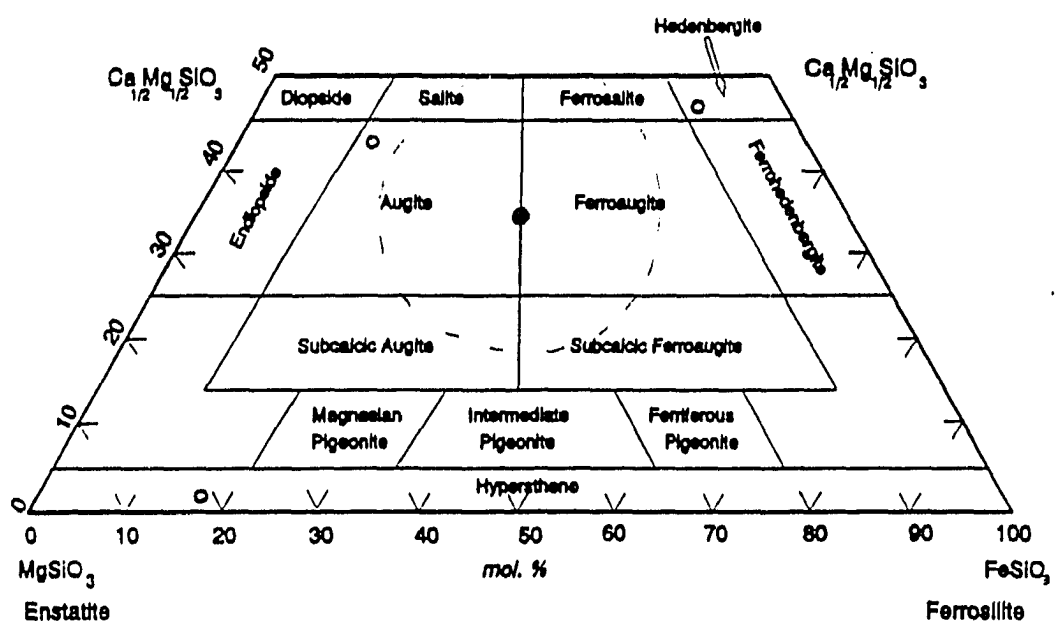


Figure 5.5 Relative Location of Lunar Sample on Pyroxene Quadrilateral

The sample was separated using a heavy liquids technique and both the ilmenite and pyroxene were concentrated (Cutler, personal communication, 1994). The samples were then sieved using standard size sieves and approximately 150 mg of the pyroxene sample, from the +19 and 19-20 mesh size (75-90+ μm), was reduced in a thermogravimetric reactor.

Experimental Apparatus

The reduction experiments were conducted in an apparatus similar to that shown in Figure 2.1. At that time however, it was yet unclear which orientation of particles resulted in the least diffusional effects. As a result, the shallow pan method was used to reduce the risk of dropping or losing part of the sample.

The sample was in two parts in order to conduct two runs. The first run, using 93.18 mg of +19 mesh sample, was labeled N-1 and was run nearly to completion. The second run, using 46.66 mg of 19-20 mesh sample, was labeled N-2 and was partially reduced.

Initially both samples were kept under a nitrogen purge for more than four hours. The furnace was then partially raised around the sample until a temperature of 250 °C was reached. This was done as a precautionary measure to insure the samples were dry. The experiments were both run at 1109 °C using 25.6% hydrogen. The flow rate of the combined hydrogen and nitrogen gas streams was 411 cc/min and 414 cc/min respectively.

The first reaction was run for 16 hours to insure relatively complete conversion. The second reaction was run for only 2.25 minutes in order to study the order of reactions. The data from both experiments has been included in Appendix A.

Results

The first sample, N-1, which was left in the reactor until relatively complete conversion was achieved, lost 1.29% of its weight (1.21 mg) within the first 15 minutes of the reaction. Over the course of 16 hours, the sample lost another 2.06% of its weight, or 1.92 mg. In terms of conversion, the N-1 sample was thought to have achieved approximately than 25% conversion. However, since the exact composition of the sample is unknown, it is difficult to say exactly what level of conversion was obtained.

The partially reduced sample, N-2, lost .38 mg or .81% of its total weight. Since the majority of the weight loss occurred with the first few minutes of the reaction, it is believed that this sample achieved approximately 6% conversion.

Interestingly enough, the N-1 sample which was believed to be completely reduced, still showed signs of gradual weight loss at 1100 °C.

Discussion

The field of pyroxene reduction is relatively untouched. Little or no work has been done and thus little data is available for comparison. The most similar research has been done by Massieon in 1992. Massieon reduced three types of pyroxenes

(hypersthene, augite and hedenbergite) at temperatures from 1090 K to 1390 K using 14% hydrogen. He noted that mass changes were "...small and took place over long periods of time." Furthermore, he noted that the majority of the weight loss "... took place within the first few minutes of the experiment, when the reactor system had not yet stabilized..." and that "...after the initial mass loss, the rate of reduction was slow and close to constant."¹ These observations seem to accurately describe the reduction data acquired from the reduction of the N-1 sample.

The lunar sample, as shown in Figure 5.5, lies within the center of the pyroxene quadrilateral. Massieon's three lunar simulants surround the lunar sample. A comparison of conversion versus time data, shown in Figure 5.6, shows that the lunar sample fell within the range of lunar simulant reduction. Thus lunar simulants are an adequate method from which to study lunar kinetic data.

The SEM micrographs of lunar simulants and actual lunar soil are also similar. Figure 5.7 shows Figure 2.8 from Massieon's 1992 thesis. The cross section of a completely reduced Fayalite sample closely resembles the SEM pictures taken from the completely reduced N-1 sample (Figure 5.8). Furthermore, Figure 5.9 (Figure 3.3 from Massieon's work) shows a partially reduced hypersthene that closely resembles Figure 5.10 taken from the partially reduced lunar sample, N-2.

Unfortunately, even though the lunar soil seems to react predictably, many of the observations that can be made by studying SEM pictures cannot yet be explained.

¹ Massieon, 1992, pg. 56.

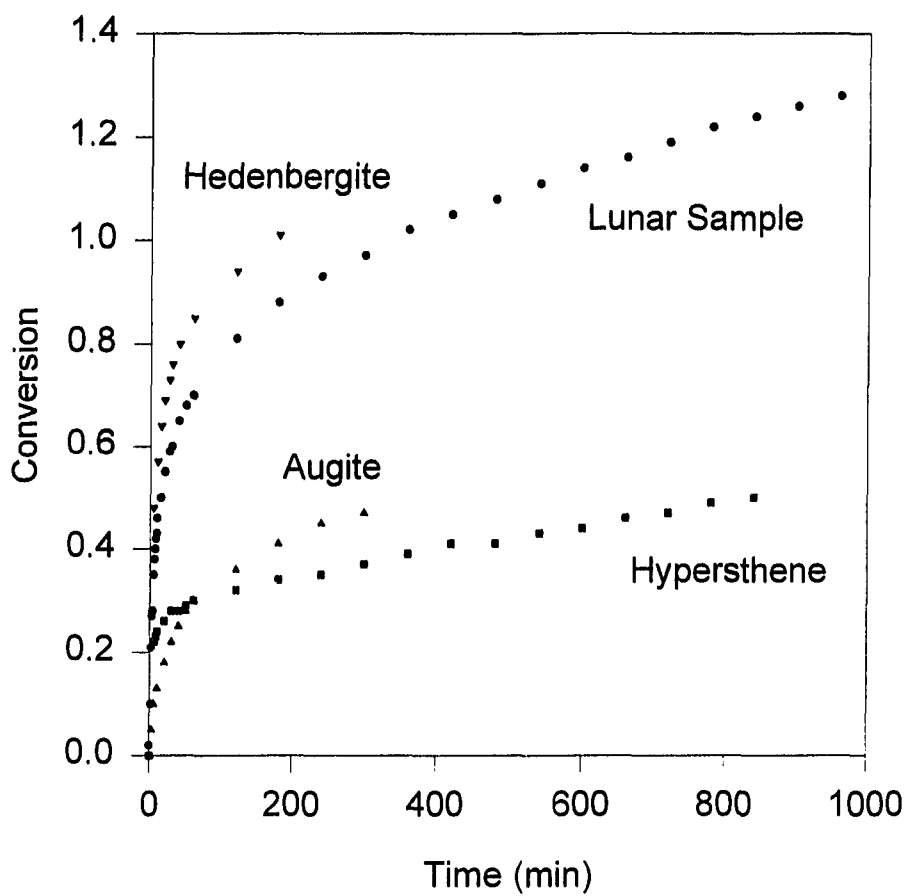


Figure 5.6 Relative Rate of Lunar Sample compared to Known Simulants

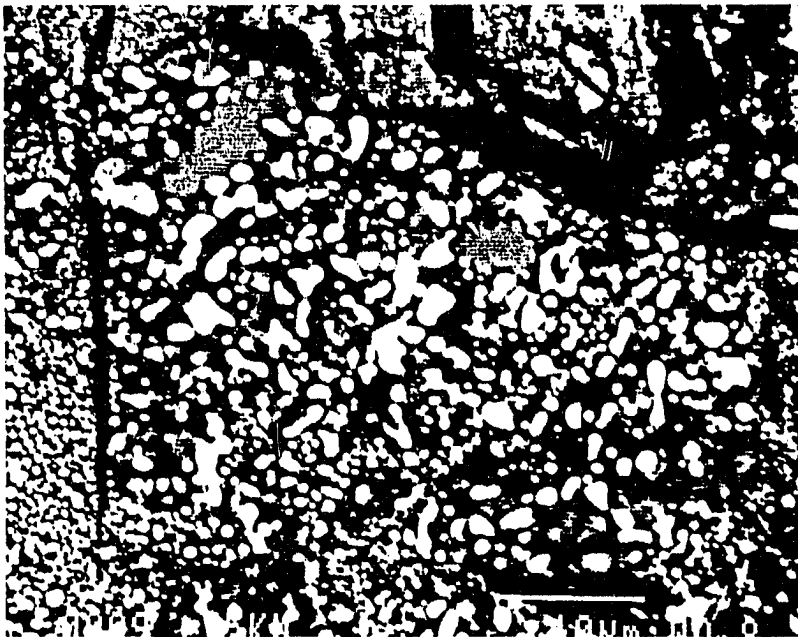


Figure 5.7 SEM Micrograph of Completely Reduced Fayalite
(Courtesy of Charles Massieon)

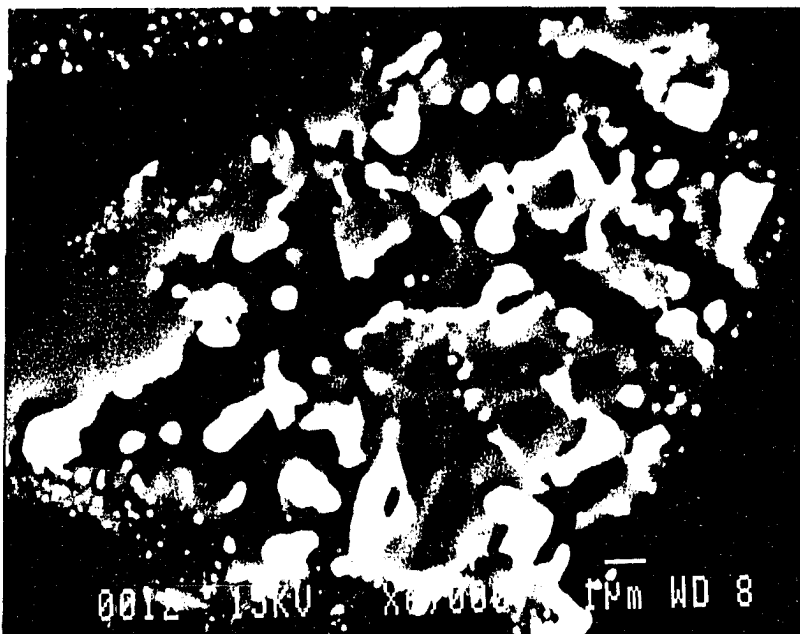


Figure 5.8 SEM Micrograph of Completely Reduced Lunar Sample, Particle #3

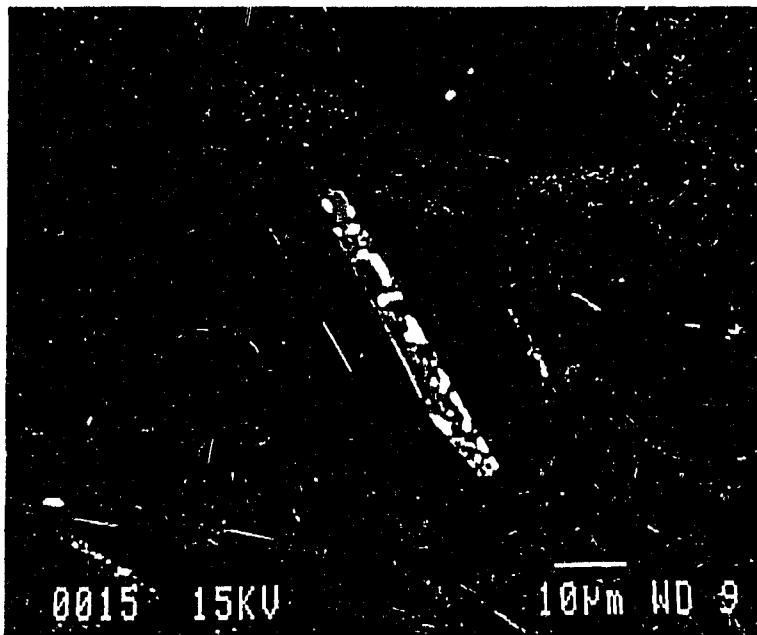


Figure 5.9 SEM Micrograph of Partially Reduced Hypersthene
(Courtesy of Charles Massieon)

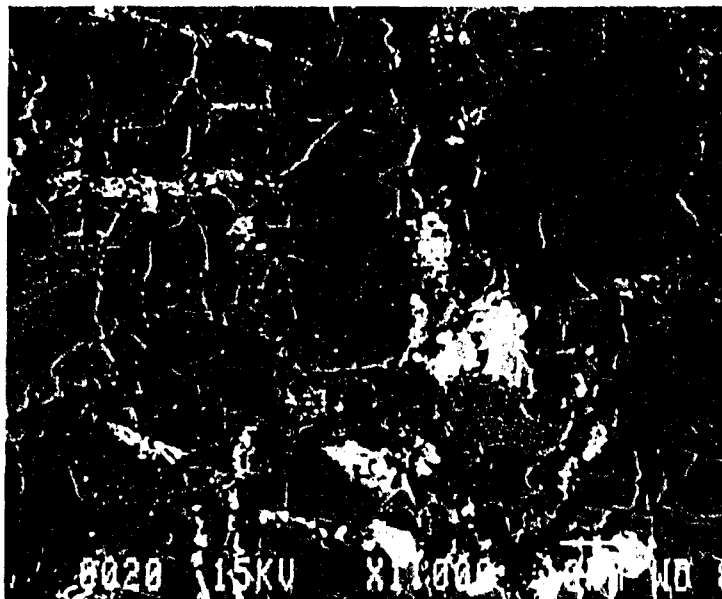


Figure 5.10 SEM Micrograph of Partially Reduced Lunar Sample, Particle #18

For instance, Figures 5.11, 5.12a and 5.12b show a particle from sample N-1 and its accompanying x-ray maps. Most notable are the distinct phases that are seen. Iron is clearly identified as the bright spot near the bottom of the Figure 5.11 and is also seen as medium and small globs. The light gray phase directly below the iron can be identified as pyroxene due to its high content of calcium and magnesium and lack of aluminum. The x-ray maps however show very little iron in that region. Two different conclusions can be drawn from this observation. First, that the pyroxene contained no iron and is of the form $(Ca,Mg)SiO_4$. If this conclusion is accepted the question becomes where did the iron come from? The second conclusion is that this was pyroxene in the form $(Ca,Fe,Mg)SiO_4$ and that it has been completely reduced. This is the more likely case, however now the migration of iron to basically one site must be explained.

There is also evidence that some iron does not accumulate as appreciably. Figure 5.13 shows a region composed primarily of silica and magnesium that has been reduced. The iron has accumulated to many small sites over the sample instead of one large region. Spot x-ray analyses (included as Figure 5.15) also show that the semi-bright shards are magnesium and reveal the relatively low concentration of calcium. The x-ray map (Figure 5.14) shows that titanium is distributed throughout the sample. This is in direct contrast to Figure 5.11 where the titanium is concentrated and the magnesium has not separated. It is possible that the presence of calcium or lack of titanium affects the degree of iron and magnesium separation.

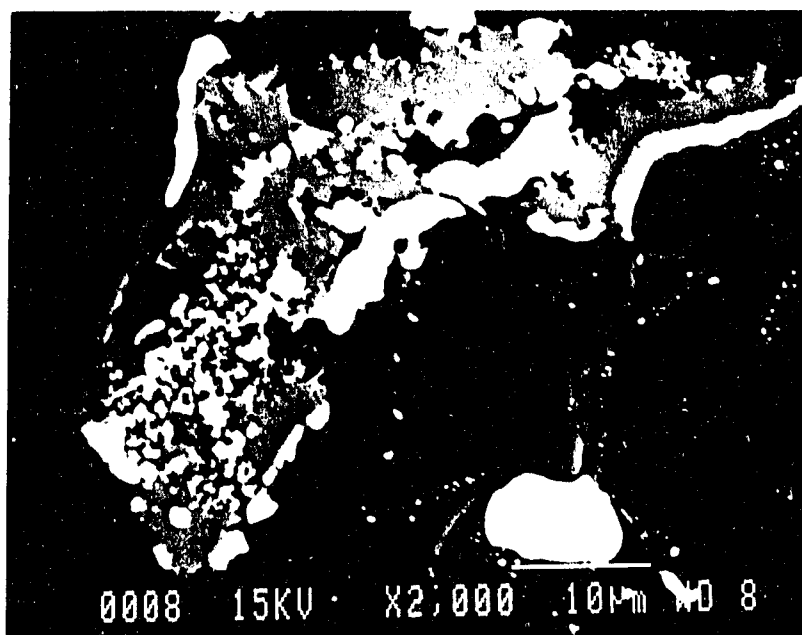


Figure 5.11 SEM Micrograph of Completely Reduced Lunar Sample, Particle #5

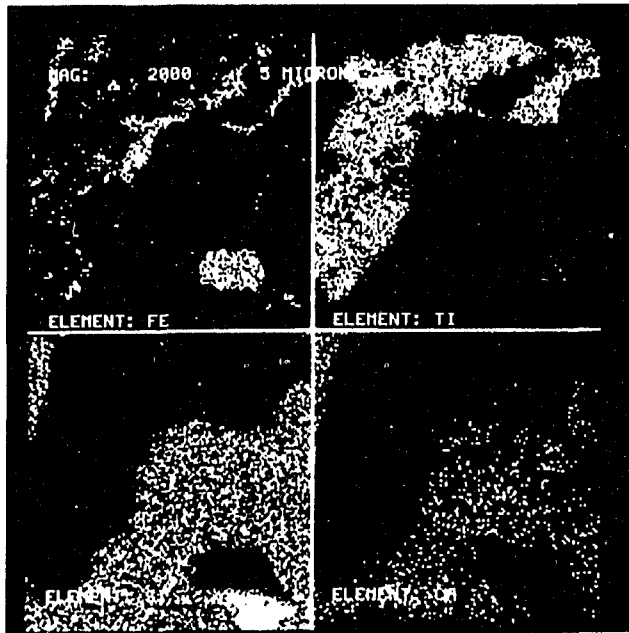


Figure 5.12a X-Ray Map Detailing Fe, Ti, Si and Ca for Particle #5

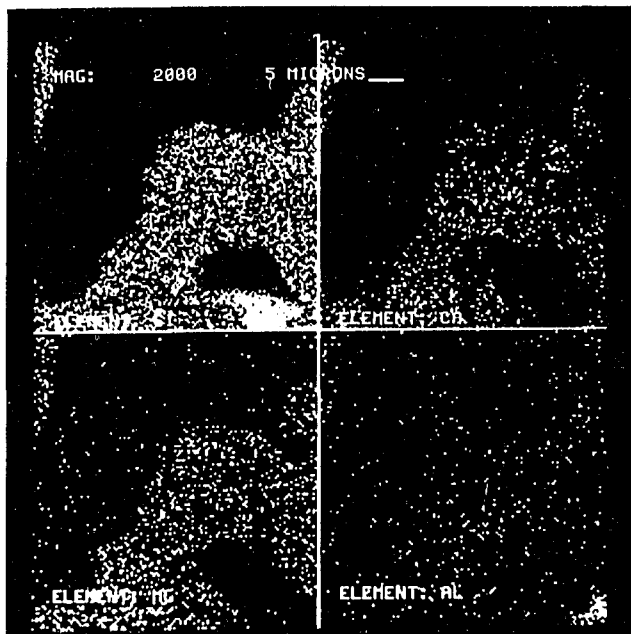


Figure 5.12b X-Ray Map Detailing Si, Ca, Mg and Al for Particle #5

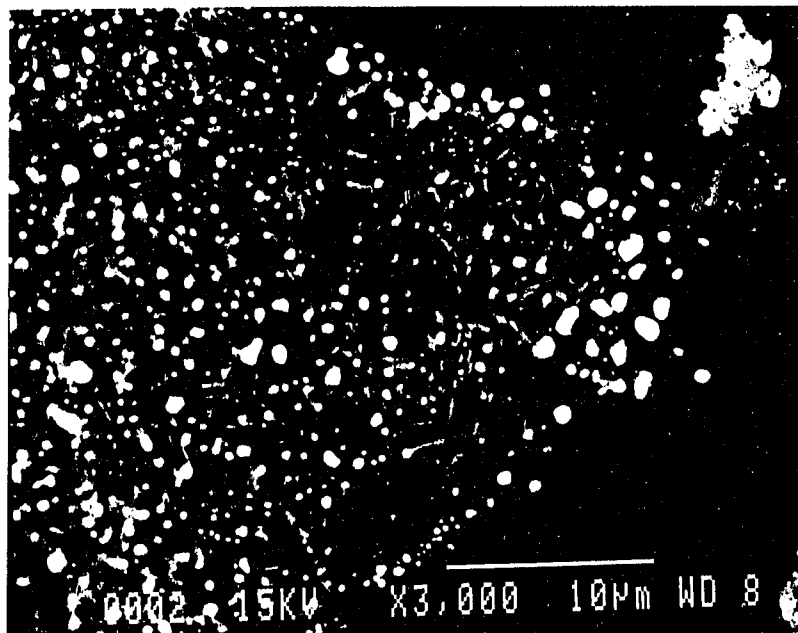


Figure 5.13 SEM Micrograph of Completely Reduced Lunar Sample, Particle # 1

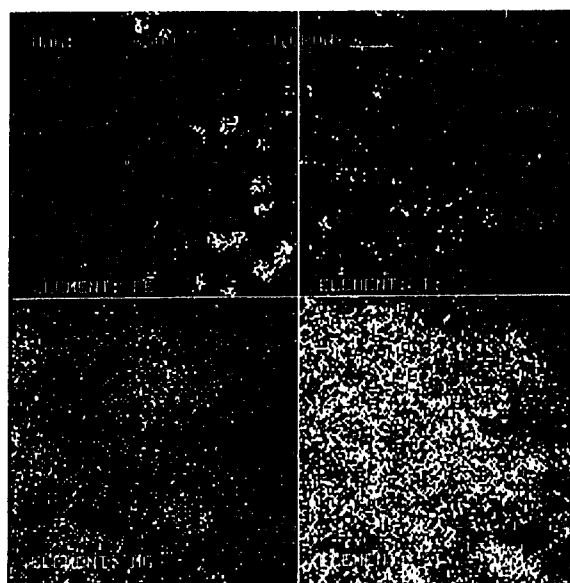
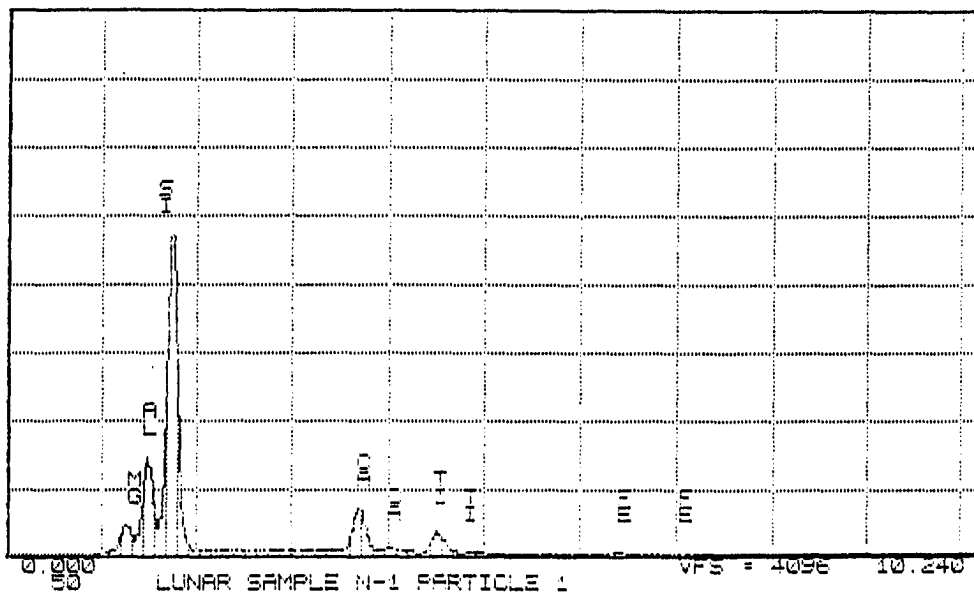


Figure 5.14 X-Ray Map Detailing Fe, Ti, Mg and Si for Particle #1

Series II University of Arizona
 Cursor: 0.010KeV = 0

FRI 13-MAY-94 12:47



Series II University of Arizona
 Cursor: 0.010KeV = 0

FRI 13-MAY-94 12:50

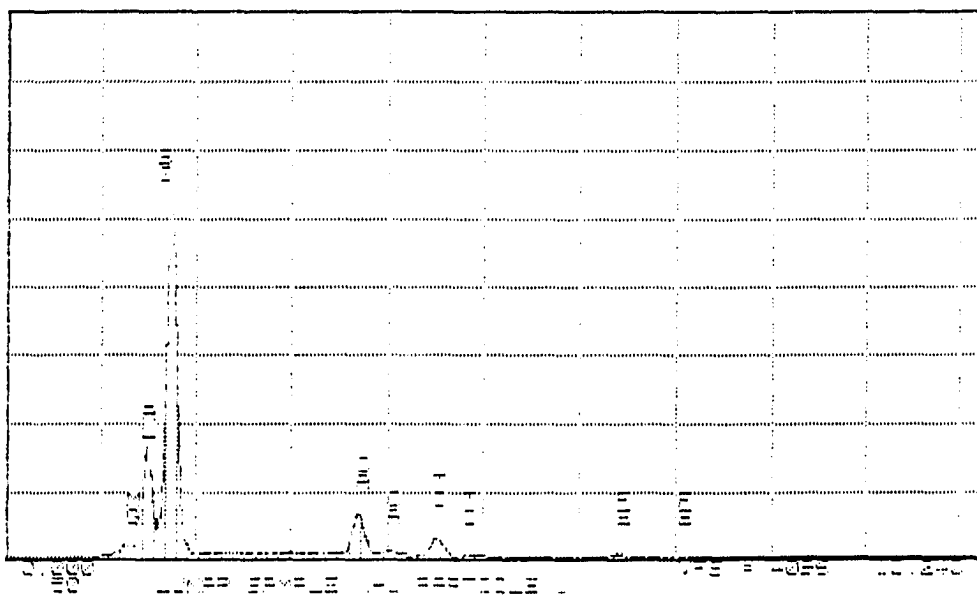


Figure 5.15 Spot X-Ray Analysis for Particle #1

Another interesting sample is shown in Figure 5.16 with x-ray maps included as Figure 5.17a and b. The bright phase located in the upper left half of the figure is a combination of iron and titanium. This sample was the largest concentration of ilmenite within the pyroxene separation. The x-ray map shows that the iron has not accumulated into very large globs but rather has accumulated as many smaller globs.

The lower half of Figure 5.16 contains silica, alumina, and calcium. This is indicative of feldspar. However, feldspar is thought to contain no iron and the sample is riddled with small pockets of iron. It is possible that the feldspar is actually a mixture of feldspar and pyroxene that has reduced. It is also possible that some iron migrated to less iron rich areas.

The partially reduced sample, N-2, also shows interesting phenomena. In Figure 5.18, it can be seen that iron has been produced almost immediately and that the reaction has progressed substantially. At lower magnification, another figure (Figure 5.19) also shows that iron rich areas are the first to react. This figure shows that the sample was probably not mass transfer controlled, since areas within particles have clearly reacted within a short span of time.

In all, the lunar samples seem to provide excellent proof that the study of lunar simulants is adequate when studying kinetic data. However, the complexity of the lunar soil and the lunar conditions that cannot be represented by terrestrial samples do introduce some additional questions.

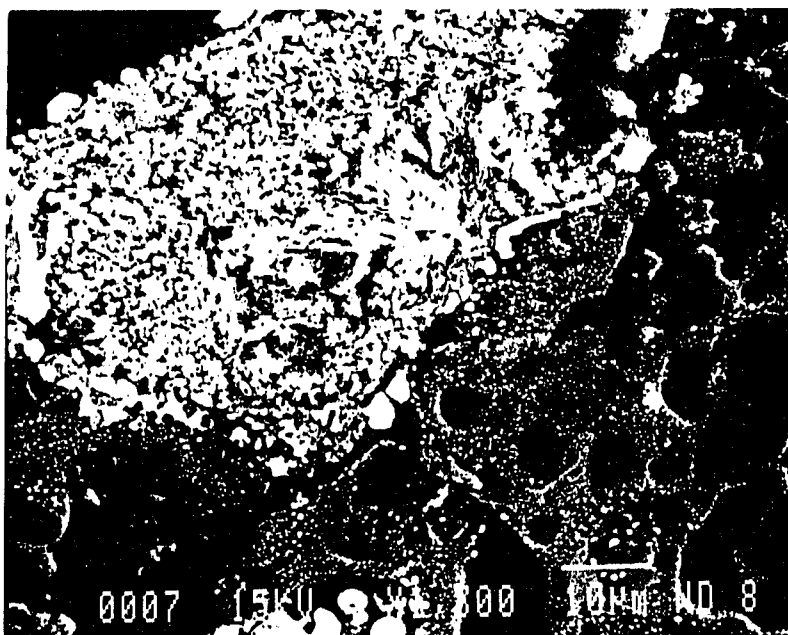


Figure 5.16 SEM Micrograph of Completely Reduced Lunar Sample, Particle #4

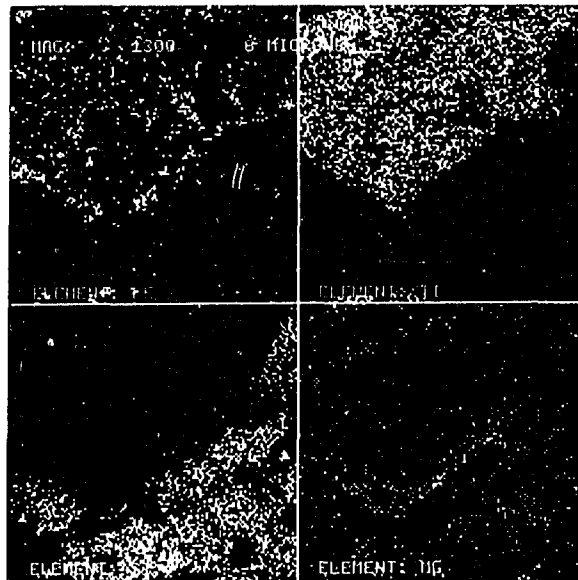


Figure 5.17a X-Ray Map Detailing Fe, Ti, Si and Mg for Particle #4

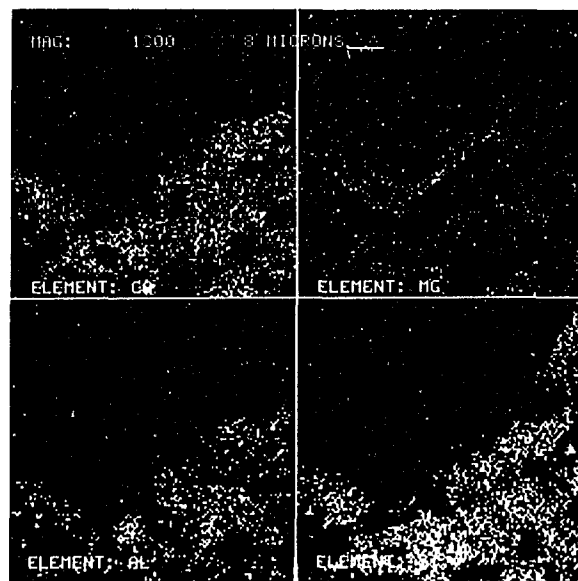


Figure 5.17a X-Ray Map Detailing Mg, Ca, Al, and Si for Particle #4

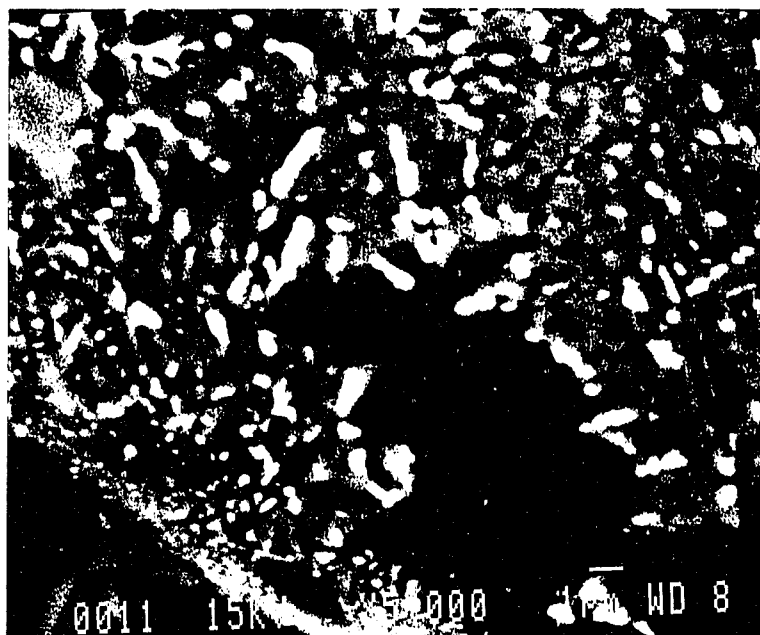


Figure 5.18 SEM Micrograph of Partially Reduced Lunar Sample, Particle #1

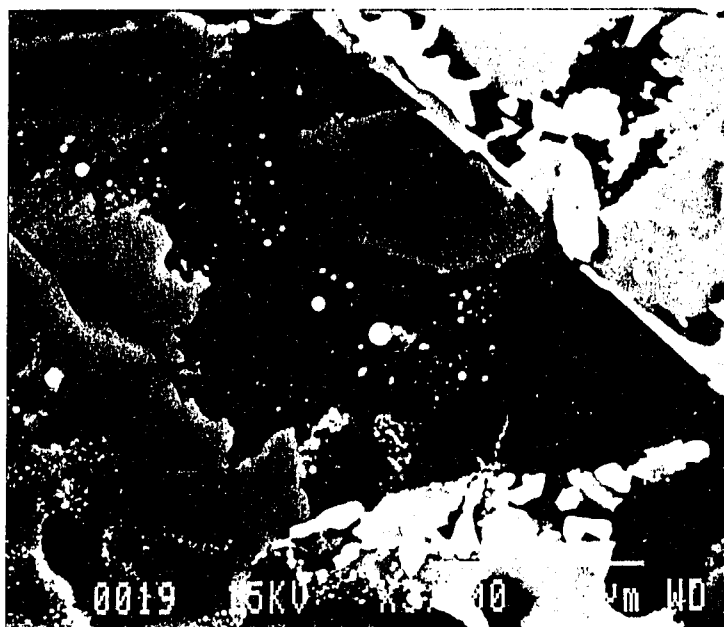


Figure 5.19 SEM Micrograph of Partially Reduced Lunar Sample, Particle # 5

CONCLUSIONS AND RECOMMENDATIONS

Conclusions

The effect of particle size on hydrogen reduction of ilmenite and carbon monoxide reduction of ilmenite has been determined and appropriate models which describing the fundamental reactions have been developed. A shrinking core model was found to best describe the data.

Experimentally, the geometry which provided the least diffusional resistance and was the easiest to used was the mesh box. The calcined pellet also offered reliable data, however, the data from the mesh box was extremely reproducible and the reaction rate was faster.

For hydrogen reduction of ilmenite, it was found that the reaction was well modeled using only the kinetically controlled SCM. Although iron is still produced within the micropores of the unreacted ilmenite, it does not seem to restrict the flow of hydrogen to the unreacted core.

For carbon monoxide reduction of ilmenite, it was found that the best model included a variable diffusivity term which was a function of conversion. The combined ash and kinetic model developed, contained the curvature expected and predicted the rate acceleration.

Reduction of the lunar sample showed lunar pyroxenes react similarly to terrestrial pyroxenes and that the overall rate lies between the experimental pyroxene reduction rates. However, additional questions regarding the migration of iron and

magnesium separation have arisen. It was confirmed however, that iron bearing minerals are the first to react and that further study into iron reduction and iron beneficiation are justified.

Recommendations

As with all studies, as soon as one question is answered another arises. Further work, of course, needs to be done in order to predict diffusivity as a function of conversion. Given this function, the effect of particle size can be quantitatively determined, and, coupled with kinetic data, can be used to design a lunar reactor. However, the oxygen production rate will only be valid for the reduction of pure ilmenite. Since this is unfeasible on the moon, additional work needs to be done on pyroxene kinetics and on understanding how particle size effect pyroxene reduction. If the major components of lunar soil can be accurately characterized, a reactor designed around the average lunar soil composition can be created.

Additional work needs to be done on the mechanism of iron movement and the cause of structural breakage. Coupled with this work is the effect of calcium and magnesium. These elements are already known to affect the rate of reaction but they may also affect the rate of iron movement and separation.

In all, the possibility of lunar space station is great and the opportunity to produce oxygen is real. However, additional work needs to be done to turn the possibility into a reality.

NOTATION

A	particle surface area, cm^2
C_A	concentration of A, mol/cm^3
D_c	diffusivity, cm^2/min
E	activation energy, $\text{kcal}/\text{mol K}$
F_p	shape factor k_0 frequency factor, cm/min
k_s	reaction rate coefficient based on surface area, cm/min
m	nucleation model coefficient, min
N_A	moles of A, mol
Q_A	flux of A, $\text{mols}/\text{cm}^2 \text{ sec}$
r	radial position vector, cm
r_A	reaction rate of species A, $\text{mols}/\text{cm}^2 \text{ sec}$
r_c	radius of the unreacted core, cm
R	original particle radius, cm
R	universal gas constant, $1.98 \text{ cal}/\text{mol K}$
t	time, min
T	temperature, $^{\circ}\text{C}$ or K
V	volume of particle, cm^3
X	fraction of reactant converted into product, dimensionless
z	dimensionless unreacted core radius, dimensionless

Greek Symbols

- Γ dimensionless concentration gradient, dimensionless
- ξ dimensionless radius, dimensionless
- ρ density
- τ time for complete conversion of a single solid particle, min

Subscripts

- a ash controlled
- A gaseous reactant
- b bulk phase
- B solid reactant
- g gas phase
- k kinetics controlled
- s solid phase

Abbreviations

- SCM shrinking core model
- SEM scanning electron microscope

APPENDIX A: REDUCTION DATA

<u>Table A.1</u>		<u>T Run 5</u>		<u>325-400 mesh, 812 deg C, 15.08% H2</u>	
Time (min)	Mass (mg)	Time (min)	Mass (mg)	Time (min)	Mass (mg)
0	101.88	13	98.70	26	95.34
1	101.65	14	98.46	27	95.14
2	101.48	15	98.09	28	94.93
3	101.29	16	97.86	29	94.78
4	100.99	17	97.56	30	94.54
5	100.84	18	97.32	31	94.36
6	100.57	19	97.03	32	94.21
7	100.32	20	96.75	33	94.03
8	100.09	21	96.52	34	93.90
9	99.80	22	96.28	35	93.77
10	99.58	23	96.00	36	93.59
11	99.27	24	95.79	37	93.45
12	98.99	25	95.56		

<u>Table A.2</u>		<u>T Run 11</u>		<u>325-400 mesh, 861 deg C, 15.55% H2</u>	
Time (min)	Mass (mg)	Time (min)	Mass (mg)	Time (min)	Mass (mg)
0	136.62	7	133.67	14	130.09
1	136.37	8	133.17	15	129.64
2	136.06	9	132.63	16	129.19
3	135.65	10	132.15	17	128.73
4	135.16	11	131.60	18	128.32
5	134.70	12	131.11	19	127.88
6	134.16	13	130.57	20	127.52

<u>Table A.3</u>		<u>T Run 6</u>		<u>325-400 mesh, 910 deg C, 15.08% H2</u>	
Time (min)	Mass (mg)	Time (min)	Mass (mg)	Time (min)	Mass (mg)
0	115.96	5	112.29	9	109.27
1	115.55	6	111.45	10	108.58
2	114.75	7	110.71	11	108.02
3	113.94	8	109.96	12	107.41
4	113.13				

<u>Table A.4</u>		<u>T Run 7</u>		<u>325-400 mesh, 1012 deg C, 15.42% H2</u>	
Time (min)	Mass (mg)	Time (min)	Mass (mg)	Time (min)	Mass (mg)
0	134.11	3	130.22	5	127.25
1	133.24	4	128.72	6	125.88
2	131.83				

<u>Table A.5</u>		<u>T Run 12</u>		<u>325-400 mesh, 1080 deg C, 14.26% H2</u>	
Time (min)	Mass (mg)	Time (min)	Mass (mg)	Time (min)	Mass (mg)
0	100.45	2	97.36	4	94.36
1	99.15	3	95.81	5	93.05

<u>Table A.6</u>		<u>T Run 8</u>		<u>140-170 mesh, 910 deg C, 13.98% H2</u>	
Time (min)	Mass (mg)	Time (min)	Mass (mg)	Time (min)	Mass (mg)
0	198.85	4	195.50	8	191.83
1	198.39	5	194.57	9	190.97
2	197.41	6	193.64	10	190.13
3	196.40	7	192.72		

<u>Table A.7</u>		<u>Run 3</u>		<u>140-170 mesh, 908 deg C, 13.15% H2</u>	
Time (min)	Mass (mg)	Time (min)	Mass (mg)	Time (min)	Mass (mg)
0	87.12	13	82.99	25	80.17
1	86.96	14	82.74	26	79.95
2	86.75	15	82.39	27	79.78
3	86.40	16	82.09	28	79.71
4	86.10	17	81.87	29	79.50
5	85.71	18	81.65	30	79.40
6	85.37	19	81.34	31	79.27
7	84.98	20	81.18	32	79.16
8	84.62	21	80.91	33	79.02
9	84.27	22	80.71	34	78.92
10	83.94	23	80.51	35	78.85
11	83.58	24	80.34	36	78.79
12	83.31				

<u>Table A.8</u>		<u>T Run 4</u>		<u>100-140 mesh, 812 deg C, 14.09% H2</u>	
Time (min)	Mass (mg)	Time (min)	Mass (mg)	Time (min)	Mass (mg)
0	207.71	4	206.69	8	205.42
1	207.56	5	206.38	9	205.10
2	207.27	6	206.07	10	204.88
3	207.00	7	205.83		

<u>Table A.9</u>		<u>T Run 10</u>		<u>100-140 mesh, 812 deg C, 14.22% H2</u>	
Time (min)	Mass (mg)	Time (min)	Mass (mg)	Time (min)	Mass (mg)
0	185.96	10	182.60	20	179.53
1	185.64	11	182.27	21	179.22
2	185.40	12	181.93	22	178.94
3	185.01	13	181.65	23	178.63
4	184.66	14	181.35	24	178.40
5	184.27	15	181.00	25	178.12
6	183.96	16	180.71	26	177.81
7	183.61	17	180.39	27	177.55
8	183.28	18	180.10	28	177.25
9	182.91	19	179.82		

<u>Table A.10</u>		<u>T Run 2</u>		<u>100-140 mesh, 906 deg C, 13.36% H2</u>			
Time (min)	Mass (mg)	Time (min)	Mass (mg)	Time (min)	Mass (mg)	Time (min)	Mass (mg)
0	194.92	4	192.82	7	190.93		
1	194.62	5	192.20	8	190.28		
2	194.06	6	191.60	9	189.66		
3	193.48						

<u>Table A.11</u>		<u>T Run 1</u>		<u>100-140 mesh, 1013 deg C, 14.77% H2</u>			
Time (min)	Mass (mg)	Time (min)	Mass (mg)	Time (min)	Mass (mg)	Time (min)	Mass (mg)
0	158.82	3	155.99	6	152.66		
1	158.13	4	154.86	7	151.71		
2	157.09	5	153.74	8	150.71		

<u>Table A.12</u>		<u>T Run 9</u>		<u>60-70 mesh, 812 deg C, 14.34% H2</u>			
Time (min)	Mass (mg)	Time (min)	Mass (mg)	Time (min)	Mass (mg)	Time (min)	Mass (mg)
0	136.58	12	133.80	23	131.66		
1	136.34	13	133.57	24	131.52		
2	136.06	14	133.37	25	131.33		
3	135.87	15	133.14	26	131.18		
4	135.60	16	132.93	27	131.01		
5	135.38	17	132.73	28	130.84		
6	135.18	18	132.56	29	130.70		
7	134.92	19	132.36	30	130.55		
8	134.69	20	132.18	31	130.40		
9	134.49	21	131.99	32	130.28		
10	134.23	22	131.83	33	130.10		
11	134.00						

<u>Table A.13</u>		<u>T Run 3</u>		<u>60-70 mesh, 1016 deg C, 13.34% H2</u>			
Time (min)	Mass (mg)	Time (min)	Mass (mg)	Time (min)	Mass (mg)	Time (min)	Mass (mg)
0	204.44	4	200.358	8	195.816		
1	204.042	5	199.18	9	194.768		
2	202.864	6	198.022	10	193.79		
3	201.576	7	196.904				

<u>Table A.14</u>		<u>CO Run 6</u>				<u>325-400 mesh, 917 deg C, 15.0% CO</u>	
<u>Time (min)</u>	<u>Mass (mg)</u>	<u>Time (min)</u>	<u>Mass (mg)</u>	<u>Time (min)</u>	<u>Mass (mg)</u>	<u>Time (min)</u>	<u>Mass (mg)</u>
0	98.85	36	97.02	71	93.44		
1	98.79	37	96.93	72	93.23		
2	98.76	38	96.88	73	93.04		
3	98.73	39	96.81	74	92.75		
4	98.65	40	96.71	75	92.52		
5	98.63	41	96.69	76	92.34		
6	98.61	42	96.63	77	92.09		
7	98.53	43	96.50	78	91.84		
8	98.49	44	96.52	79	91.60		
9	98.49	45	96.44	80	91.35		
10	98.43	46	96.37	81	91.12		
11	98.37	47	96.24	82	90.84		
12	98.32	48	96.21	83	90.68		
13	98.29	49	96.14	84	90.48		
14	98.19	50	96.06	85	90.27		
15	98.17	51	95.97	86	90.09		
16	98.12	52	95.92	87	89.92		
17	98.02	53	95.84	88	89.68		
18	98.03	54	95.78	89	89.57		
19	97.94	55	95.69	90	89.42		
20	97.94	56	95.59	91	89.30		
21	97.84	57	95.48	92	89.16		
22	97.79	58	95.37	93	89.10		
23	97.73	59	95.27	94	88.93		
24	97.68	60	95.17	95	88.91		
25	97.60	61	95.07	96	88.88		
26	97.58	62	95.03	97	88.80		
27	97.50	63	94.90	98	88.75		
28	97.48	64	94.76	99	88.68		
29	97.39	65	94.59	100	88.66		
30	97.32	66	94.47	101	88.70		
31	97.31	67	94.27	102	88.64		
32	97.26	68	94.11	103	88.65		
33	97.14	69	94.01	104	88.59		
34	97.11	70	93.71	105	88.52		
35	97.05						

Table A.15 **CO Run 1** **325-400 mesh, 1016 deg C, 15.0% CO**

Time (min)	Mass (mg)	Time (min)	Mass (mg)	Time (min)	Mass (mg)
0	113.45	16	111.33	32	108.24
1	113.35	17	111.18	33	107.94
2	113.23	18	111.06	34	107.67
3	113.13	19	110.92	35	107.38
4	113.09	20	110.77	36	107.07
5	112.93	21	110.60	37	106.76
6	112.80	22	110.43	38	106.45
7	112.69	23	110.26	39	106.14
8	112.50	24	110.03	40	105.83
9	112.34	25	109.91	41	105.52
10	112.22	26	109.69	42	105.21
11	112.07	27	109.47	43	104.89
12	111.91	28	109.25	44	104.59
13	111.82	29	109.04	45	104.33
14	111.62	30	108.81		
15	111.50	31	108.53		

Table A.16 **CO Run 2** **325-400 mesh, 1115 deg C, 14.8% CO**

Time (min)	Mass (mg)	Time (min)	Mass (mg)	Time (min)	Mass (mg)
0	126.50	11	124.04	22	120.71
1	126.32	12	123.81	23	120.26
2	125.97	13	123.62	24	119.81
3	125.65	14	123.36	25	119.39
4	125.39	15	123.16	26	118.96
5	125.15	16	122.84	27	118.55
6	124.92	17	122.53	28	118.14
7	124.73	18	122.18	29	117.72
8	124.57	19	121.87	30	117.34
9	124.39	20	121.53	31	116.96
10	124.19	21	121.09		

Table A.17 **CO Run 5** **325-400 mesh, 1167 deg C, 15.0% CO**

Time (min)	Mass (mg)	Time (min)	Mass (mg)	Time (min)	Mass (mg)
0	101.40	11	98.70	22	95.21
1	101.04	12	98.41	23	94.92
2	100.66	13	98.11	24	94.64
3	100.36	14	97.81	25	94.30
4	100.13	15	97.55	26	94.04
5	99.96	16	97.24	27	93.74
6	99.79	17	96.94	28	93.48
7	99.60	18	96.59	29	93.22
8	99.36	19	96.25	30	92.99
9	99.20	20	95.92	31	92.73
10	98.95	21	95.57		

<u>Table A.18</u>		<u>CO Run 7</u>				<u>100-140 mesh, 919 deg C, 15.0% CO</u>	
Time (min)	Mass (mg)	Time (min)	Mass (mg)	Time (min)	Mass (mg)	Time (min)	Mass (mg)
0	99.12	44	97.96	88	96.77		
1	99.02	45	97.95	89	96.79		
2	98.97	46	97.91	90	96.71		
3	98.93	47	97.84	91	96.70		
4	98.92	48	97.85	92	96.65		
5	98.88	49	97.81	93	96.61		
6	98.82	50	97.81	94	96.63		
7	98.86	51	97.78	95	96.55		
8	98.82	52	97.74	96	96.56		
9	98.80	53	97.74	97	96.48		
10	98.80	54	97.69	98	96.47		
11	98.78	55	97.66	99	96.40		
12	98.74	56	97.65	100	96.41		
13	98.71	57	97.60	101	96.37		
14	98.68	58	97.65	102	96.32		
15	98.65	59	97.57	103	96.26		
16	98.66	60	97.57	104	96.26		
17	98.59	61	97.52	105	96.22		
18	98.60	62	97.49	106	96.22		
19	98.57	63	97.44	107	96.16		
20	98.55	64	97.48	108	96.02		
21	98.54	65	97.48	109	96.12		
22	98.51	66	97.43	110	96.07		
23	98.49	67	97.38	111	96.04		
24	98.47	68	97.38	112	95.97		
25	98.44	69	97.34	113	95.97		
26	98.39	70	97.30	114	95.91		
27	98.43	71	97.25	115	95.90		
28	98.39	72	97.25	116	95.85		
29	98.35	73	97.20	117	95.85		
30	98.29	74	97.21	118	95.75		
31	98.30	75	97.17	119	95.74		
32	98.26	76	97.11	120	95.71		
33	98.26	77	97.08	121	95.66		
34	98.21	78	97.06	122	95.63		
35	98.17	79	97.01	123	95.56		
36	98.15	80	97.02	124	95.58		
37	98.13	81	96.95	125	95.51		
38	98.13	82	96.96	126	95.48		
39	98.09	83	96.92	127	95.38		
40	98.11	84	96.88	128	95.35		
41	98.02	85	96.82	129	95.27		
42	98.00	86	96.86	130	95.27		
43	98.00	87	96.81	131	95.27		

<u>CO Run 7 (cont.)</u>					
Time (min)	Mass (mg)	Time (min)	Mass (mg)	Time (min)	Mass (mg)
132	95.20	156	94.22	180	93.34
133	95.16	157	94.24	181	93.35
134	95.17	158	94.18	182	93.28
135	95.09	159	94.14	183	93.29
136	95.04	160	94.06	184	93.23
137	95.04	161	94.25	185	93.16
138	94.96	162	94.12	186	93.13
139	94.93	163	94.07	187	93.09
140	94.89	164	93.97	188	93.04
141	94.82	165	93.95	189	92.98
142	94.78	166	93.91	190	92.97
143	94.81	167	93.89	191	92.91
144	94.74	168	93.83	192	92.89
145	94.74	169	93.78	193	92.94
146	94.65	170	93.76	194	92.82
147	94.61	171	93.69	195	92.72
148	94.58	172	93.67	196	92.69
149	94.54	173	93.62	197	92.74
150	94.52	174	93.57	198	92.73
151	94.44	175	93.58	199	92.66
152	94.40	176	93.53	200	92.62
153	94.38	177	93.43	201	92.41
154	94.35	178	93.42		
155	94.30	179	93.41		

<u>Table A.19 CO Run 4 100-140 mesh, 1016 deg C, 15.0% CO</u>					
Time (min)	Mass (mg)	Time (min)	Mass (mg)	Time (min)	Mass (mg)
0	179.46	17	178.13	34	176.93
1	179.38	18	178.03	35	176.81
2	179.30	19	177.96	36	176.72
3	179.24	20	177.93	37	176.68
4	179.16	21	177.81	38	176.60
5	179.06	22	177.79	39	176.50
6	179.02	23	177.70	40	176.37
7	178.93	24	177.65	41	176.33
8	178.81	25	177.56	42	176.23
9	178.76	26	177.47	43	176.14
10	178.67	27	177.40	44	176.08
11	178.61	28	177.37	45	175.96
12	178.50	29	177.23	46	175.89
13	178.46	30	177.19	47	175.77
14	178.36	31	177.11	48	175.65
15	178.28	32	177.05	49	175.57
16	178.19	33	176.99	50	175.46

<u>CO Run 4 (cont.)</u>					
Time (min)	Mass (mg)	Time (min)	Mass (mg)	Time (min)	Mass (mg)
51	175.37	64	173.74	77	171.80
52	175.25	65	173.62	78	171.63
53	175.14	66	173.48	79	171.46
54	175.04	67	173.32	80	171.30
55	174.91	68	173.19	81	171.17
56	174.78	69	173.05	82	171.00
57	174.69	70	172.90	83	170.84
58	174.53	71	172.70	84	170.68
59	174.45	72	172.56	85	170.54
60	174.28	73	172.43	86	170.36
61	174.16	74	172.30	87	170.17
62	174.03	75	172.10	88	170.05
63	173.89	76	171.98		

<u>Table A.20 CO Run 3 100-140 mesh, 1114 deg C, 15.0% CO</u>					
Time (min)	Mass (mg)	Time (min)	Mass (mg)	Time (min)	Mass (mg)
0	177.26	18	174.81	36	171.91
1	177.09	19	174.73	37	171.71
2	176.89	20	174.60	38	171.46
3	176.71	21	174.51	39	171.18
4	176.47	22	174.38	40	170.98
5	176.35	23	174.27	41	170.68
6	176.20	24	174.13	42	170.44
7	176.07	25	174.00	43	170.19
8	175.92	26	173.88	44	169.88
9	175.83	27	173.70	45	169.67
10	175.72	28	173.56	46	169.40
11	175.56	29	173.40	47	169.11
12	175.45	30	173.17	48	168.83
13	175.34	31	172.99	49	168.60
14	175.25	32	172.79	50	168.35
15	175.15	33	172.59	51	167.92
16	175.07	34	172.37	52	167.74
17	174.92	35	172.17		

<u>Table A.21 CO Run 9 100-140 mesh, 1173 deg C, 15.1% CO</u>					
Time (min)	Mass (mg)	Time (min)	Mass (mg)	Time (min)	Mass (mg)
0	150.96	4	150.24	8	149.63
1	150.82	5	150.05	9	149.49
2	150.61	6	149.93	10	149.40
3	150.39	7	149.79	11	149.21

<u>Table A.22</u>		<u>CO Run 10</u>				<u>100-140 mesh, 1121 deg C, 15.3% CO</u>	
Time (min)	Mass (mg)	Time (min)	Mass (mg)	Time (min)	Mass (mg)		
0	430.85	8	428.18	16	425.88		
1	430.63	9	427.87	17	425.62		
2	430.28	10	427.56	18	425.37		
3	429.93	11	427.26	19	425.12		
4	429.56	12	426.96	20	424.86		
5	429.22	13	426.71	21	424.62		
6	428.82	14	426.44				
7	428.54	15	426.13				

<u>Table A.23</u>		<u>CO Run 11</u>				<u>170-200 mesh, 1120 deg C, 15.3% CO</u>	
Time (min)	Mass (mg)	Time (min)	Mass (mg)	Time (min)	Mass (mg)		
0	116.56	24	113.41	48	107.55		
1	116.46	25	113.17	49	107.39		
2	116.33	26	112.96	50	107.25		
3	116.12	27	112.70	51	107.09		
4	115.97	28	112.44	52	106.88		
5	115.84	29	112.17	53	106.78		
6	115.71	30	111.91	54	106.63		
7	115.60	31	111.64	55	106.48		
8	115.48	32	111.33	56	106.29		
9	115.39	33	111.14	57	106.20		
10	115.28	34	110.82	58	106.08		
11	115.22	35	110.52	59	105.91		
12	115.11	36	110.27	60	105.84		
13	115.03	37	109.97	61	105.71		
14	114.93	38	109.76	62	105.64		
15	114.83	39	109.49	63	105.59		
16	114.74	40	109.25	64	105.49		
17	114.62	41	108.98	65	105.41		
18	114.47	42	108.75	66	105.37		
19	114.35	43	108.52	67	105.35		
20	114.17	44	108.28	68	105.29		
21	113.96	45	108.09	69	105.25		
22	113.80	46	107.89	78	105.04		
23	113.62	47	107.72				

<u>Table A.24</u>		<u>N-1 Lunar Sample</u>		<u>+ 19 mesh, 1109 deg C, 25.6% H2</u>	
Time (min)	Mass (mg)	Time (min)	Mass (mg)	Time (min)	Mass (mg)
0	93.27	15	92.06	360	90.80
1	93.06	20	91.95	420	90.72
2	92.80	26	91.86	480	90.64
3	92.64	30	91.82	540	90.57
4	92.63	40	91.70	600	90.50
5	92.45	50	91.63	660	90.44
6	92.38	60	91.58	720	90.36
7	92.33	120	91.31	780	90.30
8	92.28	180	91.14	840	90.25
9	92.24	240	91.02	900	90.19
10	92.18	300	90.91	960	90.14

<u>Table A.25</u>		<u>N-2 Lunar Sample</u>		<u>19-20 mesh, 1109 deg C, 25.6% H2</u>	
Time (min)	Mass (mg)	Time (min)	Mass (mg)	Time (min)	Mass (mg)
0.00	46.64	1.00	46.51	1.75	46.37
0.25	46.60	1.25	46.45	2.00	46.32
0.50	46.57	1.50	46.43	2.25	46.26
0.75	46.53				

APPENDIX B: PARTICLE SIZE DATA

The particle size was determined by dividing the particle volume by the particle surface area. These values were provided by the SEM's NORAN system in the form of particle area and particle perimeter. The sum of the area column in each mesh size range was divided by the sum of the corresponding perimeter column. Multiplying this value by two gave the effective particle radius.

325-400 Mesh, Analysis #1

Effective Radius = 6.25 μm

BASIC SHAPE ANALYSIS							
PART.	AREA (μm^2)	PERIM (μm)	SHAPE FACTOR	X-FERET (μm)	Y-FERET (μm)	CNTR-X (PIXEL)	CNTR-Y (PIXEL)
1	448.62	85.61	1.322	28.88	28.63	391	47
2	442.14	173.38	5.485	28.88	38.72	21	63
3	988.21	298.59	7.811	35.79	34.98	161	73
4	663.87	187.92	4.237	31.82	34.68	278	76
5	672.42	171.22	3.468	29.53	48.86	468	189
6	451.75	145.26	3.716	36.89	27.44	412	147
7	586.88	155.11	3.788	37.58	22.37	278	288
8	684.88	318.28	13.327	34.68	51.88	189	288
9	1818.72	218.85	3.748	35.19	45.84	96	228
10	675.53	222.52	5.832	38.77	35.79	485	267
11	119.58	47.72	1.516	13.42	13.12	375	343
12	559.23	289.78	6.257	38.42	32.51	387	319
13	573.28	132.44	2.434	31.61	34.68	184	358
14	486.92	179.87	5.286	32.51	31.82	422	388
15	138.53	84.71	4.375	17.88	15.88	382	426
16	698.13	363.92	15.896	41.16	31.91	164	446
17	772.78	222.52	5.899	44.44	33.11	418	444
18	318.88	185.89	2.877	25.65	24.16	498	471

325-400 Mesh, Analysis #2Effective Radius = 6.56 μm

BASIC SHAPE ANALYSIS							
PART	AREA (μM^2)	PERIM (μM)	SHAPE FACTOR	X-FERET (μM)	Y-FERET (μM)	CNTR-X (PIXEL)	CNTR-Y (PIXEL)
1	676.11	188.76	6.913	27.44	22.07	182	36
2	191.12	70.89	2.845	23.86	12.52	39	57
3	78.74	42.05	1.786	12.82	9.24	131	98
4	197.71	107.38	4.641	23.26	15.88	3	188
5	93.69	57.86	2.843	11.93	13.42	312	129
6	2447.39	395.89	4.821	102.01	47.72	341	88
7	129.64	52.28	1.671	12.82	17.59	336	162
8	1151.66	222.82	3.438	39.97	48.26	222	146
9	121.18	53.69	1.893	13.72	15.88	386	195
10	188.55	54.28	2.159	16.48	12.82	464	209
11	438.84	168.48	4.678	24.46	32.21	13	185
12	578.88	139.90	2.731	36.39	26.24	19	275
13	745.88	121.48	1.571	27.74	41.46	158	272
14	1926.36	531.93	11.682	58.76	58.16	243	313
15	991.13	291.29	6.417	51.98	32.81	27	368
16	488.53	156.98	4.795	24.16	29.92	227	396
17	1821.47	332.69	8.633	33.78	48.82	419	413
18	456.28	92.47	1.498	25.85	26.54	65	466

170-200 Mesh Analysis #1Effective Radius = 14.32 μ m

BASIC SHAPE ANALYSIS							
PART	AREA (μ m ²)	PERIM (μ m)	SHAPE FACTOR	X-FERET (μ m)	Y-FERET (μ m)	CNTR-X (PIXEL)	CNTR-Y (PIXEL)
1	64.59	32.81	1.325	12.83	3.74	395	47
2	4128.81	286.56	13.808	77.65	98.59	52	68
3	4258.75	371.87	3.583	75.46	183.98	422	59
4	160.38	69.99	2.431	28.78	24.86	418	125
5	5675.18	1156.89	18.742	187.18	94.21	155	123
6	3511.53	1838.92	31.344	129.86	188.62	297	183
7	1985.83	228.93	1.955	51.48	56.87	364	143
8	4693.33	717.49	3.729	39.63	188.62	114	139
9	3448.52	739.37	12.644	75.46	89.68	229	148
10	1857.51	171.71	3.219	62.34	42.53	316	172
11	2725.14	249.28	1.799	79.84	63.43	91	199
12	2975.16	447.34	5.352	74.37	68.98	292	198
13	3234.76	739.37	13.449	83.12	64.53	163	197
14	2971.57	521.71	7.299	83.12	64.53	251	223
15	2612.69	369.37	4.617	79.94	59.86	248	245
16	6289.73	636.56	5.193	119.21	75.46	438	264
17	5645.23	451.71	2.975	118.46	91.67	329	267
18	3338.46	279.99	1.872	68.98	72.12	175	298
19	6488.13	731.71	6.656	98.72	118.46	182	264
20	2945.26	728.73	14.837	78.74	67.81	393	325
21	1746.57	225.31	3.312	62.34	68.15	348	334
22	943.87	198.46	3.745	76.56	24.86	438	351
23	4993.38	476.67	3.623	85.31	113.74	294	312
24	1461.86	281.89	4.388	45.93	98.78	146	347
25	3732.68	319.37	2.145	77.65	69.99	185	366
26	3221.58	318.62	2.382	59.86	73.74	318	366
27	4245.62	1388.12	32.876	98.59	72.12	421	394
28	7338.82	494.37	2.649	63.98	155.31	289	377
29	938.71	134.53	1.546	37.18	41.56	384	431
30	3348.33	319.36	3.138	32.76	77.65	132	421
31	8994.48	1213.43	29.578	97.34	73.23	38	431
32	3645.33	377.34	3.187	56.37	116.93	261	427
33	2898.23	488.25	6.347	71.89	61.24	434	454
34	3424.86	1369.33	14.174	131.71	35.15	285	467

170-200 Mesh, Analysis #2

Effective Radius = 14.49 μm

BASIC SHAPE ANALYSIS							
PART.	AREA (μM^2)	PERIM (μM)	SHAPE FACTOR	X-FERET (μM)	Y-FERET (μM)	CNTR-X (PIXEL)	CNTR-Y (PIXEL)
1	2924.92	388.28	4.181	74.37	67.81	274	58
2	1814.45	177.18	2.462	28.43	68.15	216	73
3	6139.34	562.18	4.896	115.93	79.84	115	93
4	6842.44	1647.18	35.735	139.37	98.43	327	88
5	334.96	139.99	4.656	27.34	26.24	64	144
6	838.22	226.48	4.912	38.28	43.74	134	146
7	2124.68	414.58	5.435	65.62	54.68	268	151
8	3878.36	277.81	1.532	34.21	79.84	281	152
9	4374.82	986.71	14.955	61.24	129.86	395	131
10	1857.51	159.68	1.918	48.12	34.99	333	185
11	2966.79	565.46	8.576	75.46	88.93	189	176
12	6559.24	429.84	2.248	187.18	38.59	315	284
13	977.36	247.18	4.974	38.28	49.21	165	234
14	4192.98	441.87	3.785	75.46	97.34	52	213
15	5871.67	1885.15	13.694	111.56	88.93	418	221
16	1685.56	222.83	2.324	36.71	45.93	245	255
17	1588.51	254.84	3.425	42.65	68.15	126	288
18	3755.14	918.12	14.184	73.74	74.37	68	287
19	4738.12	1878.72	19.298	54.68	146.56	387	267
20	6138.15	1891.89	46.363	189.37	117.83	214	287
21	4287.34	352.18	2.345	33.12	182.81	341	295
22	2813.66	787.49	17.548	74.37	66.71	436	316
23	1111.35	228.93	3.494	53.55	33.98	84	338
24	1766.91	276.71	3.448	78.74	43.74	167	355
25	2662.93	288.74	2.498	68.98	77.65	388	348
26	3638.73	394.84	3.416	79.84	73.23	357	387
27	3129.48	1898.46	38.248	38.98	182.81	97	383
28	5372.53	386.34	1.338	181.71	37.49	218	489
29	3958.12	344.58	5.386	85.81	74.67	294	425
30	3231.41	327.83	1.592	71.89	95.15	435	417

100-140 Mesh, Analysis #1Effective Radius = 16.28 μm

BASIC SHAPE ANALYSIS							
PART.	AREA (μM^2)	PERIM (μM)	SHAPE FACTOR	X-FERET (μM)	Y-FERET (μM)	CNTR-X (PIXEL)	CNTR-Y (PIXEL)
1	21998.31	4432.94	71.894	215.46	141.89	98	64
2	9263.96	661.71	3.768	114.84	128.31	468	145
3	12956.86	3188.26	62.437	188.12	138.15	176	154
4	62.28	56.87	4.137	13.12	16.48	91	289
5	345.72	129.86	3.833	37.18	29.53	110	233
6	1991.79	646.48	16.694	74.37	57.96	381	238
7	18193.46	666.89	3.463	133.43	178.28	387	198
8	18712.65	782.18	3.662	178.28	135.62	288	229
9	2259.76	266.87	2.587	182.81	48.12	188	299
10	2958.81	255.93	1.766	62.34	92.96	428	316
11	8272.24	714.21	4.986	89.68	179.37	51	383
12	1181.77	264.68	5.859	48.12	49.21	128	374
13	4682.87	576.48	5.744	89.68	189.37	342	351
14	18461.21	1544.36	17.883	128.31	136.71	285	345
15	3741.95	888.27	13.694	71.89	85.51	444	419
16	9148.74	975.61	8.236	148.74	126.87	121	453
17	6368.97	479.85	2.866	125.78	97.34	312	467

60-70 Mesh, Analysis #1

Effective Radius = 55.75 μm

BASIC SHAPE ANALYSIS							
PART.	AREA (μM^2)	PERIM (μM)	SHAPE FACTOR	X-FERET (μM)	Y-FERET (μM)	CNTR-X (PIXEL)	CNTR-Y (PIXEL)
1	73.40	36.78	1.466	18.44	18.44	254	182
2	774.62	212.78	4.658	52.28	32.31	345	143
3	1221.99	298.34	5.489	44.74	49.71	189	144
4	185.29	58.21	1.984	12.92	15.41	233	198
5	844.81	188.46	3.867	46.73	37.76	118	176
6	62.83	29.82	1.148	12.44	9.94	284	218
7	63.76	34.88	1.518	18.93	9.44	468	228
8	618.16	211.78	5.773	52.33	45.73	338	192
9	1146.35	334.58	7.771	59.16	43.74	488	195
10	113.44	39.77	1.188	13.42	12.42	328	244
11	388.54	88.84	1.311	26.84	22.37	123	238
12	356.98	108.38	2.613	22.86	34.38	292	238
13	177.46	68.65	1.648	18.39	18.39	435	254
14	169.88	67.11	2.118	14.41	17.48	418	277
15	1586.86	461.36	18.679	65.12	55.18	217	247
16	79.83	35.79	1.276	18.93	18.44	189	331
17	1368.67	585.61	18.933	77.85	34.51	65	278
18	2391.53	583.12	9.422	79.54	63.63	273	382
19	196.74	82.83	3.721	33.36	18.39	166	353
20	775.85	221.72	5.842	41.76	48.26	213	367
21	242.71	67.11	1.476	22.36	16.48	384	398
22	937.99	229.19	4.455	48.22	57.17	372	368

REFERENCES

- Bardi, G.; Gozzi, D.; Stranges, S.; High Temperature Reduction Kinetics of Ilmenite by Hydrogen. *Mater. Chem. Phys.* 1987, 17, pp. 325-341.
- Bird, R.B.; Stewart, W.E.; Lightfoot, E.N.; Transport Phenomena. John Wiley & Sons, New York, 1960.
- Blanford, G.E.; Solar-wind irradiation effects on ilmenite (abstract). *Lunar and Planetary Science XIII*. Lunar and Planetary Institute, Houston. 1982, pp. 47-48.
- Briggs, R.A.; Sacco, J.A.; Hydrogen Reduction Mechanisms of Ilmenite Between 823 and 1353 K. *J. Mater. Res.* 1991, 6(3), pp. 574-584.
- Cutler, A.H.; Power Demands for Space Resource Utilization. *Space Nuclear Power Systems*, 1986, pp. 25-42.
- Cutler, A.H.; Waldron, R.D.; Evaluation of Processing Options for Lunar Oxygen Production. Proceedings of Space '92, ASCE, Denver, CO, June 1-4, 1992.
- Deer, W.A.; Howie, R.A.; Zussman, J.; Rock Forming Minerals, 2nd ed. Vol. 1a. Halsted Press, New York, 1982.
- Galwey, A.K.; Chemistry of Solids. Chapman and Hall Ltd., London, 1967.
- Gibson E.K.; Knudsen C.W.; Lunar oxygen production from ilmenite. *Lunar Bases and Space Activities of the 21st Century* (W.W. Mendel, ed.). Lunar and Planetary Institute, Houston, 1985, pp. 543-550.
- Heiken, G.H.; Vaniman, D.T.; French, D.E.; eds. *Lunar Sourcebook*. Cambridge University Press, 1991.
- Kiko, J.; Warhaut, M.; Kirsten T.; Solar wind noble gas distribution in lunar ilmenites and correlated element fractionation (abstract). *Lunar and Planetary Science X*. Lunar and Planetary Institute, Houston, 1979, pp. 664-666.
- Levenspiel, O.; Omnibook. OSU Book Stores, Inc. Corvallis, Oregon, 1989.
- Levenspiel, O.; Chemical Reaction Engineering, 2nd Ed. John Wiley & Sons, New York, 1972.

- Massieon, C. Masters Thesis, Department of Chemical Engineering, University of Arizona, Tucson, AZ., 1992.
- McKay D.S.; Williams R.J.; A geological assessment of potential lunar ores. *Space Resources and Space Settlements* (J. Billingham et al., eds.). NASA SP-428, 1979, pp. 243-256.
- National Commission on Space; Pioneering the Space Frontier. Bantam, New York, 1986.
- Ramadorai, G.; Dean, R.; Beneficiation of Ilmenite from Lunar Analog. NASA Space Engineering Research Center, Annual Progress Report. University of Arizona, 1992, pp. 112-121.
- Smith, J.M.; Chemical Engineering Kinetics, 3rd Ed. McGraw-Hill Publishing Company, New York, 1981.
- Szekely, J.; Evans, J.W.; Sohn, H.Y.; Gas-Solid Reactions, Academic Press, New York, 1976.
- Williams R.J.; Erstfield T.E.; High Temperature Electrolyte Recovery of Oxygen from Gaseous Effluents from the Carbo-Chlorination of Lunar Anorthite and the Hydrogenation of Ilmenite. NASA TM-58214, 1979.
- Williams R.J.; Oxygen extraction from lunar materials: An experimental test of an ilmenite reduction process. *Lunar Bases and Space Activities of the 21st Century* (W.W. Mendel, ed.), 1985.
- Wouterlood, H.J. The Reduction of Ilmenite with Carbon. *J. Chem. Technol. Biotechnol.* 1979, 29, pp. 603-618.
- Zhao, Y.; Shadman, F.; Reduction of Ilmenite with Hydrogen. *Ind. Eng. Chem. Res.* 1991, 30, pp. 2080-2087.
- Zhao, Y. Doctoral Dissertation, Department of Chemical Engineering, University of Arizona, Tucson, AZ., 1991.
- Zhao, Y.; Shadman, F.; Kinetics and Mechanism of Ilmenite Reduction with Carbon Monoxide. *AIChE J.*, 1990, 36(9), pp. 1443-1438.